Technical Physics Letters, Vol. 28, No. 11, 2002, pp. 881–882. Translated from Pis'ma v Zhurnal Tekhnicheskoĭ Fiziki, Vol. 28, No. 21, 2002, pp. 1–5.
Original Russian Text Copyright © 2002 by Kyasov, Dedkov.

The Motion of a Neutral Spherical Particle between Coaxial Cylindrical Surfaces

A. A. Kyasov and G. V. Dedkov
Kabardino-Balkarian State University, Nal'chik, Kabardino-Balkaria, Russia
Received April 26, 2002

Abstract—The tangential and normal components of a dipole force acting upon a neutral spherical particle moving parallel to the axis of symmetry of a coaxial cylindrical channel with different permittivities of the internal and external walls are calculated in a nonrelativistic approximation of the fluctuational electromagnetic theory. Upon a limiting transition, the obtained formulas coincide with the previous results for a particle moving inside a cylindrical channel or parallel to the generatrix of a convex cylindrical surface. The problem is considered in the general case of different temperatures of the particle and the surface. *© 2002 MAIK "Nauka/Interperiodica".*

The electromagnetic and fluctuational-electromagnetic interaction of a moving charged or neutral particle with flat and curved surfaces (for example, with nanotubes) is of considerable interest, in particular, to nanotribology [1] and to particle beam control by nanotubes [2, 3]. Information about the forces acting upon particles in such systems is also of interest to the study of adsorption on fullerenes and the retardation of particles in porous media. The motion of positively and negatively charged particles in the field of nanotubes was considered in [2–8]. However, it was recently demonstrated [9] that nanotubes can also effectively transmit thermal atomic beams. In this case, the dynamic interactions of particles and surfaces must be described within the framework of the fluctuational electrodynamics [4].

A characteristic feature of the theory developed in our papers is the direct calculation of the average force with which a fluctuational electromagnetic field of a surface acts upon a moving fluctuating dipole. The statistical averaging is performed in terms of the fluctuational-dissipative relations, without recourse to any additional model simplifications [4, 10]. This approach was successfully employed to consider the fluctuational-electromagnetic interaction of a moving neutral particle with a cylindrical surface or a channel, as well as a number of related problems [4].

Here, we will consider a more general problem: longitudinal (nonrelativistic) motion of a neutral spherical particle with the polarizability $\alpha(\omega)$ in the space between two coaxial cylindrical surfaces with the radii a_1 and a_2 and the permittivities $\varepsilon_1(\omega)$ and $\varepsilon_2(\omega)$, respectively (see figure). It is assumed that $a_1 < R < a_2$, where R is the distance from the particle to the common axis of the cylinders, the cylinders possess the same temperature T_2, and the particle temperature is T_1 (for an atom in the ground state, $T_1 = 0$).

For a tangential (retarding) force acting upon the particle, calculations yield the following expressions:

$$F_z = \langle(\mathbf{d}\nabla)E_z\rangle = -\frac{\hbar}{\pi^2R^2}\sum_{n=0}^{\infty}\int_0^{\infty}d\omega\int_0^{\infty}dkk \times\{\coth(\omega\hbar/2k_BT_1)\alpha''(\omega)[\Delta''_{12,n}(\omega+kV) - \Delta''_{12,n}(\omega-kV)] + \coth(\omega\hbar/2k_BT_2)\Delta''_{12,n}(\omega) \times[\alpha''(\omega+kV)-\alpha''(\omega-kV)]\}, \quad (1)$$

$$\Delta_{12,n}(\omega) = \frac{1}{1-\Delta_{1,n}(\omega)\Delta_{2,n}(\omega)} \times\{(kR)^2[\Delta_{1,n}(\omega)K_n'^2(kR)+\Delta_{2,n}(\omega)I_n'^2(kR) - 2\Delta_{1,n}(\omega)\Delta_{2,n}(\omega)K_n'(kR)I_n'(kR)] + ((kR)^2+n^2)[\Delta_{1,n}(\omega)K_n^2(kR)+\Delta_{2,n}(\omega)I_n^2(kR) - 2\Delta_{1,n}(\omega)\Delta_{2,n}(\omega)K_n(kR)I_n(kR)]\}, \quad (2)$$

$$\Delta_{1,n}(\omega) = \frac{(\varepsilon_1(\omega)-1)I_n(ka_1)I_n'(ka_1)}{\varepsilon_1(\omega)I_n'(ka_1)K_n(ka_1)-I_n(ka_1)K_n'(ka_1)}, \quad (3)$$

$$\Delta_{2,n}(\omega) = \frac{(\varepsilon_2(\omega)-1)K_n'(ka_2)K_n(ka_2)}{\varepsilon_2(\omega)K_n'(ka_2)I_n(ka_2)-K_n(ka_2)I_n'(ka_2)}, \quad (4)$$

while the (conservative) component normal to the surfaces of the cylinders F_r is conveniently expressed in

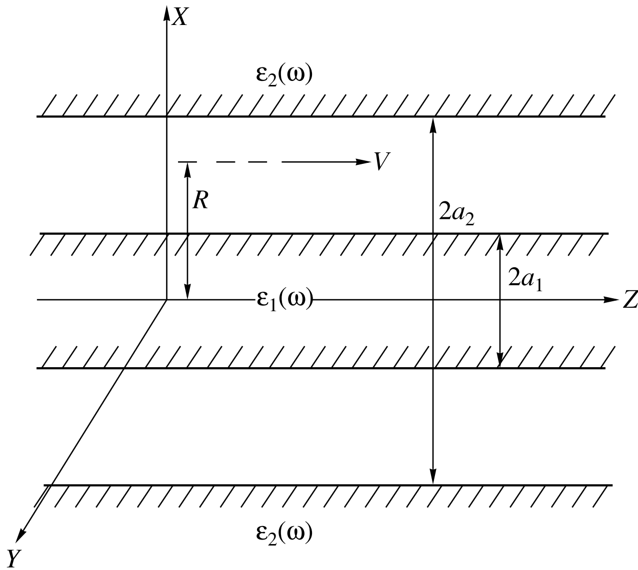

Schematic diagram showing the motion of a nonrelativistic particle ($V \ll c$) in a coaxial cylindrical channel and a coordinate system used to describe this motion.

terms of the potential energy $U(r)$ of the particle-surface interaction:

$$F_r\langle(\mathbf{d}\nabla)E_r\rangle = -\frac{\partial U}{\partial r}, \quad (5)$$

$$U(r) = -\frac{1}{2}\langle\mathbf{dE}\rangle = -\frac{\hbar}{\pi^2R^2}\sum_{n=0}^{\infty}\int_0^{\infty}d\omega\int_0^{\infty}dk$$
$$\times\{\coth(\omega\hbar/2k_BT_1)\alpha''(\omega)[\Delta''_{12,n}(\omega+kV)$$
$$+\Delta''_{12,n}(\omega-kV)]+\coth(\omega\hbar/2k_BT_2)\Delta''_{12,n}(\omega)$$
$$\times[\alpha'(\omega+kV)+\alpha'(\omega-kV)]\}. \quad (6)$$

Here, **d** is the dipole moment of the particle, E_z is the surface electric field component, $\hbar$ is the Planck constant, and k_B is the Boltzmann constant; $K_n(x)$, $I_n(x)$ and $K'_n(x)$, $I'_n(x)$ denote the nth order Bessel functions and their derivatives, respectively; for the other quantities in Eqs. (1) and (6), single and double prime denote real and imaginary components of the corresponding values, respectively; in the sums over n, the term with $n = 0$ is taken with a half weight.

From Eqs. (2)–(4), it follows for $a_1 \longrightarrow 0$ that $\Delta_{1,n}(\omega) \longrightarrow 0$ and

$$\Delta_{12,n}(\omega) = \lfloor(kR)^2I'^2_n(kR)+((kR)^2+n^2)I^2_n(kR)\rfloor\Delta_{2,n}(\omega), \quad (7)$$

while for $a_2 \longrightarrow 0$, accordingly, $\Delta_{2,n}(\omega) \longrightarrow 0$ and

$$\Delta_{12,n}(\omega) = \lfloor(kR)^2K'^2_n(kR)+((kR)^2+n^2)K^2_n(kR)\rfloor\Delta_{1,n}(\omega). \quad (8)$$

In the former case ($a_1 \longrightarrow 0$), Eqs. (1), (6), and (7) yield expressions for the tangential force and the interaction potential obtained previously for a particle interacting with a cylindrical channel [4, 11]. In the latter case, we arrive at the expressions obtained for a particle interacting with a convex cylindrical surface [4,11]. The general case described by Eqs.(1)–(6) is of practical interest for the description of neutral atomic particles (clusters) traveling in the cylindrical channels of multilayer nanotubes or in microcapillaries. Particular calculations of the particle trajectories must employ the potential (6) with allowance for the retardation losses (1). Moving at an angle to the axis of symmetry of the coaxial channel, the particles may approach the walls to a distance smaller than the interatomic spacings. In this case, the attraction potential (6) has to be complemented with a short-range repulsive component acting in a near-wall region.

REFERENCES

1. G. V. Dedkov, Usp. Fiz. Nauk **170** (6), 585 (2000).
2. G. V. Dedkov, Nucl. Instrum. Methods Phys. Res. B **143** (8), 584 (1998).
3. G. V. Dedkov and B. S. Karamurzov, Surf. Coat. Technol. **128**/**129**, 51 (2000).
4. G. V. Dedkov and A. A. Kyasov, Fiz. Tverd. Tela (St. Petersburg) (in press) [Phys. Solid State (in press)].
5. V. V. Klimov and V. S. Letokhov, Phys. Lett. A **222**, 424 (1996).
6. L. A. Gevorgian, K. A. Ispirian, and R. K. Ispirian, Nucl. Instrum. Methods Phys. Res. B **145**, 1555 (1998).
7. N. K. Zhevago and V. I. Glebov, Zh. Éksp. Teor. Fiz. **118**, 579 (2000) [JETP **91**, 504 (2000)].
8. N. F. Shul'ga and V. I. Truten', Izv. Akad. Nauk, Ser. Fiz. **66** (1), 85 (2002).
9. G. V. Dedkov, A. A. Kyasov, and R. I. Teghaev, in *Abstracts of SMMIB-2001, Marburg, Germany, 2001.*
10. G. V. Dedkov and A. A. Kyasov, Pis'ma Zh. Tekh. Fiz. **28** (8), 79 (2002) [Tech. Phys. Lett. **28**, 346 (2002)].
11. A. A. Kyasov and G. V. Dedkov, Surf. Sci. **491**, 124 (2001).

Translated by P. Pozdeev

Technical Physics Letters, Vol. 28, No. 11, 2002, pp. 883–884. Translated from Pis'ma v Zhurnal Tekhnicheskoĭ Fiziki, Vol. 28, No. 21, 2002, pp. 6–10.
Original Russian Text Copyright © 2002 by Kamanina, Voronin.

Electron-Microscopic Study of the Polyimide–C_{70} Fullerene System

N. V. Kamanina* and Yu. M. Voronin

Vavilov Optical Institute, State Scientific Center of the Russian Federation, St. Petersburg, 190164 Russia

** e-mail: kamanin@ffm.ioffe.rssi.ru*

Received April 23, 2002

Abstract—The structure of a polyimide–C_{70} fullerene system was studied on an HU-11B electron microscope at an accelerating voltage of 75 kV. The formation of a conjugated organic system representing a polyimide matrix sensitized by fullerenes was traced. © *2002 MAIK "Nauka/Interperiodica".*

Good prospects for the use of C_{60} and C_{70} fullerenes in polyimide-based systems were demonstrated in [1–9]. In particular, it was found that fullerene-containing polyimides (PIs) exhibit a longwave shift in the absorption spectra, possess increased photoconductivity, produce optical confinement in the visible spectral range (the level of which depends on the fullerene content), and can be used for the modulation of laser radiation [1–4]. The same PI–fullerene system [5, 6] produces nonlinear attenuation of laser radiation in the near IR range (at 1315 nm), which can be effectively controlled with allowance for the spectral features of the lamp pumping of an iodine laser. The photorefractive effect in fullerene-containing PIs was confirmed by recording thin-layer phase diffraction gratings with a sufficiently high spatial frequency of ~100 mm^{-1} using nano- and picosecond laser pulses at a wavelength of $\lambda = 532$ nm [7, 8]. The threshold for the transition from phase to amplitude grating was found, and the induced refractive index was determined from the dependence of the diffraction efficiency on the readout beam energy density. It was also established that polymer-dispersed liquid crystal systems based on the fullerene-containing PI matrices can be used for attenuating laser radiation and for recording holograms [9].

All investigations devoted to the effects of optical confinement and holographic recording have shown that the fullerene-sensitized PI systems are characterized by sufficiently high radiation and thermal stability. These results showed the need for more thorough investigation of the structure of fullerene-containing PIs by microscopic techniques in order to elucidate the role of fullerene molecules in the formation of photosensitized polymer films.

The experiments were performed with thin films of grade 6B polyimide (PI-6B) prepared from 3% solutions of the photosensitive compositions in tetrachloroethane. The polymer was sensitized by introducing C_{60} and C_{70} fullerenes to a concentration of 0.2–0.5 wt % with respect to the dry PI weight. The drops of solution were applied onto the surface of distilled water, after which the spread polymer film was collected by copper grids and dried for 8–12 h until complete removal of the solvent. The thickness of the polymer film samples supported on the grids was ~0.1 μm.

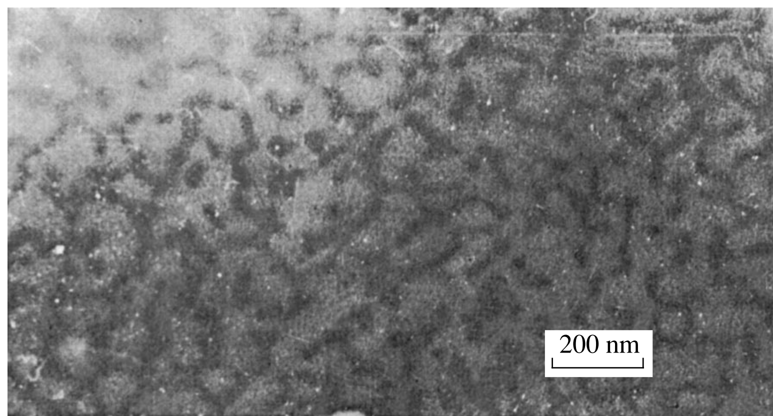

Fig. 1. An electron-microscopic image showing fullerene structures of various configurations forming chains of quasi-pentagonal and hexagonal shapes.

1063-7850/02/2811-0883$22.00 © 2002 MAIK "Nauka/Interperiodica"

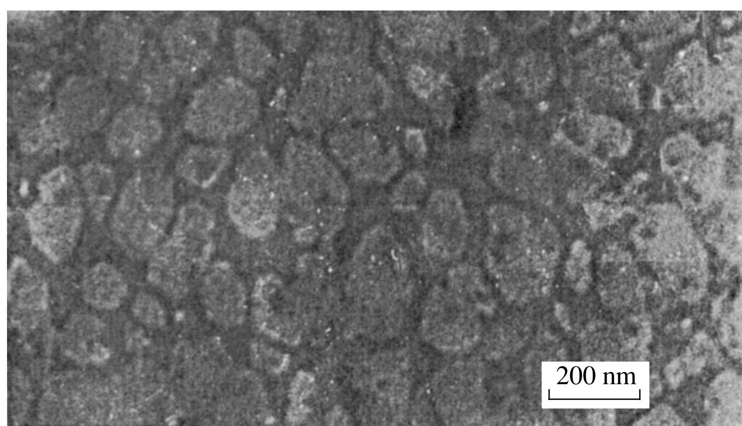

Fig. 2. An electron-microscopic image showing an example of the polyimide film formed on a framework of fullerene chains of quasi-pentagonal and hexagonal shapes.

The films were studied with an HU-11B electron microscope operating at an accelerating voltage of 75 kV and a magnification of ×12500. In order to increase the electron image contrast, the photographs were made using partial underfocusing conditions. The possibility of studying carbon films by this technique was demonstrated in [10].

Figures 1 and 2 present the first results of electron-microscopic examination of the PI–fullerene system, illustrating the formation of a film of the conjugated PI matrix sensitized with C_{70} fullerene. The image in Fig. 1 shows fullerene structures of various configurations forming close and open chains of quasi-pentagonal and hexagonal shapes. The image clearly reveals the aggregation of fullerene clusters into globules, the size of which reaches up to 10–50 nm. The dimensions of close fullerene configurations amounts to ~200 nm on the average. A difference in the contrast between the fullerene configurations and the matrix film material is probably due to the different molecular weights of the PI and C_{70} fullerene molecules. The molecular weight of a photosensitive monomer unit in the PI molecule is 750 (against 840 for C_{70} fullerene).

Figure 2 illustrates the formation of a PI film on the fullerene framework. As can be seen, there takes place a partial cross-linking of the open chains. Individual fullerene clusters are present both at the boundaries between the neighboring chains and inside the close rings. The pattern observed for the PI–C_{70} fullerene structures studied well explains the high strength of fullerene-containing systems and does not contradict the results of Shibata *et al.* [11], which showed an example of the formation of a high-strength nanocomposite resist. At the same time, the obtained images help us understand the processes involved in the synthesis of a homogeneous photosensitive polymer film, followed by the recording of an interference pattern.

When the PI–C_{70} fullerene composite structure is exposed to a laser beam with a spot size of 3–5 mm, the integral action of the light field upon the organic compound neither creates a refractive index gradient related to structural inhomogeneities nor activates light-induced scattering on such inhomogeneities. Instead, the laser action induces photorefractive processes with a change in the pathway of charge carriers: the carriers are transferred from a donor fragment of the organic molecule to fullerene, rather than to the intramolecular acceptor, because the electron affinity of fullerenes is several times that of many organic acceptors.

Thus, we have demonstrated the formation of conjugated organic thin-film structures based on fullerene-containing polyimide and showed the role of fullerene clusters in this process.

Acknowledgments. This study was partly supported by the Russian Foundation for Basic Research, project no. 00-15-99067.

REFERENCES

1. N. V. Kamanina, L. N. Kaporskii, and B. V. Kotov, Opt. Commun. **152** (4–6), 280 (1998).
2. Y. A. Cherkasov, N. V. Kamanina, E. L. Alexandrova, *et al.*, Proc. SPIE **3471**, 254 (1998).
3. N. V. Kamanina, Opt. Commun. **162** (4–6), 228 (1999).
4. N. V. Kamanina and N. A. Vasilenko, Nonlinear Opt. **25**, 207 (2000).
5. N. V. Kamanina, I. V. Bagrov, I. M. Belousova, *et al.*, Opt. Commun. **194** (4–6), 367 (2001).
6. N. V. Kamanina, I. V. Bagrov, I. M. Belousova, and A. P. Zhevlakov, Opt. Spektrosk. **91** (1), 5 (2001) [Opt. Spectrosc. **91**, 1 (2001)].
7. N. V. Kamanina, Opt. Spektrosk. **90** (6), 960 (2001) [Opt. Spectrosc. **90**, 867 (2001)].
8. N. V. Kamanina, Synth. Met. **127** (1–3), 121 (2002).
9. N. V. Kamanina, S. Putilin, and D. Stasel'ko, Synth. Met. **127** (1–3), 129 (2002).
10. Yu. M. Voronin and N. B. Voznesenskiĭ, Opt. Zh. **65** (1), 94 (1998) [J. Opt. Technol. **65**, 80 (1998)].
11. T. Shibata, T. Ishii, H. Nozawa, and T. Tamamura, Jpn. J. Appl. Phys. **36** (12B), 7642 (1997).

Translated by P. Pozdeev

Technical Physics Letters, Vol. 28, No. 11, 2002, pp. 885–888. Translated from Pis'ma v Zhurnal Tekhnicheskoĭ Fiziki, Vol. 28, No. 21, 2002, pp. 11–21.
Original Russian Text Copyright © 2002 by Berezkin, Viktorovskiĭ, Golubev, Petrova, Khoroshko.

A Comparative Study of the Sorption Capacity of Activated Charcoal, Soot, and Fullerenes for Organochlorine Compounds

V. I. Berezkin, I. V. Viktorovskiĭ, L. V. Golubev, V. N. Petrova, and L. O. Khoroshko

Ecological Safety Research Center, Russian Academy of Sciences, St. Petersburg, Russia
e-mail: vibii5@mail.infostar.ru
Ioffe Physicotechnical Institute, Russian Academy of Sciences, St. Petersburg, 194021 Russia
e-mail: Golubeviv@mail.ioffe.ru

Received May 3, 2002

Abstract—New experimental data on the sorption properties of fullerenes are presented. Fullerenes are approximately ten times more effective physical adsorbents of organic impurities from water than traditional activated carbons. *© 2002 MAIK "Nauka/Interperiodica".*

Active (activated) charcoals are widely used as sorbents in various fields. Another representative of dispersed carbons, also used on a commercial scale, is soot. However, the sorption properties of soot are much less studied because this substance is usually not employed as a sorbent. Fullerenes, which have been extensively studied over the past decade, are virtually not characterized with respect to their sorption properties.

In this context, we performed a comparative study of the sorption capacity of activated charcoal, soot, and fullerenes for organochlorine compounds.

The experiments were conducted with samples of natural river water and waste water of a pharmaceutical plant. The sorbents were (i) commercial granulated activated charcoal (BAU-A grade) intended for the adsorption of organic impurities from aqueous solutions; (ii) soot produced by electric-arc discharge, containing ~5% fullerenes with the ratio $C_{60}/C_{70} = 5.5 : 1$; (iii) the same soot after extraction of fullerenes with xylene; and (iv) ground fullerene extract isolated from the soot. Since the specific surface area of the sorbents was unknown, the samples of sorbents were characterized by the weight content of carbon.

Weighted amounts of the activated charcoal (0.5 g), fullerene soot (0.5 g), fullerene-free soot (0.475 g), and fullerenes (0.025 g) were introduced into equal volumes of water (500 ml), and the mixtures were allowed to stand for two weeks. Then, water was filtered and extracted with methylene chloride. The extracts were analyzed on a QP-5000 chromatomass spectrometer (Shimadzu) in a range of masses from 33 to 450 amu and retention times from 8 to 65 min. The internal standard was decane.

Figure 1 presents chromatograms (peak intensity versus retention time) of the samples of natural water (a) in the initial state and (b) after treatment with fullerene soot. As can be seen, the sorbent produces effective cleaning of water from virtually all impurities belonging to various classes of organic substances. Peaks with yield times of 8.2, 8.7, 8.8, 10.5, 11.2, 14.0, and 20.0 min were attributed to an admixture of CH_2Cl_2. The peak observed at 13.0 min belongs to decane (internal standard).

For a quantitative characterization of the efficacy of water cleaning by the sorbents studied, we used the samples of industrial waste water. The initial chromatogram of this water presented in Fig. 2 displays about 150 peaks belonging to various aliphatic, cyclic, and aromatic compounds. For the analysis, we employed the part of the chromatogram corresponding to the retention times from 22 to 40 min (Fig. 3a). In this region, the total concentration of impurities amounted to 222.5 μg/l, including 215.5 μg/l of organochlorine compounds. This representative fraction was used for the subsequent investigation. The effect of sorbents is illustrated in Fig. 3b for fullerenes. The residual concentrations of organochlorine impurities in the samples of water treated with various solvents were as follows (μg/l): (i) 15.0, (ii) 42.0, (iii) 35.5, and (iv) 32.5.

The results of our experiments showed that all studied substances are effective sorbents, whose the action on a qualitative level is similar. In particular, all sorbents very weakly adsorbed polar molecules. It was established that the sorption properties of fullerenes could be related to the well-known features of their solubility [1]. This result is by no means surprising because the same intermolecular forces are operative in

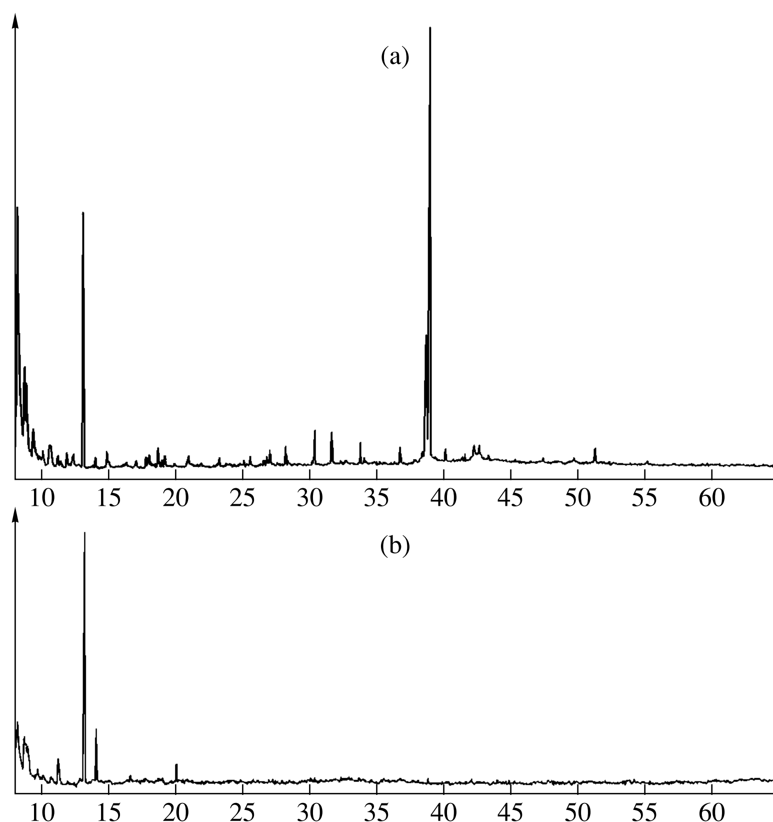

Fig. 1. Full-scale chromatograms of a natural river water sample (a) before and (b) after treatment with fullerene soot. Peaks with yield times of 8.2, 8.7, 8.8, 10.5, 11.2, 14.0, and 20.0 min belong to an admixture of CH_2Cl_2. The peak observed at 13.0 min belongs to decane (internal standard). The peaks at 38.6 and 38.9 min belong to palmitic acid and dibutylphthalate, respectively.

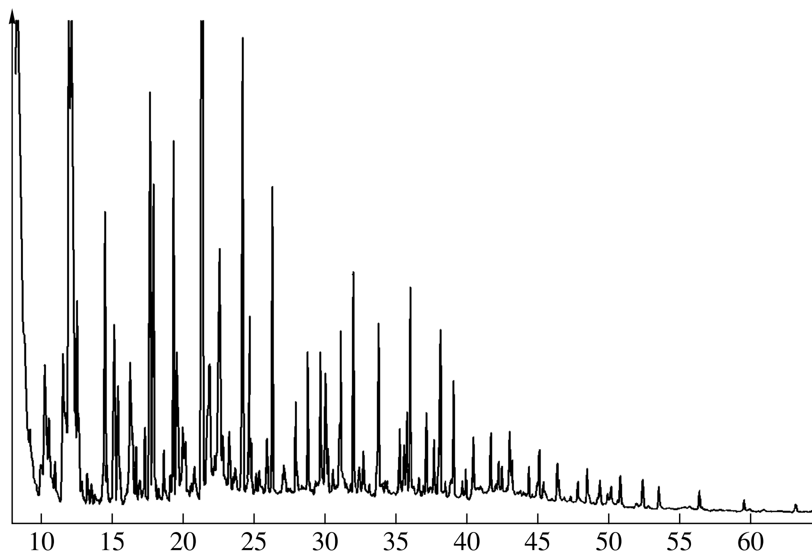

Fig. 2. Full-scale chromatogram of a sample of waste water from a pharmaceutical plant.

both adsorption and dissolution processes. Fullerenes, as well as soot and activated charcoal, virtually did not adsorb alkanes, acids, esters, and some other impurities from waste water. Quantitatively, activated charcoal proved to be a somewhat more effective sorbent as compared to soot. There are two interesting points to be specially noted. The first conclusion is that the effects of soot components (soot proper and fullerenes) are not additive. The second conclusion is that fullerenes are about ten times more effective sorbents than activated

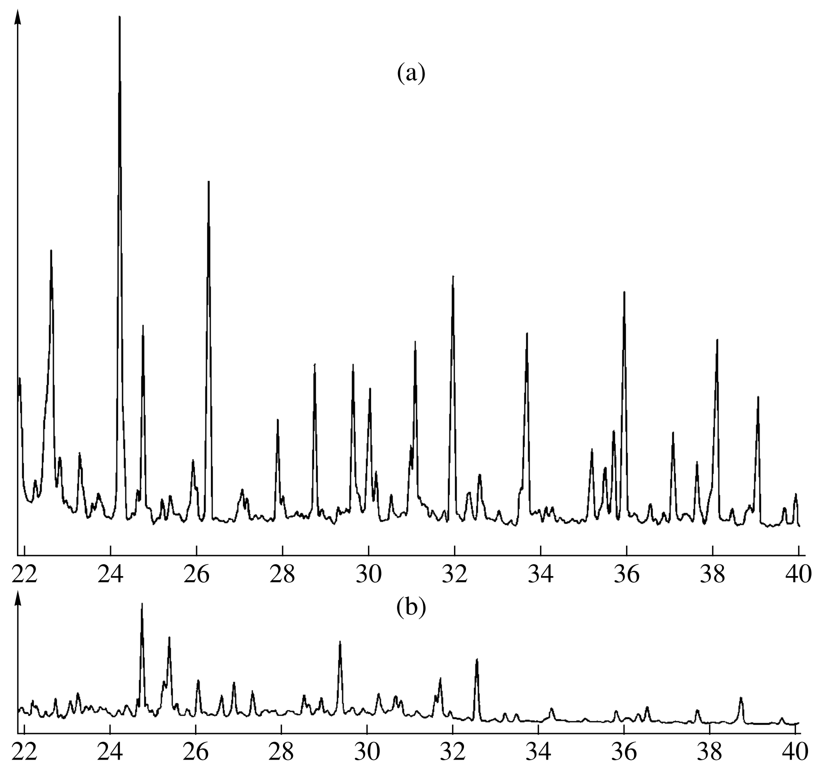

Fig. 3. Chromatograms of waste water from a pharmaceutical plant in the region of retention times from 22 to 40 min measured (a) before and (b) after treatment with fullerenes.

charcoal (taking into account the weight content of various sorbents in the tests).

In fullerene soot, fullerenes are probably bound to carbon particles and aggregates, which hinders the dissociation of fullerenes in solution. For this reason, the individual properties of fullerenes are not manifested: the fullerene soot component does not produce an additive sorption effect.

The efficacy of various sorbents depends on the particular mechanisms of sorption and on the specific area. The main mechanism of sorption for the physical adsorbents studied is related to the formation of van der Waals bonds at the phase boundaries (solid–liquid or solid–gas interfaces) between species (atoms, molecules, or their aggregates) of the adsorbent and adsorbate.

The main structural units of soot and activated carbons are loose graphitelike nanocrystals representing defective and distorted stacks of hexagonal carbon grids [2–4] with an average length of 2–3 nm and above and a thickness of 1.0–1.7 nm at a layer spacing of 0.34–0.37 nm. The main difference between various materials consists in the character of package of these crystallites. In this context, we may probably assume that the general mechanisms of adsorption on soot and activated carbons have much in common. Since these sorbents possess comparable specific areas (typically tens to hundreds m^2/g [2, 5]), their sorption capacities must also be very close, just as was confirmed by our experiments.

The stronger action of fullerenes can be related both to a greater specific area and to more effective sorption. Estimates of the specific area of C_{60} give 1.34×10^3 m^2/g. Since the fullerene adsorbent used in our experiments represented microcrystals, rather than separate molecules, the real specific surface was significantly lower than this estimate. For C_{60} microcrystals involving 10^6 and 10^9 molecules, the specific area can be estimated at 50 and 5 m^2/g, respectively.

As for the mechanism of sorption on fullerenes, there are two main variants. The first is via physical adsorption; the second, via breakage of carbon–carbon bonds in a fullerene molecule, followed by chemisorption. Since the energy of the double C=C bond is 615 kJ/mol [6], the latter variant is unlikely (our experiments were conducted at room temperature).

Attractive forces involved in the physical adsorption are divided into electrostatic and dispersive. The former are related to the presence of electric dipoles (polar molecules), quadrupoles, and higher multipoles in molecules related to both intrinsic and induced moments. The electrostatic interactions are divided into orientational and induction. The induction forces are operative when at least one of the interacting molecules (adsorbent or adsorbate) is polar.

An extremely low solubility of fullerenes in polar solvents is indicative of the role of the dipole–dipole interactions being insignificant (which is natural in

view of the symmetry of fullerene molecules and the absence of a dipole moment). The dipole-induced interaction must also play an insignificant role for fullerenes, which is confirmed by the following fact. While the molecular dipole moment increases in the series of fluoro- (dipole moment, 1.57 D), chloro- (1.69 D), bromo- (1.70 D), and nitrobenzene (4.22 D) (where 1 D = 3.34×10^{-30} C m) [7], the solubility of fullerene C_{60} in these substances (0.59, 7.00, 3.30, and 0.80 mg/ml, respectively [1]) varies without any correlation to the dipole moment of the solvent.

It was suggested that a relatively high solubility of fullerenes in aromatic substances can be due to a magnetic interaction of closed electron currents passing in the hexagonal molecules of both fullerenes and solvents [8]. At the same time, fullerenes (as well as most organic molecules) are diamagnetic (possess no constant magnetic moment). Therefore, there are no reasonable grounds for realization of the magnetic dipole interaction.

Some aromatic molecules (benzene, naphthalene, anthracene) possess considerable quadrupole moments [9]. In the molecules of fullerenes, the bonds between carbons atoms are not equivalent. Therefore, the charge distribution in these molecules exhibits local anisotropy and, hence, the fullerene fragments can also possess nonzero quadrupole electric moments (naturally, the total quadrupole moment of the fullerene molecule is zero). At temperatures above the phase transition temperature (249–260 K), C_{60} molecules can rotate in the lattice, which indicates that no fixed quadrupole interactions can take place under these conditions.

Thus, for sufficiently high temperatures, the sorption on fullerenes must proceed primarily via the physical adsorption mechanism mediated predominantly by the dispersive interaction forces. These interactions are of a universal character not related to the presence of stationary electric or magnetic moments. The dispersive forces act between atoms and molecules of any nature, irrespective of the molecular structure, and are realized by synchronization of the instantaneous dipoles arising in the interacting particles.

The binding energy of two C_{60} molecules was estimated at 2200–2900 K (0.19–0.25 eV) [10]. The heat of dissolution calculated for fullerenes in benzene, toluene, and CS_2 is about 10 kJ/mol (0.104 eV) [8]. The energy of cohesion for C_{60} in a crystal lattice, calculated per molecule with allowance for 12 nearest neighbors, is 1.6 eV [11]. The experimentally measured energy of sublimation for C_{60} at 400°C is 40 kcal/mol (1.74 eV) [12]. Our estimate of the energy of the adsorption interaction of C_{60} with a separate aromatic ring (benzene), calculated using the Lennard-Jones potential for carbon atoms, is 0.123 eV (in good agreement with the published data for fullerenes). At the same time, the characteristic energy of adsorption for an activated carbon and a standard vapor (benzene) amounts to 10–15 kJ/mol [13].

Assuming that the energies of adsorption for activated charcoals and fullerenes are on the same order of magnitude, the higher sorption efficacy of fullerenes should be explained with recourse to some other factors. In contrast to flat or elongated molecules, the molecules of fullerenes interact with the surrounding medium irrespective of their orientation. In other words, assuming that the molecules of adsorbate and adsorbent most effectively interact for a certain mutual arrangement, we may expect that an adsorbate molecule will find any possible arrangement, including the most favorable surface sites, on the spherical molecule of fullerene upon approaching the adsorbent to a sufficiently close distance. In addition, the carbon rings of fullerenes are free of defects, while the carbon rings of activated charcoal and soot are highly defective. This circumstance may influence the efficacy of generation of the instantaneous electric moments and the adsorption force field at the phase boundaries.

Acknowledgments. The authors are grateful to A.Ya. Vul' for formulation of the problem for this study and fruitful discussions. This work was supported within the framework of the State Scientific-Technological Program "Controlled Synthesis of Fullerenes and Other Atomic Clusters."

REFERENCES

1. R. S. Ruoff, D. S. Tse, R. Malhorta, *et al.*, J. Phys. Chem. **97** (13), 3379 (1993).
2. V. B. Fenelonov, *Porous Carbon* (Inst. Kataliza, Novosibirsk, 1995).
3. V. I. Berezkin, Phys. Status Solidi B **226** (2), 271 (2001).
4. H. Kienle and E. Bader, *Aktivkohle und ihre industrielle Anwendung* (Enke, Stuttgart, 1980; Khimiya, Leningrad, 1984).
5. *Production and Properties of Carbon Soots*, Ed. by V. F. Surovikin (Omsk, 1972).
6. L. Pauling, *General Chemistry* (Freeman, San Francisco, 1970; Nauka, Leningrad, 1974).
7. V. A. Rabinovich and Z. Ya. Khavin, *Concise Chemical Handbook* (Leningrad, 1977).
8. V. N. Bezmel'nitsyn, A. V. Eletskiĭ, and M. V. Okun', Usp. Fiz. Nauk **168** (11), 1195 (1998) [Phys. Usp. **41**, 1091 (1998)].
9. A. Cheng and M. L. Klein, Phys. Rev. B **45** (4), 1889 (1992).
10. A. Cheng and M. L. Klein, J. Phys. Chem. **95** (18), 6750 (1991).
11. S. Saito and A. Oshiyama, Phys. Rev. Lett. **66** (20), 2637 (1991).
12. H. S. Chen, A. R. Kortan, R. C. Haddon, *et al.*, J. Phys. Chem. **96** (3), 1016 (1992).
13. S. L. Glushakov, V. V. Konopleva, and N. G. Lyubchenko, *Activated Carbons: Catalogue* (Cherkassy, 1990).

Translated by P. Pozdeev

Technical Physics Letters, Vol. 28, No. 11, 2002, pp. 889–892. Translated from Pis'ma v Zhurnal Tekhnicheskoĭ Fiziki, Vol. 28, No. 21, 2002, pp. 22–28.
Original Russian Text Copyright © 2002 by Medvedkin.

Multivalent Substitution in a Quasi-Binary $Ga_{1-x}(II–Mn–IV)_xAs$ Solid Solution

G. A. Medvedkin

Ioffe Physicotechnical Institute, Russian Academy of Sciences, St. Petersburg, 194021 Russia

e-mail: G.A.Medvedkin@mail.ioffe.ru

Received May 16, 2002

Abstract—A process of the multivalent substitution of Mn atoms for cations in $Ga_{1-x}Mn_xAs$ (a base material) is proposed. According to this approach, the two-cation ternary compound with a chalcopyrite structure is used as a component forming a solid solution with GaAs. Based on the successful prediction and growth of high-temperature chalcopyrite ferromagnets, it is expected that the content of Mn in $Ga_{1-x}Mn_xAs$ can be increased. Quasi-binary $(GaAs)_{1-x}(ZnGeAs_2)_x$:Mn and $(GaAs_{1-x}(CdSiAs_2)_x$:Mn solid solutions are considered as candidate materials possessing higher Curie temperatures as compared to that of $Ga_{1-x}Mn_xAs$. *© 2002 MAIK "Nauka/Interperiodica".*

The development of spintronics requires new materials possessing ferromagnetic and semiconductor properties. A high potential of these materials can be realized provided they are compatible with the well-developed crystalline materials of semiconductor microelectronics, such as Si, Ge, GaAs, and InP. Gallium arsenide and AlGaAs solid solutions are already widely used as base materials for various optoelectronic devices (lasers, LEDs, photodetectors, etc.). Therefore, ensuring compatibility with these materials, with respect to both the crystal lattice parameters and technological characteristics (temperature, mutual solubility, solid solution formation, etc.), becomes one of the main problems encountered in the development of devices for high-temperature (as well as room-temperature) spintronics.

This Letter presents the concept of creation of a new generation of materials grown on the basis of quasi-binary solid solutions and doped with a magnetic impurity up to a level exceeding that reached to date in III–V semiconductor compounds such as GaAs and InGaAs.

The equilibrium solubility of magnetic impurities (Mn, Cr, Fe, etc.) in III–V semiconductor compounds is very small. In the course of the usual growth process, it is impossible to introduce a large number of such atoms into the crystal. It has been demonstrated that the ferromagnetic transition temperature in $Ga_{1-x}Mn_xAs$ depends on the magnetic impurity concentration as $T_C = 200x$ K in the interval $0 \le x \le 0.053$ ($0 \le [Mn] \le 5.3\%$). The maximum Curie temperature $T_C = 110$ K was achieved in $Ga_{1-x}Mn_xAs$ with [Mn] = 5.3% and a free hole concentration of $p = 3.5 \times 10^{20}$ cm^{-3}. For further increase in T_C, it is necessary to provide for a growth in the content of manganese atoms at a still high density of holes ($p > 5 \times 10^{20}$ cm^{-3}) and insure that $[Mn] > p$ [1–3].

As is known, direct introduction of Mn atoms into GaAs (e.g., by low-temperature molecular beam epitaxy, LTMBE) allows the impurity level to be increased up to 6–9% [4], while a special multilayer (digitated) deposition technique raises this level up to 14% [5, 6]. However, these methods are based on the monovalent substitution $Ga^{3+} \longrightarrow Mn^{2+}$ and, hence, cannot provide for an increase in the Curie temperature. Moreover, the T_C value of such nonequilibrium solid solutions exhibits depression rather than growth. An increase in the critical concentration level of [Mn] above 8–10% results in decomposition of the $Ga_{1-x}Mn_xAs$ solid solution with the formation of a second phase possessing a structure different from that of the zinc blende type. A decrease in the crystal lattice symmetry to hexagonal (NiAs type) or orthorhombic (MnP type) and "metallization" of the chemical bonds sharply deteriorate the optoelectronic properties of the material.

Previously [7–9], we reported that ternary chalcopyrite semiconductors of the II–IV–V_2 type can readily accept a high concentration of Mn atoms, which is a natural property of chalcopyrites used as two-cation semiconductors. This is accompanied by a strong ferromagnetic effect as a result of the bound manganese substitution in two-cation sublattices (e.g., for Cd and Ge in $CdGeP_2$). In such crystals, point defects are additionally included into exchange interaction with the spin system of manganese to supply charge carriers. Shortly after the experimental discovery of ferromagnetism in Mn-substituted chalcopyrites, ferromagnetic ordering was theoretically confirmed within the framework of various models, including those with point defects or sulfur impurity [10, 11]. At the same time, it is known

1063-7850/02/2811-0889$22.00 © 2002 MAIK "Nauka/Interperiodica"

Structural, optoelectronic, and magnetic properties of ternary II–IV–V_2 chalcopyrites and GaAs

Property	$CdGeP_2$	$ZnGeP_2$	$CdSiAs_2$	$ZnGeAs_2$	GaAs
Crystal structure*	Ch, ZB	Ch	Ch, ZB	Ch, ZB	ZB
a, Å	5.741	5.465	5.884	5.672	5.653
$c/2a$	0.938	0.985	0.925	0.983	1.0
μ	0.282	0.257	0.289	0.258	0.25
Bandgap	Direct	Indirect	Direct	Direct	Direct
E_g, eV	1.72	1.99	1.55	1.15	1.43
Δ_{cf}, eV	–0.20	–0.08	–0.29	–0.06	0.0
Δ_{so}, eV	0.11	0.09	0.29	0.31	0.34
Conductivity, $cm^2/(V\ s)$	*n*, *p*	*n*, *p*	*n*, *p*	*p*	*n*, *p*
	1500, 90	6, 100	–, 500	56	8500, 400
Solid solution with GaAs			Yes	Yes	Yes
Ferromagnetism (Mn substitution)	Yes	Yes		Yes	Yes
T_C, K	320	>350		300	110

* Ch, chalcopyrite; ZB, zinc blende; Δ_{cf} and Δ_{so}, the crystal-field and spin-orbit splitting of the valence band, respectively.

that related compounds of the III–V and II–IV–V_2 types with a common group V anion form a limited or unlimited series of solid solutions [12, 13].

Based on the close physicochemical nature of the two groups of compounds and on the recent results concerning room-temperature ferromagnetism in ternary chalcopyrites [9], we propose a concept of creating new ferromagnetic materials. According to this, GaAs (the base material) can be doped by manganese through multivalent substitution up to a level of concentrations exceeding that reached to date. The concept stipulates the following stages:

(i) Selecting a base material for realization of a desired function, for example, high-temperature ferromagnetism in $Ga_{1-x}Mn_xAs$.

(ii) Selecting a compound capable of forming a solid solution with GaAs, for example, $ZnGeAs_2$ or $CdSiAs_2$.

(iii) Growing a solid solution with multivalent substitution of Mn to a level exceeding that in Mn-doped III–V compounds.

Note that the aforementioned condition of [Mn] > p is automatically satisfied in both (III, Mn)V and (II, Mn, IV)V_2 compounds because only a part of the Mn atoms (involved into nonisovalent substitution) will serve as acceptors, while the other atoms (isovalent substitution) will occur in the 2+ and 4+ valence states.

The properties of GaAs and related compounds of the II–IV–V_2 type, either realized in Mn-substituted ferromagnetic chalcopyrites or anticipated in solid solutions and/or epitaxial heterojunctions, are summarized in the table. The most acceptable technologies for these purposes include MBE, metalorganic MBE (MOMBE), metalorganic vapor-phase epitaxy (MOVPE), and chemical vapor deposition (CVD). According to the concept proposed, the new materials based on GaAs are described by chemical formulas of the type

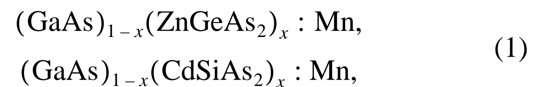

$$(GaAs)_{1-x}(ZnGeAs_2)_x : Mn, \quad (GaAs)_{1-x}(CdSiAs_2)_x : Mn, \tag{1}$$

where x varies within the interval from 0 to 0.2, which is usually sufficient to provide for a 5–10% substitution of Mn. Using the proposed approach, the other possible cross combinations of cations (e.g., 2Zn $\longleftrightarrow$ Cd $\longleftrightarrow$ Mg and 4Si $\longleftrightarrow$ Ge $\longleftrightarrow$ Sn) can also be considered and realized for arsenides and phosphides.

For solid solutions occurring in a quasi-binary section on the GaAs side of the phase diagram, the above formulas can be written in a simpler form as

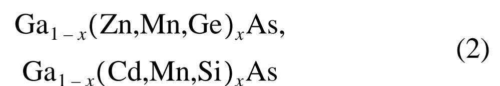

$$Ga_{1-x}(Zn,Mn,Ge)_xAs, \quad Ga_{1-x}(Cd,Mn,Si)_xAs \tag{2}$$

or as other cross combinations satisfying the octet rule for covalent electrons.

In solid solutions of type (1), Mn atoms occupy the structural positions of Ga and the Zn + Ge bound cation positions. In the Ga^{3+} and Zn^{2+} positions, manganese atoms occur in the 2+ valence state (Mn^{2+}) and act as an acceptor replacing gallium. In the Ge^{4+} positions, manganese atoms must occur in the 4+ or 3+ valence state

(Mn^{4+} or Mn^{3+}) and act as additional acceptor centers. Chemical formulas (2) emphasize that the main substitution in cationic sublattices proceeds at the expense of the ternary compound. This reflects the real situation of significantly different equilibrium concentrations of Mn entering into sphalerite and chalcopyrite structures. For this reason, the high-temperature ferromagnetic state can be attained either by introducing high concentrations of Mn atoms and holes or by using a mechanism specific to the chalcopyrite structure.

It should be noted that this approach cannot be considered merely as codoping [14], since both doping and chemical substitution functions are performed by the same element (Mn), albeit in a system with the GaAs–$ZnGeAs_2$ quasi-binary section. The introduction of manganese into GaAs via a ternary compound of the II–IV–V_2 type is a nontrivial process representing multivalent substitution, for which codoping is another particular case of mediation by two chemical elements. In the case of a single element, the effect can be reached only via true multivalent substitution mediated by a chemical element possessing several allowed valence states, for example, by a *d* or *f* transition element.

An analogous multivalent state is realized for Cr in the $CdCr_2Se_4$ ternary compound, for manganites, and, probably, for the binary Eu-substituted chalcogenides. However, among all the aforementioned semiconductor compounds, only chalcopyrites of the II–IV–V_2 type crystallize in a diamondlike structure (space group D_{2d}^{12} or T_d^2) and are readily compatible with III–V crystals (space group T_d^2 or D_{2d}^{12}).[1] Most ternary chalcopyrites can be successfully doped with intrinsic point defects or with foreign impurities to obtain conductivity of the *n* or *p* types. Related crustal structures and space symmetry groups provide for ideal epitaxial growth of both thick single crystal layers and low-dimensional (2D, 1D, 0D) systems on III–V substrates.

A heterojunction of the GaAs–$Ga_{1-x}(Zn,Ge)_xAs$ type showing ideal crystallographic matching in the *z* axis direction is schematically depicted in the figure. Since the value of $c/2a$ for $ZnGeAs_2$ (a pure chalcopyrite) is very close to 1.0 (see table), the lattice mismatch in the directions of the *a* and *b* axes for an epitaxial layer of the solid solution will also be very small, $2\Delta a/a < 0.3\%$ (i.e., close to zero for a small *x* and a structure of T_d^2 symmetry). Note the alternation of Zn and Ge atoms, as well as of the (Zn,Ge)–Ga pairs, in each subsequent layer. When Mn atoms are introduced by means of multivalent substitution, the positions of Ga, Zn, and Ge cations are occupied in accordance with the allowed valence states of manganese. The crystal lattice of type T_d^2 or D_{2d}^{12} will be retained, at least for the total concentration of cations such that [Ga] + [Zn] + [Ge] > [Mn]. This condition was experimentally confirmed for both III–V (with [Mn] not lower than 5–6%) [1–3] and II–IV–V_2 ([Mn] not lower than 20%) [7–10].

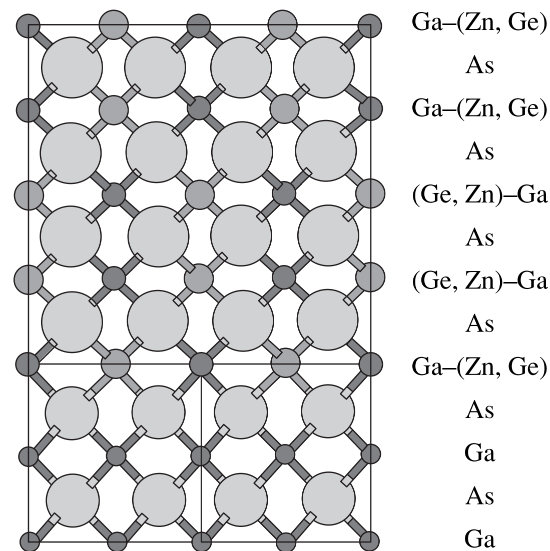

Schematic diagram of a heterojunction of the GaAs–$Ga_{1-x}(Zn,Ge)_xAs$ type in the *z* axis direction showing the alternation of cations in the solid solution layers (for a 5% substitution in the cationic sublattice of gallium).

The proposed concept of multivalent substitution is based on the achievements made in the technology of binary/ternary III–V/II–IV–V_2 semiconductor compounds and the recent discovery of ferromagnetic (II,Mn,IV)–V_2 chalcopyrites such as $(Cd,Mn,Ge)P_2$, $(Zn,Mn,Ge)P_2$, and $(Zn,Mn,Ge)As_2$ solid solutions and some others. There are no evident obstacles to the growth of solid solutions of the $Ga_{1-x}(Zn,Mn,Ge)_xAs$ type, and we expect that these materials will feature ferromagnetism with T_C above 110 K.

Acknowledgments. This study was supported by a grant from Deutsche Forschungsgemeinschaft within the framework of the "II–VI Tunnel Structures for Spin Injection" project (2002).

[1] A chalcopyrite structure of D_{2d}^{12} symmetry is realized upon ordering of the III and III' group cations, for example, in $GaInAs_2$.

REFERENCES

1. H. Ohno, J. Magn. Magn. Mater. **200**, 110 (1999).
2. T. Dietl and H. Ohno, Physica E (Amsterdam) **9**, 185 (2001).
3. T. Dietl, H. Ohno, and F. Matsukura, Phys. Rev. B **63**, 195205 (2001).
4. A. van Esch, L. van Bockstal, J. De Boeck, *et al.*, Phys. Rev. B **56** (20), 13103 (1997).
5. J. Sadowski, R. Mathieu, P. Svedlindh, *et al.*, Appl. Phys. Lett. **78** (21), 3271 (2001).

6. K. Sato, in *Crystal Growth and Characterization of Magnetic Semiconductors: Proceedings of the 11th International Summer School on Crystal Growth, 2001,* Invited Lecture; R. Misawa, M.S. Thesis (Tokyo Univ. A&T) (unpublished).
7. G. A. Medvedkin, T. Ishibashi, T. Nishi, *et al.*, Jpn. J. Appl. Phys. **39** (10A), L949 (2000).
8. G. A. Medvedkin, T. Ishibashi, T. Nishi, and K. Sato, Fiz. Tekh. Poluprovodn. (St. Petersburg) **35** (3), 305 (2001) [Semiconductors **35**, 291 (2001)].
9. K. Sato, G. A. Medvedkin, T. Nishi, *et al.*, J. Appl. Phys. **89** (11), 7027 (2001).
10. P. Mahadevan and A. Zunger, Phys. Rev. Lett. **88** (4), 047205 (2002).
11. Y.-J. Zhao, S. Picozzi, A. Continenza, *et al.*, Phys. Rev. B **65**, 094415 (2002).
12. $A_2B^4C_5^2$ *Semiconductors*, Ed. by N. A. Goryunova and Yu. A. Valov (Sov. Radio, Moscow, 1974).
13. J. L. Shay and J. H. Wernick, *Ternary Chalcopyrite Semiconductors* (Pergamon, Oxford, 1975).
14. T. Yamamoto and H. Katayama-Yoshida, Jpn. J. Appl. Phys., Part 2 **38**, L166 (1999).

Translated by P. Pozdeev

Technical Physics Letters, Vol. 28, No. 11, 2002, pp. 893–895. Translated from Pis'ma v Zhurnal Tekhnicheskoĭ Fiziki, Vol. 28, No. 21, 2002, pp. 29–35.
Original Russian Text Copyright © 2002 by Betekhtin, Gorobeĭ, Korsukov, Luk'yanenko, Obidov, Tomilin.

Features of Defect Formation on a Deformed Si(111) Surface

V. I. Betekhtin*, N. N. Gorobeĭ, V. E. Korsukov, A. S. Luk'yanenko, B. A. Obidov, and A. N. Tomilin

Ioffe Physicotechnical Institute, Russian Academy of Sciences, St. Petersburg, 194021 Russia

** e-mail: Vladimir.Betekhtin@pop.ioffe.rssi.ru*

Received May 22, 2002

Abstract—Dynamics of the surface relief on a Si(111) single crystal face of a sample subjected to biaxial lateral extension after mechanical or chemical polishing was studied using scanning tunneling microscopy. In both cases, despite certain differences, the sample surface shows evidence of relief dynamics on a nanometer scale and exhibits a fractal character of the spatial structure formed in late stages of the process. *© 2002 MAIK "Nauka/Interperiodica".*

As is known, the surface layers of solids differ from bulk with respect to many physical parameters and structure [1]. This is manifested, in particular, in a lower mechanical strength of the surface. Therefore, we may expect that the process of defect formation under mechanical action proceeds on the surface at a higher rate than in the bulk. The main distinctive feature of the surface is the presence of a free boundary, which opens new channels of defect structure formation related primarily to the dynamics of the surface relief. The development of modern methods for surface analysis has made it possible to study the evolution of defect structures on a previously inaccessible nanometer level, which is especially important for the physics of strength and plasticity.

We have used the method of scanning tunneling microscopy (STM) to study the process of defect formation on a Si(111) single crystal surface subjected to isotropic lateral extension. Previously [2, 3], we observed and analyzed quasi-reversible effects in the surface relief dynamics on a deformed Ge(111) surface, which were suggested to be related to a diffusion mass transfer in the mechanical force field. These effects are analogous to those observed in the course of heteroepitaxy, for example, during the deposition of germanium onto a silicon substrate [4]. However, the possible pathways of the surface structure formation are not restricted to the diffusion kinetics. Plastic deformation of the surface layers of semiconductor crystals on a micron level (microplastics) has also been observed and considered in sufficient detail [5]. The effects observed in the relief dynamics on a deformed Si(111) surface show evidence that the microplastics is accompanied (and, probably, preceded) by the surface structure dynamics on a nanometer level.

We have studied the Si(111) surfaces of samples prepared by different methods involving mechanical and chemical polishing. The experimental procedure, including the sample preparation and mechanical loading, was described in detail elsewhere [2]. Figure 1 shows typical STM profiles of a deformed Si(111) surface prepared by mechanical grinding followed by chemical polishing. The chemical treatment removes,

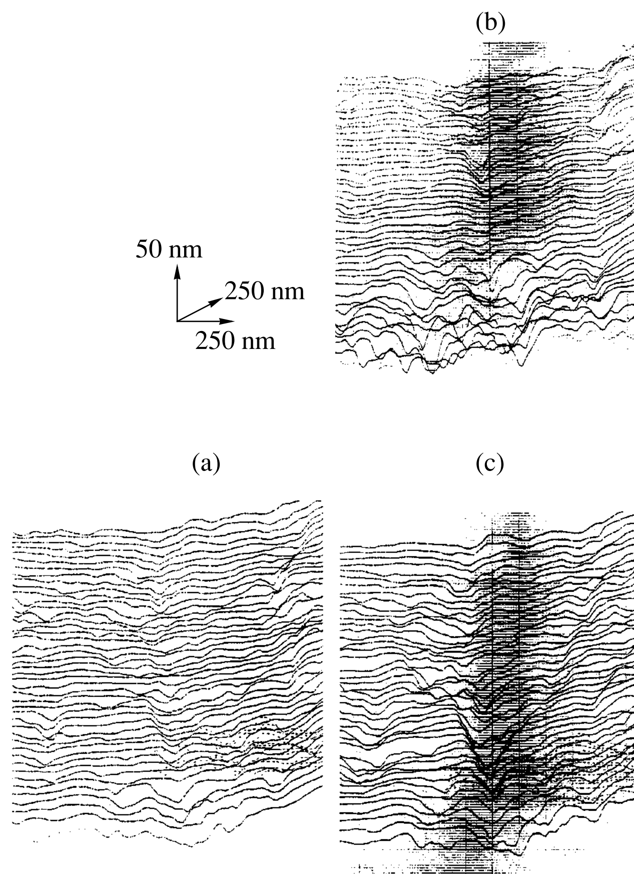

Fig. 1. STM profiles illustrating the effect of biaxial extension on the Si(111) surface relief upon chemical polishing: (a) initial surface ($t = 0$); (b, c) sample loaded with $\sigma = 0.1$ GPa for $t = 10$ and 40 min, respectively.

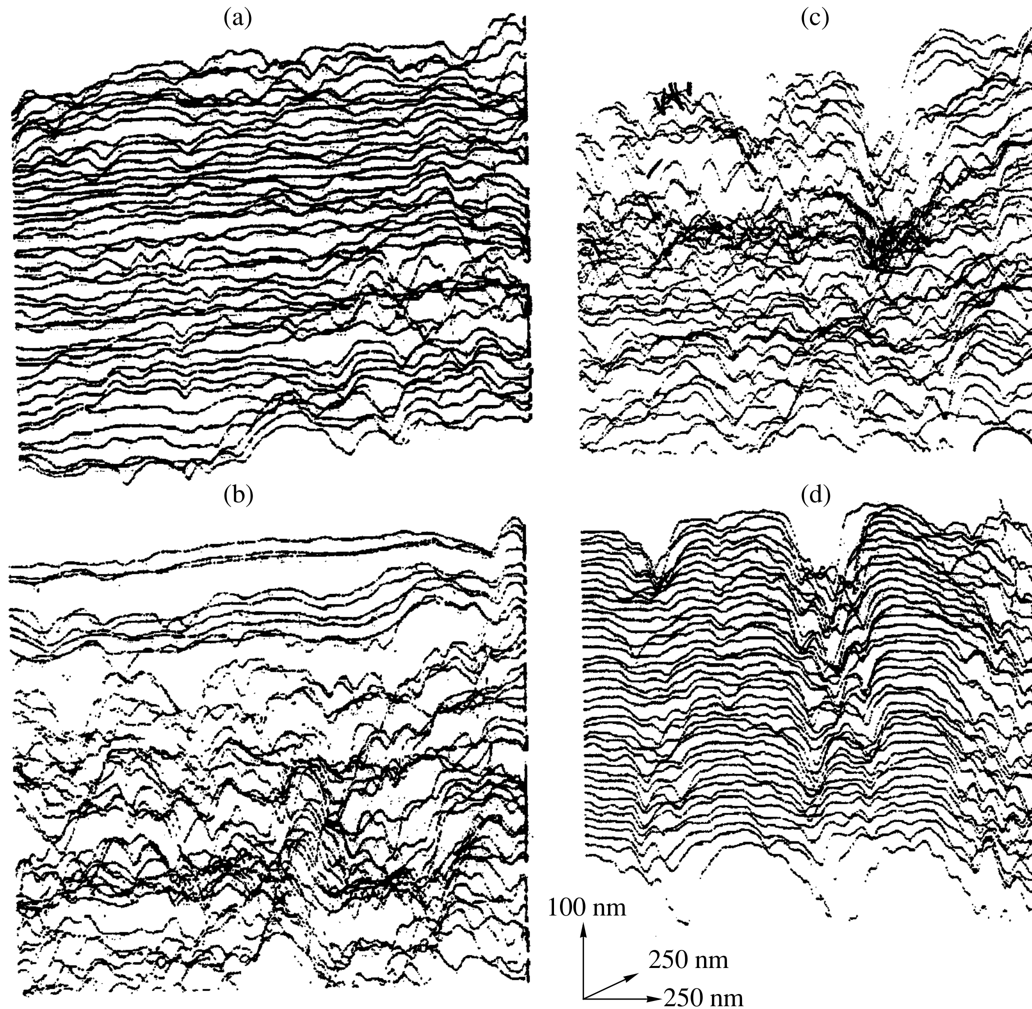

Fig. 2. STM profiles illustrating the effect of biaxial extension on the Si(111) surface relief upon mechanical polishing: (a) initial surface ($t = 0$); (b–d) sample loaded with $\sigma = 0.1$ GPa for $t = 20$, 40, and 50 min, respectively.

to a considerable extent, the layer damaged by mechanical grinding, so that the scenario observed in this case can be referred to as initially defectless. As can be seen, the initially smooth sample surface (Fig. 1a) becomes rough already after a 10-min loading at about 50 MPa (Fig. 1b).

In this series of experiments, we traced the nucleation and development of one microdefect representing a pit in the surface relief at the center of the area scanned. The density of such micron-sized defects is on the order of $\sim 10^6$ cm^{-2}, which agrees with the data reported recently [3]. However, the experimental STM profiles also reveal dynamics in the surface relief at a site adjacent to the above microdefect, where the process is developed on a nanometer level. Upon taking into account such features in the relief, with lateral dimensions on the order of tens and hundreds of nanometers, the total defect density would increase by two to three orders of magnitude. This relief dynamics, considered as a manifestation of the plastic deformation of the sample surface, can be referred to as nanoplastics. Obviously, the relief dynamics on various dimensional levels cannot be considered as independent processes. Since the crystal bulk occurs in the elastically deformed state, plastic shear in the surface layers must begin and end on the same surface. Therefore, the formation of surface macrodefects has to be accompanied by a certain dynamics on the adjacent areas, which is observed in the form of nanoplastics.

A different scenario of evolution of the surface structure was observed for an initially defective surface. Such areas can be found even on a chemically polished sample. However, the initially defective scenario is most clearly pronounced on a mechanically polished Si(111) surface not subjected to subsequent chemical polishing (Fig. 2). Here, the surface layer with a thickness of about 1 μm is initially damaged and it is interesting to follow the dynamics of this relief in the course of the subsequent mechanical deformation. As can be seen on the background of evident plastic shear, the

relief dynamics in this case begins on a nanometer level as well. The process expands over the entire scanned surface area and continues on a micron level, after which the pattern exhibits stabilization.

Thus, before attaining stabilization on a micron level, the defect structure existing in the surface layer is first "rearranged" on the nanometer and, probably, atomic levels. Note a tendency to the formation of a self-similar spatial relief structure in a late stage of the surface dynamics. The self-similarity is qualitatively manifested in the fact that the relief structure (see Fig. 2c) contains defects of all levels (encountered at the corresponding frequency) from nanometer to micron dimensions and this character is retained upon increasing the STM resolution. Recently, the appearance of fractal structures was observed for the dynamics of dislocation pile-ups [6]. Apparently, the observed relief dynamics reflects the evolution of the surface layer structure, which is accompanied by intensive mass transfer. However, neither a monoatomic diffusion mechanism nor the usual mechanisms of the theory of plasticity seem to be capable of adequately explaining the whole pattern of dynamics observed on the deformed crystal surface.

Irrespective of the mechanisms determining the dynamics of the defect surface structure, the main driving force of the relief formation is expressed by the principle of minimum energy. This principle underlies theoretical analysis of the process of heteroepitaxy, where the relief formation is determined by misfit stresses arising between epitaxial layer and substrate [4]. The epitaxial process also involves two competitive dynamic mechanisms: surface diffusion and plastic deformation. We employed the principle of minimum energy for analysis of the relief dynamics in the case of direct mechanical loading of the sample surface. The results of this analysis showed that, for a certain geometry of the deformed relief, the energy is really gained as a result of the elastic strain energy release in the surface layer, but with an allowance for a certain growth in the energy due to an increase in the surface area. Similarly to the case of heteroepitaxy, it is a question of kinetics to determine the pathways to reach the state of minimum energy.

Thus, the defect formation on a deformed solid surface is a process involving all levels of the crystal structure: micron, nanometer, and, probably, atomic. A general trend on a mechanically deformed crystal surface is the growth of fractal dimensionality [7], which is indicative of the formation of a defect structure containing, with high probability, the sites of nucleation of a macroscopic damage from which the fracture proceeds deep into the bulk.

Acknowledgments. This study was supported by the Russian Foundation for Basic Research, project no. 2000-00-00482.

REFERENCES

1. B. A. Nesterenko and O. V. Snitko, *Physical Properties of Atomically Clean Surface of Semiconductors* (Naukova Dumka, Kiev, 1983).
2. S. N. Zhurkov, V. E. Korsukov, A. S. Luk'yanenko, *et al.*, Pis'ma Zh. Éksp. Teor. Fiz. **51** (6), 324 (1990) [JETP Lett. **51**, 370 (1990)].
3. N. N. Gorobeĭ, S. A. Knyazev, V. E. Korsukov, *et al.*, Pis'ma Zh. Tekh. Fiz. **28** (1), 54 (2002) [Tech. Phys. Lett. **28**, 23 (2002)].
4. I. Tersoff and F. K. LeGones, Phys. Rev. Lett. **72** (22), 3570 (1994).
5. V. P. Alekhin, *Physics of Strength and Plasticity of Surface Layers of Materials* (Nauka, Moscow, 1983).
6. M. S. Bharathi, M. Lebyodkin, G. Ananthakrishna, *et al.*, Phys. Rev. Lett. **87** (16), 165508 (2001).
7. V. I. Betekhtin, P. N. Butenko, V. L. Gilyarov, *et al.*, Pis'ma Zh. Tekh. Fiz. **28** (1), 60 (2002) [Tech. Phys. Lett. **28**, 26 (2002)].

Translated by P. Pozdeev

Technical Physics Letters, Vol. 28, No. 11, 2002, pp. 896–898. Translated from Pis'ma v Zhurnal Tekhnicheskoĭ Fiziki, Vol. 28, No. 21, 2002, pp. 36–41.
Original Russian Text Copyright © 2002 by Grishchuk, Davidenko, Zholner, Verbitskii, Kurik, Piryatinskii.

Optical Absorption and Luminescent Properties of Melanin Films

V. P. Grishchuk, S. A. Davidenko, I. D. Zholner, A. B. Verbitskii, M. V. Kurik, and Yu. P. Piryatinskii

"Ukrenergoresursy" Joint-Stock Company, Kiev, Ukraine

Institute of Physics, National Academy of Sciences of Ukraine, Kiev, Ukraine

e-mail: avsky@iop.kiev.ua

Received April 1, 2002

Abstract—The optical absorption and luminescence spectra of the films of natural melanin were measured. The results are explained based on a nanocluster structure of the films. *© 2002 MAIK "Nauka/Interperiodica".*

The natural pigment melanin plays an important role in living organisms, including humans. In particular, melanin acts as a UV protector and participates in many physiological and psychic processes. However, the mechanism of the interaction of this compound with UV radiation, as well as the contributions of melanin to complicated processes, is still unknown. Knowledge of the physical properties, including the electron structure, of melanin is probably a key to understanding the role this compound plays in the human organism.

Melanin, as a substance possessing semiconductor properties, has been known since 1974, when McGinnes *et al.* [1] established that this compound exhibits the effect of switching from weakly to highly conducting state under the action of relatively small electric fields. Recently, Rosei *et al.* [2] studied the spectral and photoelectric properties of synthetic melanin and proposed a mechanism explaining the photoproduction of charge carriers.

The purpose of our study was to measure the absorption spectra of natural melanin, the effect of UV irradiation on the samples, and the photoluminescence at room and low (liquid helium) temperatures.

The experiments were performed with melanin extracted from raw plant material. In respect to the structure, the extracted substance was close to synthetic melanin based on a 5,6-indolequinone monomer [2], as confirmed by the results of chromatographic measurements and elemental analyses. The sample films were prepared by applying a melanin solution (in alcohol possessing a complicated molecular structure) onto quartz substrates at room temperature.

The absorption spectrum of melanin measured in the visible spectral range (Fig. 1, curve *1*) exhibit a monotonic decrease from 375 to 800 nm. This shape of the absorption spectrum was explained [2] as resulting from a disordered structure of the melanin film composed of elementary nanodimensional two-dimensional clusters packed into stacks. According to this model, the absorption spectrum of melanin is explained by the π–π^* electron transitions inside nanoclusters. The observed absorption spectrum is untypical of organic compounds, being closer in shape to the spectra of disordered amorphous inorganic semiconductors [3].

For comparison, Fig. 1 shows the absorption spectra of a melanin film irradiated for 1.5 h by nonfiltered polarized light of a mercury lamp (DRSh-250-2). The measurements were performed using a beam polarized in directions parallel (curve *2*) and perpendicular (curve *3*) to that of the irradiating light. As can be seen, the irradiation does not modify the character of the spectrum on the whole: there is only an insignificant change in the slope and a small (5–15%) decrease in the absorption coefficient in the region of 375–400 nm. The latter decrease depends on the polarization, being more pronounced for the spectrum measured using

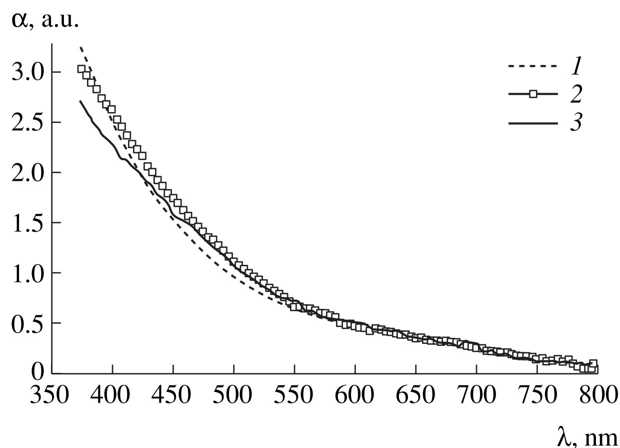

Fig. 1. The optical absorption spectra of (*1*) unirradiated and (*2*, *3*) UV-irradiated melanin films measured using (*2*) parallel and (*3*) perpendicular polarization of the probing beam.

1063-7850/02/2811-0896$22.00 © 2002 MAIK "Nauka/Interperiodica"

light polarized in the perpendicular direction. This result is additional evidence of the absence of linear structures typical of most polymers.

Using the measured absorption spectrum (Fig. 1, curve *1*), we estimated the optical bandgap width E_g^{opt} of melanin. This was done using the Tautz law, according to which the plot of $(\alpha E)^{1/2}$ versus energy E for amorphous solids with three-dimensional electron states must be linear. By extrapolating this plot to the abscissa axis, it is possible to determine the E_g^{opt} value of such a disordered substance [3].

Since the melanin films studied also possessed a disordered structure, it was possible formally to employ the Tautz formula [2, 3]. However, the plots of $(\alpha E)^{1/2}$ versus energy E in our case (unlike that reported in [2]) were not strictly linear. To a first approximation, the experimental curve could be divided into two linear parts, the extrapolation of which yields E_g^{opt} ~ 1.4 and ~1 eV. Using an exponent of 0.3 instead of 0.5 (as was done, e.g., in [4]) provided a better linearization of the experimental data, in which case we obtained E_g^{opt} = 1.2 ± 0.2 eV. This change in the exponent was justified [4] as resulting from fluctuations (scatter) in the dimensions of nanoparticles. It should also be noted that, as was correctly indicated, e.g., in [5], the estimated energy corresponds, strictly speaking, to a minimum energy of the π–π* electron transition (π–π* gap) [5].

According to the most commonly accepted model [6], the dependence of the change in the optical bandgap width (π–π* gap) on the size of nanoparticles (conjugation length) is described by the relation $\Delta E_g^{opt} \sim C/d^2$, where C is a constant and d is the particle diameter. Using this relation, it is possible to estimate the ratio of the size of nanoclusters corresponding to the two estimates of E_g^{opt} : $d_2/d_1 = (E_{g1}^{opt}/E_{g2}^{opt})^{0.5} = 0.85$. From this we may conclude that the films studied exhibit a bimodal distribution of nanocluster dimensions with two most probable values (conjugation lengths).

This conclusion is confirmed by the results of measurements of the photoluminescence (PL) spectra of melanin films at 5 and 300 K (the experimental procedure was described in detail elsewhere [7]). Figure 2 presents the spectra of stationary and time-resolved PL (the latter measured at a nanosecond delay time). As can be seen, the room-temperature stationary PL spectrum consists of two intense narrow bands peaking at 375 and 440 nm and a broad structureless band with a maximum at about 660 nm (Fig. 2, curve *1*). In the time-resolved PL spectrum (measured at a nanosecond resolution), the intensity of the narrow bands somewhat decreases and the broad band disappears (Fig. 2, curve *2*). The spectra of stationary and time-resolved PL measured at liquid-helium temperature differ rather

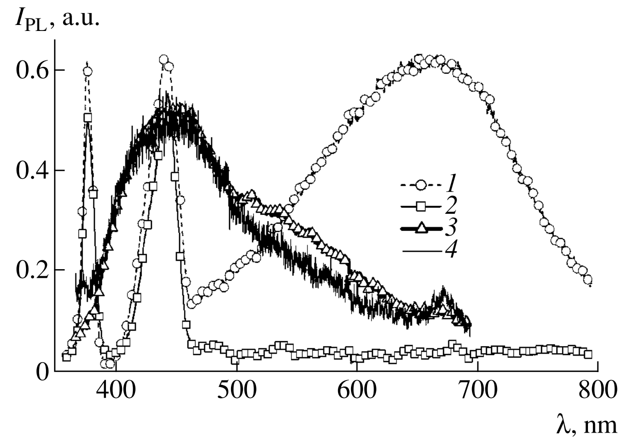

Fig. 2. The spectra of (*1*, *3*) stationary and (*2*, *4*) time-resolved (t_d = 3 ns) photoluminescence of a melanin film measured at (*1*, *2*) 300 K and (*3*, *4*) 5 K.

slightly from each other (Fig. 2, curves *3*, *4*). In comparison to the corresponding room-temperature spectra, the intensity of the band at 375 nm drops to almost zero and the band at 440 nm exhibits a significant broadening. The band at 660 nm is absent from both PL spectra measured at 5 K.

The results of our PL measurements can be interpreted as follows. The narrow emission bands correspond to the excitation of nanoclusters of the two most probable dimensions and represent the electron transitions inside these clusters (between their fragments). For this reason, these bands are observed in both stationary and time-resolved PL spectra. Note that the ratio of the energies of these bands (0.85) coincides with the estimate of the ratio of the most probable dimensions of nanoclusters. The broad structureless band, manifested only in the room-temperature stationary PL spectrum, probably reflects the interaction of structural elements (clusters) with each other and is due to the excimer radiation. A similar pattern is observed, for example, in many conjugated polymers where the PL spectra contain narrow bands caused by emission from conjugated fragments and broad structureless bands with rather large lifetimes (>1 μs) caused by excimer (dimer) radiation [8].

At low temperatures, one (less stable) type of nanocluster is probably subject to irreversible breakage, which accounts for the disappearance of the emission band at 375 nm. A change in the structure of melanin, manifested in an increase in the homogeneity of the film, can be observed using an optical microscope.

Thus, the results of investigation of the absorption and photoluminescence spectra of melanin show that a film of this natural biomolecular semiconductor is composed of stacked nanoclusters (manifested by the presence of excimer radiation). This nanocluster structure with two most probable cluster types probably deter-

mines the physical properties of this compound, in particular, the phenomenon of switching [1].

REFERENCES

1. J. McGinnes, P. Corry, and P. Proctor, Science **183**, 853 (1974).
2. M. A. Rosei, L. Mosca, and F. Galuzzi, Synth. Met. **76**, 331 (1996).
3. N. F. Mott and E. A. Davis, *Electronic Processes in Non-Crystalline Materials* (Clarendon, Oxford, 1979; Mir, Moscow, 1982).
4. V. N. Novikov, A. P. Sokolov, O. A. Golikova, *et al.*, Fiz. Tverd. Tela (Leningrad) **32** (5), 1515 (1990) [Sov. Phys. Solid State **32**, 884 (1990)].
5. E. A. Konshina, Fiz. Tverd. Tela (St. Petersburg) **37** (4), 1120 (1995) [Phys. Solid State **37**, 610 (1995)].
6. Y. Wang, A. Suna, W. Mahler, *et al.*, J. Chem. Phys. **87** (12), 7315 (1987).
7. Yu. P. Piryatinskii and O. V. Yaroshchuk, Opt. Spektrosk. **89** (6), 937 (2000) [Opt. Spectrosc. **89**, 860 (2000)].
8. M. Furukawa, K. Mizuno, A. Matsui, *et al.*, J. Phys. Soc. Jpn. **58** (8), 2976 (1989).

Translated by P. Pozdeev

Technical Physics Letters, Vol. 28, No. 11, 2002, pp. 899–901. Translated from Pis'ma v Zhurnal Tekhnicheskoĭ Fiziki, Vol. 28, No. 21, 2002, pp. 42–47.
Original Russian Text Copyright © 2002 by Skakun, Lomaev, Tarasenko, Shitts.

KrCl and XeCl Exciplex Glow Discharge Lamps with an Output Power of ~1.5 kW

V. S. Skakun, M. I. Lomaev, V. F. Tarasenko, and D. V. Shitts

Institute of High-Current Electronics, Siberian Division, Russian Academy of Sciences, Tomsk, Russia

e-mail: VFT@loi.hcei.tsc.ru

Received May 31, 2002

Abstract—A high-power multisection cylindrical exciplex lamp pumped by a glow discharge is created. The energy, temporal, and spectral characteristics of the emission from KrCl* (λ ~ 222 nm) and XeCl* (λ ~ 308 nm) molecules are studied. The average output UV radiation power is 1.6 kW (for 222 nm) and 1.1 kW (for 308 nm) at a power pumping efficiency of up to 14%. *© 2002 MAIK "Nauka/Interperiodica".*

Introduction. Previously [1–4], we reported on the creation of coaxial and cylindrical KrCl and XeCl exciplex lamps (excilamps) pumped by a stationary glow discharge, which were characterized by an average output power of 100–200 W in the UV spectral range. This type of discharge was originally used for pumping cylindrical excilamps in [5, 6], where a mixture of krypton or xenon with the halogen (Cl_2) was excited and an average output power of ~8 W at an efficiency of up to 12% was obtained for the emission from KrCl* and XeCl* molecules, respectively.

Subsequent investigations of the glow discharge excitation regime [7] showed that maximum efficiencies of the excilamps are achieved by using excitation voltage pulses of millisecond duration and a certain shape. It was also demonstrated [8] that maximum output powers are achieved by adding light inert gases (helium, neon) to the Kr(Xe)–Cl_2 mixtures. The spontaneous emission sources operating on exciplex molecules, which generate radiation in relatively narrow UV and VUV bands, can find application in various fields of science and technology.

Here, we report for the first time on the creation of KrCl (λ ~ 222 nm) and XeCl (λ ~ 308 nm) exciplex glow discharge lamps with an average output power above 1 kW, which is more than five times higher than the level achieved previously. The radiation is emitted from plasma of a positive column of the glow discharge excited in a cylindrical tube.

Experimental. Figure1 shows a photograph of the emitter unit of a new excilamp. The emitter comprises three parallel branches, each including four sections (to a total of 12) representing cylindrical quartz tubes with 2.5-mm-thick walls. The dimensions of one section of the excilamp are as follows: length, ~100 cm; external diameter, 52 mm (for single branches) or 56 mm (for double branches). Each branch of the excilamp is powered from a separate high-voltage source; each section of the lamp can be switched on independently by shunting the other sections.

The given experimental system was air cooled; replacing the air cooling system by a water jacket decreases dimensions of the excilamp but significantly complicates the emitter design. Each power source, consisting of a transformer and a voltage regulator, produced a sinusoidal voltage of commercial frequency (50 Hz) with an amplitude of up to 20 kV (smoothly controlled) and a power of up to 7 kW. This design of the emitter and the power supply system probably offers the simplest variant ensuring an average output power of 1 kW or greater.

The output radiation power was measured using a calibrated FEK-22 SPU photodetector sequentially moved along each branch of the excilamp. The pulses of current and voltage in the lamp, as well as of the output emission intensity, were measured using current probes, voltage dividers, FEK-22 SPU, and a TDS-224 oscillograph. The glow discharge was photographed using a digital camera. The working gas mixtures of

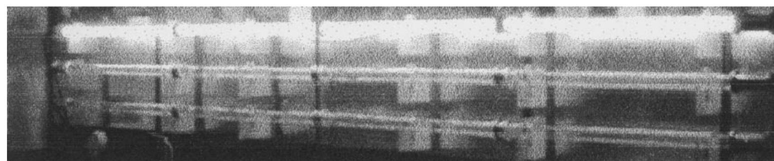

Fig. 1. A photograph of the excilamp emitter with one branch switched on.

1063-7850/02/2811-0899$22.00 © 2002 MAIK "Nauka/Interperiodica"

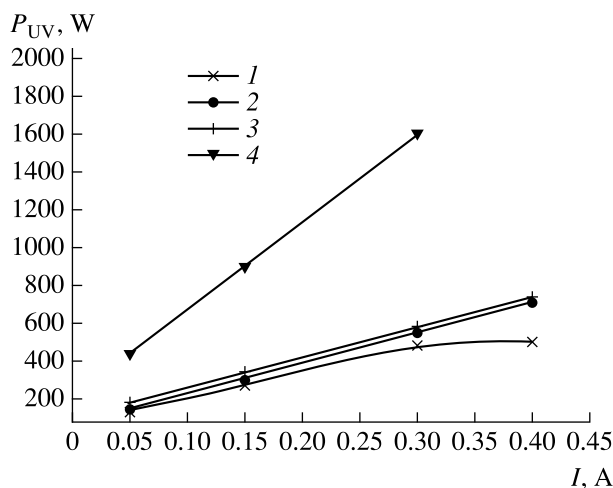

Fig. 2. Plots of the average output power P_{UV} (KrCl* emission) versus discharge current I for one branch of an excilamp employing quartz tubes with a diameter of (*1*) 52 mm and (*2*, *3*) 56 mm and (*4*) for the whole emitter. Working gas mixture: He–Kr–Cl_2 (2 : 5 : 1) at an initial pressure of 0.3 Torr.

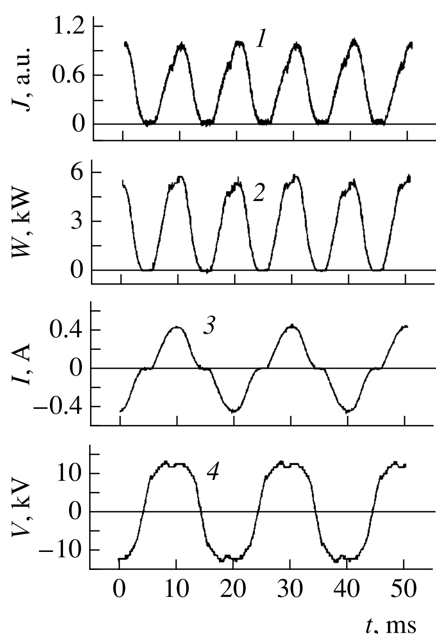

Fig. 3. Typical oscillograms of the pulses of (*1*) emission from KrCl* molecules, (*2*) pumping power (calculated), (*3*) discharge current, and (*4*) interelectrode voltage for one branch. Working gas mixture: Kr–Cl_2 (5 : 1) at an initial pressure of 0.3 Torr.

krypton or xenon with molecular chlorine and (in the experiments with additives) helium were prepared immediately inside the emitter tubes.

Results and discussion. We have separately tested each section and branch of the emitter and the whole excilamp. Figure 2 shows plots of the output power versus discharge current for each branch of a KrCl excilamp operating separately and for the whole emitter. It was found that higher radiation powers were provided by quartz tubes with an external diameter of 56 mm. Tested separately, one emitter branch of four sections gave an average output power about 0.7 kW at a wavelength of 222 nm with a pumping efficiency of ~12% (for 56-mm tubes). Three branches operating simultaneously produced an output power of 1.6 kW at an efficiency above 10%. It should be noted that operation of the high-power excilamp is accompanied by the formation of ozone and nitrogen oxides in large concentrations, which requires measures be taken to protect laboratory personnel.

When krypton was replaced by xenon, the breakdown voltage and resistance of the gas discharge plasma increased and, accordingly, the average pumping power decreased. This was related to a relatively low maximum voltage of the power supply units. For this reason, the maximum average power of the emission from XeCl* molecules was 1.1 kW, which is lower than the value for KrCl* molecules. The average output power of one emitter branch was 0.4 kW for the 56-mm quartz tubes and 0.3 kW for the 52-mm tubes.

For both binary and ternary gas mixtures, a maximum pumping efficiency was observed at small discharge currents and amounted to ~20% and ~15% for KrCl and XeCl excilamps, respectively. The working pressures of the gas mixture in the new excilamp were lower as compared to those used previously [3, 4], which is explained by a lower power supply voltage per unit length of the emitter. When the discharge current density was increased, the maximum average powers of emission for both exciplex molecules were observed in ternary mixtures with additives of a light inert gas. The above parameters are not limiting for this emitter and can be increased by using supply units of higher power and voltage, by increasing the working gas pressure, and by improving the cooling of quartz tubes and electrodes. It should be noted that the cathode and anode potential drop was observed only at the ends of branches (in the terminal emitter sections), while the central sections exhibited a positive glow discharge column.

Figure 3 shows typical oscillograms of the pulses of emission intensity, discharge current, interelectrode voltage, and a calculated curve of the pumping power for one branch of the excilamp. As was noted above, the lamp was excited by an ac voltage from a transformer connected to the commercial main line. As can be seen, the duration of emission pulses coincides with that of the current pulses and is independent of their polarity. The emission spectrum of the new emitter is typical of excilamps pumped by a glow discharge. The main emission power (>70%) is concentrated in the B–X band.

Conclusion. We created a high-power cylindrical excilamp pumped by a glow discharge and studied the characteristics of pumping and emission from KrCl*

and XeCl* molecules. For the first time, the average output power of emission from these molecules exceeded 1 kW in the UV spectral range. This excilamp can be used as a pumping source to obtain high-power spontaneous emission due to transitions in other atoms and molecules.

Acknowledgments. The authors are grateful to the Lawrence Livermore National Laboratory (contract no. B506095) and to the International Scientific-Technological Center (project no. 1270) for financial support of this study.

REFERENCES

1. A. N. Panchenko, É. A. Sosnin, V. S. Skakun, *et al.*, Pis'ma Zh. Tekh. Fiz. **21** (20), 47 (1995) [Tech. Phys. Lett. **21**, 851 (1995)].
2. M. I. Lomaev, A. N. Panchenko, V. S. Skakun, *et al.*, Laser Part. Beams **15** (2), 241 (1998).
3. M. I. Lomaev, A. N. Panchenko, É. A. Sosnin, and V. F. Tarasenko, Zh. Tekh. Fiz. **68** (2), 64 (1998) [Tech. Phys. **43**, 192 (1998)].
4. A. N. Panchenko, E. A. Sosnin, and V. F. Tarasenko, Opt. Commun. **166**, 249 (1999).
5. A. P. Golovitskiĭ, Pis'ma Zh. Tekh. Fiz. **18** (8), 73 (1992) [Sov. Tech. Phys. Lett. **18**, 269 (1992)].
6. A. P. Golovitskiĭ and V. S. Kan, Opt. Spektrosk. **75** (3), 604 (1993) [Opt. Spectrosc. **75**, 357 (1993)].
7. A. N. Panchenko, É. A. Sosnin, and V. F. Tarasenko, RF Patent No. 2089971 (1995), Byull., No. 25, 352 (1997).
8. A. N. Panchenko, É. A. Sosnin, and V. F. Tarasenko, RF Patent No. 2089962 (1995), Byull., No. 25, 350 (1997).

Translated by P. Pozdeev

Technical Physics Letters, Vol. 28, No. 11, 2002, pp. 902–903. Translated from Pis'ma v Zhurnal Tekhnicheskoĭ Fiziki, Vol. 28, No. 21, 2002, pp. 48–50.
Original Russian Text Copyright © 2002 by Shuman, Savkina.

Nondestructive Determination of the Characteristics of Porous Silicon Carbide Layers

V. B. Shuman and N. S. Savkina

Ioffe Physicotechnical Institute, Russian Academy of Sciences, St. Petersburg, 194021 Russia
e-mail: nata.sav@pop.ioffe.rssi.ru

Received June 14, 2002

Abstract—It shown that the porosity and thickness of a porous silicon carbide layer can be nondestructively monitored provided that the sample weight loss upon electrochemical etching is known and the reflectance spectrum exhibits interference. *© 2002 MAIK "Nauka/Interperiodica".*

The main parameters of a porous layer are its thickness and porosity. In studying porous silicon, the porous layer thickness h is readily determined by etching off the layer in a low-concentration KOH solution [1], after which the porosity P is calculated, using the data of gravimetric measurements, as

$$P = \frac{\Delta M}{Shd}, \tag{1}$$

where ΔM is the sample weight loss upon electrochemical etching, S is the area of the porous layer, and d is the density of silicon.

In the case of a porous silicon carbide (por-SiC), the porous layer cannot be removed as readily. For this reason, a sample has to be cleaved and the por-SiC layer thickness determined with the aid of electron microscopy. However, if the reflectance spectrum of a sample exhibits an interference pattern, the P and h values can be simultaneously determined using the following nondestructive method.

Let ν_1 and ν_2 be wavenumbers corresponding to adjacent maxima in the reflectance spectrum. The thickness of the porous layer producing this interference pattern is

$$h = \frac{1}{2n_{ef}}(\nu_1 - \nu_2)^{-1}, \tag{2}$$

where n_{ef} is effective refractive index of por-SiC, which depends on the degree of porosity and is different from the refractive index (n_0) of a SiC single crystal.

The unknown n_{ef} value can be calculated using the Bruggeman model of an effective medium. According to this model, the effective permittivity ε_{ef} of a medium composed of N components can be calculated provided that the volume fractions (f) and dielectric constants (ε) of each component are known [2]. Applying this model to a two-component medium (SiC and air in pores), we obtain the relations

$$f_1 + f_2 = 1, \tag{3}$$

$$f_1\frac{\varepsilon_1 - \varepsilon_{ef}}{\varepsilon_1 + 2\varepsilon_{ef}} + f_2\frac{\varepsilon_2 - \varepsilon_{ef}}{\varepsilon_2 + 2\varepsilon_{ef}} = 0. \tag{4}$$

In the case under consideration, the volume fraction of air ($\varepsilon_1 = 1$) in pores is $f_1 = P$, while the volume fraction of por-SiC is $f_2 = 1 - P$. Assuming that SiC (like Si [2]) has $\mathrm{Re}\lfloor(n_0 - i_k)^2\rfloor \cong n_0^2$, where k is the extinction coef-

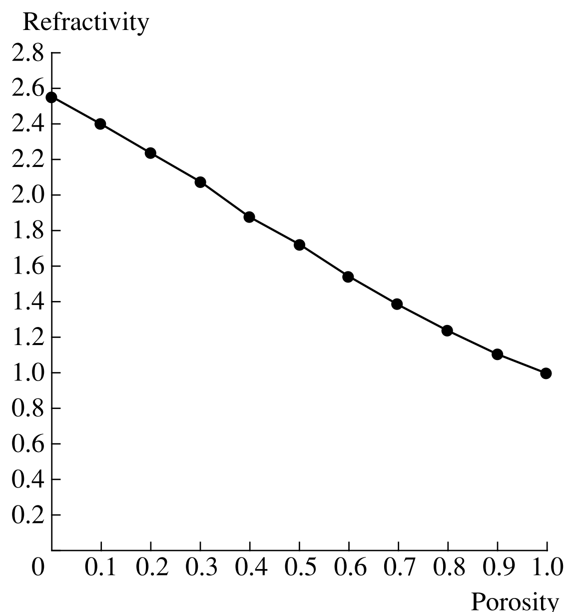

A plot of the refractive index versus porosity for porous silicon carbide.

1063-7850/02/2811-0902$22.00 © 2002 MAIK "Nauka/Interperiodica"

ficient, we obtain the following relation from Eq. (4):

$$\frac{P(1-n_{ef}^2)}{1+2n_{ef}^2} + \frac{(1-P)(n_0^2-n_{ef}^2)}{n_0^2+2n_{ef}^2} = 0. \quad (5)$$

Calculated by this formula, the plot of refractivity n_{ef} as a function of the porosity of silicon carbide is presented in the figure. Since the plot is linear at $P < 0.3$ and is close to linear at $P > 0.3$, we can adopt the following approximation:

$$n_{ef} \approx n_0 - (n_0 - 1)P. \quad (6)$$

By substituting expressions (1) and (6) into (2), we obtain a formula for the por-SiC layer thickness,

$$h = \frac{1}{n_0}\left[\frac{1}{2(\nu_1-\nu_2)} + (n_0-1)\frac{\Delta M}{Sd}\right]. \quad (7)$$

Once the layer thickness is determined, the porosity can be calculated using formula (1). Thus, the characteristics of a por-SiC layer are determined in a nondestructive manner from the sample weight loss upon etching and the interference pattern in the reflectance spectrum of the sample.

We obtained a good coincidence of the values of the por-SiC layer thickness determined with the aid of a scanning electron microscope and the results of calculation using formula (7) for samples exhibiting an interference pattern in the reflectance spectrum measured in the wavelength interval from 2.5 to 10 μm. The optical measurements were performed on an IKS-29 spectrophotometer. The proposed calculation algorithm is applicable to all semiconductors in which the porous layer can be modeled by a two-component medium.

Acknowledgments. This study was supported by the Russian Foundation for Basic Research, project no. 01-02-17907.

REFERENCES

1. C. Mazzoleni and L. Pavesi, Appl. Phys. Lett. **67** (20), 2983 (1995).
2. S. Zangooie, P. O. A. Persson, J. N. Hilfiken, *et al.*, J. Appl. Phys. **87** (12), 8497 (2000).

Translated by P. Pozdeev

Technical Physics Letters, Vol. 28, No. 11, 2002, pp. 904–906. Translated from Pis'ma v Zhurnal Tekhnicheskoĭ Fiziki, Vol. 28, No. 21, 2002, pp. 51–56.
Original Russian Text Copyright © 2002 by Dugaev, Volkov, Oszwaldowski, Vieira.

Energy Relaxation during Inelastic Electron Scattering on Localized States

V. K. Dugaev[a,b], V. L. Volkov[b], M. Oszwaldowski[c], and M. Vieira[a]

[a] *Institute Superior de Engenharia de Lisboa, Portugal*

[b] *Chernovtsy Branch, Institute for Problems in Materials Science, National Academy of Sciences of Ukraine, Chernovtsy, Ukraine*

e-mail: chimsp@unicom.cv.ua

[c] *Technical University, Poznan, Poland*

Received March 22, 2002

Abstract—A mechanism which can be responsible for the phase relaxation in polycrystalline semiconductors and metals is proposed. This mechanism is related to the inelastic scattering of electrons on localized states with energies near the Fermi level. © *2002 MAIK "Nauka/Interperiodica".*

In recent years, there have appeared a large number of papers devoted to the possible mechanisms of phase relaxation in disordered semiconductors and metals [1–4]. At present, it is commonly accepted [3, 5, 6] that the inelastic scattering of electrons on two-level centers can account for saturation of the phase relaxation time at $T \longrightarrow 0$. The results of experiments with polycrystalline disordered metals have clearly demonstrated that the phase relaxation time at low temperatures exhibits saturation [4]. An analogous behavior was recently observed in experiments with thin polycrystalline films of indium antimonide strongly doped with lead [7, 8], where the concept of inelastic scattering of electrons in the vicinity of grain boundaries as the possible reason for the observed relaxation time saturation was formulated.

In this Letter, we present an estimate of the time of energy relaxation during the inelastic interaction of a free electron with electrons localized at impurity centers or defects. The main assumption is that a sufficiently dense energy spectrum of localized electron states exists in the vicinity of the Fermi energy of free electrons.

Let us consider a polycrystalline, strongly doped semiconductor with charge carriers (for certainty, electrons) that exhibit diffusion motion within grains (the free path length l being much shorter than the characteristic grain size L_c). The electron gas is assumed to be degenerate, and the mobility threshold for the electrons in a grain is assumed to occur below the Fermi level. In this case, the electron conductivity in the grains can be described by a classical theory with small corrections for the localization ($k_F l \gg 1$). We will also assume that the grains are separated by thin tunneling-transparent barriers (which allow the electrons to move readily in the polycrystalline material) and that the intergranular space is filled with an amorphized semiconductor. Thus, within a simplified model adopted, the material filling the space between grains represents a strongly doped semiconductor with a mobility threshold lying significantly above the Fermi level. The main assumption is that the electron states with energies near the Fermi level are localized in space between and/or at the surface of grains.

In accordance with this concept, we consider a model with the energy spectrum ε_k of electrons filling the Fermi sphere and a large number of localized electron states with the energies ε_n near the Fermi level. Since the energy levels of the localized states are situated within the energy band $\varepsilon_{\mathbf{k}}$, these are the resonance states hybridized with the $\varepsilon_{\mathbf{k}}$ spectrum. For the purpose of estimation, we will neglect the hybridization effects and consider the states with the energies ε_n as localized states.

We believe that the above model can be in fact realized in the vicinity of a crystal grain boundary. Discreteness of the spectrum is related to the surface states appearing due to boundary defects or broken bonds. As is known, a semiconductor material filling the space between grains possesses the properties of an amorphous semiconductor [9] with a rather wide band of discrete levels. In the model proposed, we assume that such localized states exist near the Fermi energy of nonlocalized electrons.

The energy relaxation time for an electron with the energy $\varepsilon_{\mathbf{k}}$ can be calculated using the following formula of the perturbation theory:

$$\frac{1}{\tau(\varepsilon_{\mathbf{k}})} = \frac{2\pi}{\hbar}\Omega\int\frac{d^3\mathbf{k}}{(2\pi)^3}\sum_{i,n,n'}|V_{\mathbf{kk}',nn'}|^2[1-f(\varepsilon_{\mathbf{k}'})] \times f(\varepsilon_n)[1-f(\varepsilon_{n'})]\delta(\varepsilon_{\mathbf{k}}-\varepsilon_{\mathbf{k}'}+\varepsilon_n-\varepsilon_{n'}), \quad (1)$$

where $V_{\mathbf{kk}',nn'}$ is the matrix element of the electron–electron interaction, whereby one electron passes from state

k to **k**' and the other, from state n to n'. The sum over i is taken over all localized centers, while n and n' imply the states of the same center. The Fermi distribution function $f(\varepsilon)$ in Eq. (1) restricts the integration and summation operations to the transitions from occupied to vacant states; the δ function is related to the law of energy conservation; and Ω denotes the crystalline grain volume (a separate grain is considered a crystal of volume Ω). The applicability of formula (1) to the localized or resonance states is limited by the use of the second-order perturbation theory with respect to the electron–electron interaction. The model under consideration is restricted to this approximation.

Using the free-electron wave functions normalized in the volume Ω and a set of the wave functions corresponding to electrons localized at the ith impurity, we can determine the elements of the scattering matrix $V_{\mathbf{kk}', nn'}$. The process of scattering of a free electron on the scalar potential $H_{int}(\mathbf{r}) = e\phi(\mathbf{r})$ can be described as the interaction for a Hamiltonian in the secondary quantization representation:

$$\int d^3\mathbf{r}\psi^*(\mathbf{r})H_{int}(\mathbf{r})\psi(\mathbf{r}) = \frac{e}{\Omega}\sum_{kq}\int\frac{d^3\mathbf{k}}{(2\pi)^3}\frac{d^3\mathbf{q}}{(2\pi)^3}c^+_{\mathbf{k}}c_{\mathbf{k}-\mathbf{q}}\phi_{\mathbf{q}}, \quad (2)$$

where $\psi^*(\mathbf{r})$, $\psi(\mathbf{r})$ and $c^+_{\mathbf{k}}$, $c_{\mathbf{k}}$ are the operators of production and annihilation of delocalized electrons in the coordinate and momentum spaces, respectively, and $\phi_{\mathbf{q}}$ is the Fourier transform of $\phi(\mathbf{r})$.

Transitions between the localized states n and n' are described by the expression

$$\int d^3\mathbf{r}\psi^*_l(\mathbf{r})e\phi(\mathbf{r})\psi_l(\mathbf{r}) = e\sum_{nn'}\int\frac{d^3\mathbf{q}}{(2\pi)^3}w_{nn'}(\mathbf{q})c^+_n c_{n'}\phi_{\mathbf{q}}, \quad (3)$$

with the matrix

$$w_{nn'}(\mathbf{q}) = \int d^3r\varphi^*_n(\mathbf{r})\varphi_{n'}(\mathbf{r})e^{i\mathbf{q}\cdot\mathbf{r}}, \quad (4)$$

where $\varphi_n(\mathbf{r})$ is the wave function of the localized electron. In these terms, the amplitude of a process involving the transitions $\mathbf{k}, n \longrightarrow \mathbf{k}', \mathbf{n}'$ can be expressed as

$$V_{nn', k'}(\mathbf{q}) = \frac{e^2}{\Omega}w_{nn'}(-\mathbf{q})D(\mathbf{q}), \quad (5)$$

where $D(\mathbf{q}) \equiv \langle\phi_{\mathbf{q}}\phi_{-\mathbf{q}}\rangle = 4\pi/q^2$ is the correlator of electromagnetic fluctuations [10].

Now, let us calculate the probability (4). Let a_l be the radius of the corresponding localized function. Since the energy transfer to an electron at the Fermi surface is on the order of k_BT, the corresponding momentum transfer is $q \propto k_F(k_B/T)/\varepsilon_F$, where ε_F is the Fermi energy of localized electrons and k_B is the Boltzmann constant. From this we obtain the estimate $qa_l \propto a_lk_F(k_BT)/\varepsilon_F \ll 1$. Thus, the exponent in Eq. (4) can be expanded into a series in $(\mathbf{q}\cdot\mathbf{r})$, which yields

$$w_{nn'}(\mathbf{q}) \approx (qa_l)^2. \quad (6)$$

This relation was obtained taking into account that the first term in the expansion of the exponent can be omitted due to orthogonality of the wave functions with different n, while the second term becomes zero after integration with respect to the angles in (1). Using relations (5) and (6) and introducing the densities of states ρ and ρ_l for the free and localized electrons, respectively, which are constant in the vicinity of the Fermi level, we obtain the following estimate for the relaxation time:

$$\frac{\hbar}{\tau(\varepsilon)} \propto \varepsilon^2\rho\rho_l^2 Ry^2 a_B^2 a_l^4, \quad (7)$$

where $Ry = me^4/\varepsilon_0\hbar^2$ and $a_B = \varepsilon_0\hbar^2/me^2$ are the Rydberg and Bohr radii, respectively. This result corresponds to the usual electron–electron scattering in metals [11], for which the relaxation time is proportional to the square of energy ε^2.

For the density of states at the Fermi energy, we obtain the estimate $\rho = mk_F/2\pi^2\hbar^3 \propto k_F/(a_B^2 Ry)$. Now, we can also evaluate the density of the localized level (related to a single defect center) as $\rho_l \approx 1/\Delta\varepsilon$, where $\Delta\varepsilon \approx \hbar^2/m_0a_l^2$ is the average energy difference between the closest localized states. Note that the density of the localized level was evaluated using the effective electron mass m_l, which differs from the free electron mass in InSb because most of the local states are situated in the regions between grains which are occupied by an amorphous material with significantly different properties. The number of local centers is determined as $N_l \approx c_lL_dL_c^2$, where c_l is the density of defects in the space between grains, L_d is the width of this region, and L_c is the grain size ($L_c^3 = \Omega$).

For the numerical estimates, we will employ the following parameters of InSb: $m = 0.014m_0$ and $\varepsilon_0 = 16$, which yields $a_B = 6.75 \times 10^{-6}$ cm and $Ry = 0.003$ eV. For the free carrier concentration $n = 5 \times 10^{16}$ cm^{-3}, this yields $k_F \approx 10^6$ cm^{-1}. The energy measured from the Fermi level is $\varepsilon \approx k_BT$. Our estimates for the other parameters are as follows: $L_c = 10^{-5}$ cm, $L_d = 10^{-6}$ cm, $a_l = 10^{-6}$ cm, $c_l = 10^{22}$ cm^{-3}, and $m_l = 0.2m_0$. For these values, we obtain

$$\frac{\hbar}{\tau_\varepsilon} \approx T \times 10^3\frac{T}{Ry}. \quad (8)$$

This indicates that the energy relaxation time at $T > 1$ K exhibits a stronger temperature dependence than $\varepsilon \approx k_BT$. In other words, electrons inelastically scattered

from the local defect centers on the grain boundaries loose their coherency.

The observed phase relaxation (in the estimates, we assume that the phase relaxation time is on the same order of magnitude as the energy relaxation time) in a polycrystalline material with strong electron relaxation on the grain boundaries is on the order of the time of diffusion through the grain $\tau_c \approx L_c^2/D_0$, where D_0 is the diffusion coefficient of delocalized electrons. The reason for this is that electrons diffusing through a grain do not "feel" the grain boundaries. As a result, the observed phase relaxation time is independent of the temperature over a broad temperature interval. Only when the temperature decreases below a certain critical level determined by the condition of compete dephasing at the boundary, $h/\tau_\varepsilon \approx k_B T$, does the relaxation time begin to increase.

Thus, our estimates show that the electron scattering from local states at the grain boundaries can be a reason for the dephasing of electrons during their motion through the boundaries. In this case, the observed phase relaxation time in a polycrystalline material is determined by the average grain size. According to a concept proposed previously [7, 8], this can explain the effect of saturation of the phase relaxation time in polycrystalline InSb films at $1\ K < T < 4\ K$. It should be emphasized that the above calculations were performed within the framework of a simplified model and, hence, possess the character of estimates.

Acknowledgments. This study was supported by grants from P.P. (BW62-184), the INTAS foundation (2000-0476), and NATO (CP (UN) 06/B/2001/PO).

REFERENCES

1. P. Mohanty, E. M. Q. Jariwala, and R. A. Webb, Phys. Rev. Lett. **78** (17), 3366 (1997).
2. B. L. Altshuler, M. E. Gershenzon, and I. L. Aleiner, Physica E (Amsterdam) **3** (1–3), 58 (1998).
3. Y. Imry, H. Fukuyama, and P. Schwab, Europhys. Lett. **47** (5), 608 (1999).
4. J. J. Lin and L. Y. Kao, J. Phys.: Condens. Matter **13** (5), L119 (2001).
5. A. Zawadowski, J. von Delft, and D. C. Ralph, Phys. Rev. Lett. **83** (13), 2632 (1999).
6. I. L. Aleiner, B. L. Altshuler, and Y. M. Galperin, Phys. Rev. B **63** (20), 201401 (2001).
7. M. Oszwaldowski, T. Berus, and V. K. Dugaev, Mol. Phys. Rep. **21** (1), 139 (1998).
8. M. Oszwaldowski, T. Berus, and V. K. Dugaev, Ann. Phys. (Leipzig) **8** (S1), 201 (1999).
9. D. Adler, in *Physical Properties of Amorphous Materials*, Ed. by D. Adler, B. B. Schwartz, and M. C. Steele (Plenum, New York, 1985).
10. V. B. Berestetskii, E. M. Lifshitz, and L. P. Pitaevskii, *Course of Theoretical Physics*, Vol. 4: *Quantum Electrodynamics* (Nauka, Moscow, 1989; Pergamon, New York, 1982).
11. D. J. Thouless, Phys. Rev. Lett. **39** (18), 1167 (1977).

Translated by P. Pozdeev

Technical Physics Letters, Vol. 28, No. 11, 2002, pp. 907–909. Translated from Pis'ma v Zhurnal Tekhnicheskoĭ Fiziki, Vol. 28, No. 21, 2002, pp. 57–61.
Original Russian Text Copyright © 2002 by Musaev.

Microchannel Avalanche Photodetector Based on a Si–SiO_2 Structure

M. A. Musaev

Azerbaijan State Petroleum Academy, Baku, Azerbaijan

e-mail: ihm@adna.baku.az

Received May 23, 2002

Abstract—A new avalanche photodetector is developed and realized on the basis of a Si–SiO_2 microchannel structure. The new device is analogous to the well-known vacuum microchannel plates but possesses better technological characteristics. A considerable increase in the photocurrent amplification coefficient is achieved due to decreased fluctuations of the semiconductor breakdown voltage and suppressed local avalanche processes in inhomogeneities of the semiconductor responsible for the microplasma breakdown. *© 2002 MAIK "Nauka/Interperiodica".*

In recent years, there has been a considerable interest in the development of avalanche photodetectors of a new type based on silicon heterostructures. These devices possess higher sensitivity at a potentially lower cost of production as compared to the analogous characteristics of traditional avalanche photodiodes [1, 2]. The most significant results were obtained with avalanche structures of the Si–SiO_2 and Si–SiC types with a local suppression of the avalanche process [3–5]. The former structure exhibits better parameters only when the power is supplied in a pulsed regime, while the latter can operate with both pulsed and dc power supplies owing to the presence of a SiC layer of the required conductivity type.

As is known [5], avalanche photodetectors possessing high parameters can be obtained by, first, completely blocking the charge carrier injection from a metal electrode and, second, ensuring spatial localization of the avalanche process. In this work, a new design of the silicon avalanche structure is suggested and implemented that obeys both these conditions.

The proposed photodetector was implemented on the basis of a *p*-Si substrate with a resistivity of ~1 Ω m, on which a ~500-Å-thick oxide (SiO_2) layer was grown by thermal oxidation and a system of 2×2 μm windows exposing the substrate was formed with a spacing of 5 μm. Material in the windows was ion-doped with phosphorus to a dose of ~5×10^{-4} C/cm^2 so as to obtain a matrix of *p–n* junctions with a thickness of ~1 μm. The surface of the *p–n* junctions was coated with a ~25-Å-thick (tunneling-transparent) oxide film. Applied onto the oxide surface was a semitransparent titanium field electrode with an area of ~1 mm^2. In order to elucidate special features of the proposed structure, usual avalanche photodiodes were also fabricated on the basis of a common plane-parallel *p–n* junction.

Due to a sufficiently high conductivity of the tunneling-transparent oxide layer, the photodetector can operate with a dc power supply. For this purpose, a positive (relative to the substrate) potential, the magnitude of which is sufficient to initiate the avalanche process in the *p–n* junctions, is applied to a semitransparent electrode. The applied potential is divided between the oxide layer and the silicon substrate. Owing to a small thickness and a rather high conductivity of the tunneling-transparent oxide as compared to those of a thick thermal oxide, a maximum field strength sufficient for the avalanche process development is always achieved in the regions of the *p–n* junctions in the matrix. This provides for a complete localization of the avalanche process, whereby the charge carriers generated by the impact-field ionization are accumulated at the boundary between silicon and the tunneling-transparent oxide and decrease (shield) the electric field in this region of the semiconductor. When the field strength decreases below a certain critical value, the avalanche process in a given microchannel (*p–n* junction) ceases. The pulsed photoresponse represents a bias current passing through a capacitance of the dielectric layer of the structure.

The main feature of the structure with a matrix of *p–n* junctions is that the photocurrent amplification coefficient is much higher as compared to that in a conventional (base) structure. Figure 1 shows plots of the photocurrent amplification coefficient versus applied voltage for the two structures measured using light pulses with a duration of ~100 ns and a pulsed radiation power of ~4.4×10^{-9} W.

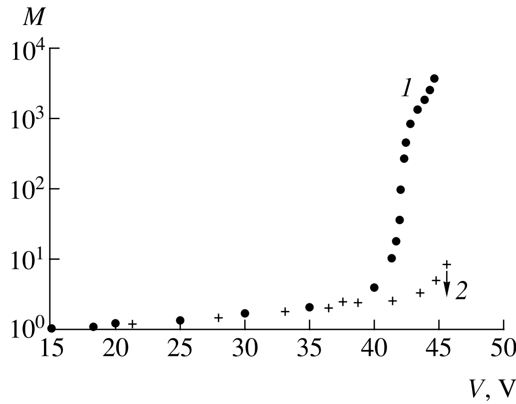

Fig. 1. Plots of the pulsed photocurrent amplification coefficient versus applied voltage for (*1*) the new microchannel structure and (*2*) a base structure.

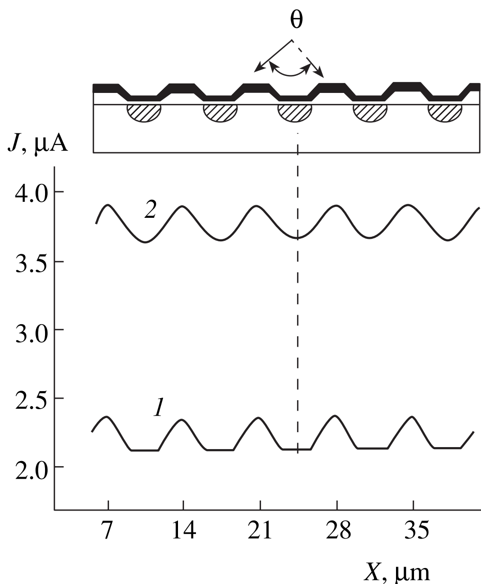

Fig. 2. Oscillograms illustrating spatial variation of the photocurrent across a microchannel avalanche photodetector structure with M = 5000 measured at an electron beam energy of E = 15 (*1*) and 30 keV (*2*).

In the working regime, a voltage V was applied to the sample structure with a polarity corresponding to depletion of the semiconductor–dielectric interface. The light source was a light-emitting diode with $\lambda \sim$ 650 nm. The amplification coefficient of the avalanche photodetector was determined as a ratio of the amplitude of the amplified photocurrent for $V > 15$ V to that for $V = 15$ V. As can be seen from Fig. 1, the photocurrent amplification coefficient of the structure with the *p–n* matrix (curve *1*) at a voltage of $V = 44$ V exceeds the analogous coefficient of the base structure with a single plane-parallel *p–n* junction by a factor above 1000. In the base structure, high amplification coefficients cannot be achieved because the avalanche current exhibits unlimited growth on microinhomogeneities of the silicon substrate, which essentially shunt the entire working area of the device.

The proposed structure is characterized by a decrease in breakdown voltage, which is due to the "point" effect at the sharp *p–n* junctions of the microchannel structure. After thermal diffusion of the doping impurity through windows with a diameter on the order of ~2 μm, the *p–n* junctions formed in the surface layer of the substrate are characterized by nearly hemispherical boundaries. For a depth of the impurity diffusion comparable to a maximum possible thickness W of a depletion layer in the substrate (in this case, $W \sim$ 1.8 μm), the equipotential surfaces of the electric field around the *p–n* junctions are characterized by a large curvature. As a result, the avalanche process begins at a much lower potential as compared to that in a base structure with a plane-parallel junction.

It was established that a significant increase in the photocurrent amplification coefficient in the structures with *n*-type conductivity is achieved due to (i) a decrease in fluctuations of the semiconductor breakdown voltage after the formation of sharp hemispherical *p–n* junctions [5] and (ii) a local (within a single micro-*p–n* junction) suppression of the avalanche process in inhomogeneities of the semiconductor responsible for the microplasma breakdown. The point is that electrons passing from one *n*-type region to another have to overcome a potential barrier with a height of ~5 eV (formed due to different thicknesses of the two silicon oxide layers).

A spatial inhomogeneity of the avalanche process in the proposed microchannel structure was studied by scanning a sample with the beam of an electron microscope. The photocurrent inducing the avalanche process in the semiconductor was generated by the electron beam scanning over the working area of the photodetector structure. The electron beam diameter did not exceed 0.5 μm. The photoresponse was measured as an oscillogram corresponding to a single passage along the surface structure (Fig. 2). It was found that the periodic pattern on the oscillogram repeats the arrangement of small *p–n* junctions, with a minimum signal observed when the electron beam probes the middle of each hemispherical *n*-region. This is explained by the fact that the electron beam loses a part of its energy in the highly doped *n*-regions. Despite this microscopic structure, the microchannel avalanche photodetector is characterized by a sufficiently homogeneous photoresponse over the working area. For example, at an electron beam energy of E = 30 keV, the relative variation of the photocurrent over the detector surface does not exceed 5% (Fig. 2, curve *2*).

Thus, a new avalanche photodetector has been developed and realized on the basis of a $Si–SiO_2$ microchannel structure, which is analogous to the well-known vacuum microchannel plates but possesses bet-

ter technological characteristics. The new device can be successfully employed for the detection of very weak light fluxes of light and gamma-quanta.

Acknowledgments. The author is grateful to Z.Ya. Sadygov for his help in manufacturing the samples.

REFERENCES

1. A. Ya. Vul', A. T. Dideĭkin, and A. I. Kosarev, Pis'ma Zh. Tekh. Fiz. **16** (21), 15 (1990) [Sov. Tech. Phys. Lett. **16**, 813 (1990)].
2. Z. Ya. Sadygov, M. K. Suleĭmanov, and T. Yu. Bokova, Pis'ma Zh. Tekh. Fiz. **26** (7), 75 (2000) [Tech. Phys. Lett. **26**, 305 (2000)].
3. A. B. Kravchenko, A. F. Plotnikov, Yu. M. Popov, and V. É. Shubin, Kvantovaya Élektron. (Moscow) **8** (1), 785 (1981).
4. V. V. Osipov, A. A. Pankratov, and V. A. Kholodnov, Zh. Tekh. Fiz. **60** (6), 121 (1990) [Sov. Phys. Tech. Phys. **35**, 707 (1990)].
5. Z. Ya. Sadygov, Doctoral Dissertation in Physics and Mathematics (Mosk. Inzh.-Fiz. Inst., Moscow, 1997).

Translated by P. Pozdeev

Technical Physics Letters, Vol. 28, No. 11, 2002, pp. 910–912. Translated from Pis'ma v Zhurnal Tekhnicheskoĭ Fiziki, Vol. 28, No. 21, 2002, pp. 62–67.
Original Russian Text Copyright © 2002 by Astrov, Purwins.

Spatiotemporal Structures in a Transversely Extended Semiconductor System

Yu. A. Astrov[a],* **and H.-G. Purwins**[b],**

[a] *Ioffe Physicotechnical Institute, Russian Academy of Sciences, St. Petersburg, 194021 Russia*
** e-mail: yuri.astrov@pop.ioffe.rssi.ru*
[b] *Institute of Applied Physics, Münster University, 48149 Münster, Germany*
*** e-mail: purwins@uni-muenster.de*

Received June 4, 2002

Abstract—A semiconductor system with an N-shaped current–voltage characteristic can generate nonstationary structures that are inhomogeneous in the direction transverse to the current flow. In samples of semiinsulating GaAs with a large cross section, this effect is explained by a loss of stability of the regime of uniform domain motion. *© 2002 MAIK "Nauka/Interperiodica".*

The interest in investigations of the self-organization of spatial structures in distributed nonequilibrium systems is explained, in particular, by the prospects of creating computing devices based on new principles [1]. Distributed semiconducting media frequently exhibit the formation of dissipative structures, a classical example being offered by the spontaneous formation of field domains in systems with N-shaped current–voltage (I–U) characteristics [2]. To our knowledge, previous investigations of the electrical domain instabilities in semiconductors were restricted to narrow (quasi-one-dimensional) systems, in which domain structures in the direction transverse to the current flow were ignored (see, e.g., recent review [3] devoted to the problem of domain instability in semiinsulating GaAs).

Recently [4], we observed complicated behavior of a planar system of the "semiconductor–gas-discharge (GD) gap" with a semiinsulating GaAs (si-GaAs) electrode. That study was devoted to the dynamics of spatiotemporal structures formed by an ensemble of pulsating current columns. The parameters of the GD region studied did not allow us to judge the role of the semiconductor in the appearance of the observed patterns.

In this paper, we will compare transport properties of structures of the two types, one of which contains a GD [5]. Both structures sequentially operate with the same si-GaAs sample. Using the data obtained under these conditions, it is possible to conclude that the spatially inhomogeneous current distributions readily observed in the structures with GDs are generated by the semiconductor element and, hence, can exist in the absence of GD as well. The experiments were performed with 1.5-mm-thick si-GaAs plates.[1]

[1] The si-GaAs plates were obtained from the Freiberger Company (Germany).

One experimental system (structure of type I) was completely solid-state, representing a si-GaAs plate with a strongly doped p^+ region with a thickness of about 10 μm (which was formed by zinc diffusion and served as a contact) on one side and a thin gold film (which was formed by vacuum deposition and served as the other contact) on the opposite side.

In another system (structure of type II), the role of the second contact (instead of the metal film) was played by a gas-filled gap in which a GD was initiated at a sufficiently high potential difference between electrodes. The discharge region with a thickness of 100 μm was filled with argon at a pressure of 200 GPa. This corresponds to a discharge operating in the Townsend regime (this stable form of discharge is employed in spectral image converters of the semiconductor–GD type [6] with photosensitive semiconductor electrodes possessing linear I–U characteristics).

The current in the experimental structures was controlled by illuminating the semiconductor via the p^+ electrode with the light of an incandescent lamp. The area of the conducting channel in both structures was 18 mm^2. In the structures of type II, the emission from gas molecules in the GD rendered the current distribution visible. These patterns were recorded with a digital video camera, transmitted into a computer, and processed.

Figure 1 shows examples of the stationary I–U curves measured (a) in the absence and (b) in the presence of a GD region. The curves in pairs *1*, *1*' and *2*, *2*' were obtained using the same intensity of light from the incandescent lamp illuminating the samples via the transparent p^+ electrode. As can be seen, the curves measured for one polarity of the applied voltage possess a clearly pronounced N-like shape. A comparison of data for the structures of two types shows that the

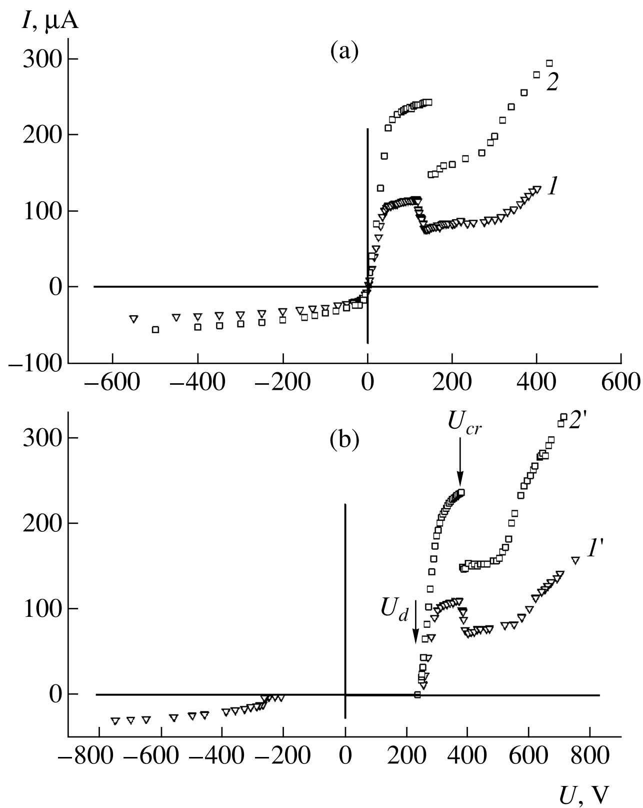

Fig. 1. Current–voltage characteristics measured on the samples (a) without and (b) with a gas-filled gap. The curves in pairs *1*, *1*' and *2*, *2*' were obtained using the same intensities of illumination of the semiconductor. Positive voltage corresponds to negative potential on the p^+ electrode.

presence of the GD region does not significantly modify the character of the charge transport in the system studied: the corresponding *I–V* curves are only shifted by a value corresponding to the potential U_d of the GD initiation. A change in the illumination intensity does not lead to a significant shift of the critical voltage U_{cr} at which the current *I* begins to drop with increasing voltage *U*. When the p^+ electrode was illuminated in the IR range (by light passed through a silicon filter), the N-like character of the *I–U* curve was not pronounced.

When the voltage *U* approaches the threshold level U_{cr} from below, the current *I* in the structures exhibits oscillations of a relatively small amplitude. Such a behavior of si-GaAs samples has been observed previously (see review [3]). For $U \geq U_{cr}$, the current usually oscillates in a broad range of voltages, whereby both regular and irregular variations can be observed. As is known, current pulsations of large amplitude in such materials are related to the dynamics of electrical domains (generation, motion along the sample, and damping at the contacts). It is suggested that electrical instability observed in the samples of this type is related to an increase in the rate of trapping carriers by EL2 centers heated by the electric field [3].

By using the structure with a GD electrode, we determined spatial distributions of the current corresponding to various parts of the *I–U* curve. The main characteristic features of these distributions are as follows:

(i) Immediately after a drop to smaller values, the current is stationary and its spatial distribution is homogeneous.

(ii) A subsequent increase in the supply voltage leads to the appearance of regions in the current-carrying channel in which the current is unstable: a current density pulse arising in the channel gives rise to a wave spreading over the space. The process can be coherent, exhibiting a cyclic character on space and time. Some phases of such process are illustrated by the series of images *1–8* in Fig. 2a. It should be noted that this coherence takes place in the presence of an inhomogeneity in the system (e.g., an artificial inhomogeneity created by nonuniform illumination of the semiconductor). In a homogeneous system, no special center determining the dynamics is found and the primary local current pulses arise at random points within the active region of the system. This results in a disordered spatiotemporal state of the system; an example of such a state is presented in Fig. 2b. As the voltage grows further, the sys-

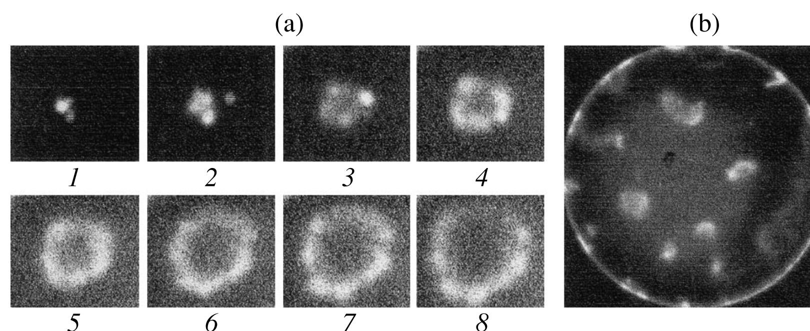

Fig. 2. Examples of spatial structures in the distribution of emission from the GD region. Light areas correspond to higher current densities: (a) images *1–8* represent a series of states in which a current pulse appears only at one point of the active region (interval between shots, 40 ms; horizontal size of the imaged region, 5 mm); (b) an example of the state with numerous sources of local current pulses (active region diameter, 18 mm).

tem shows various structures, description of which falls outside the scope of this short communication.

The similarity of the transport properties of both systems (Fig. 1) gives us ground to suggest that the spatiotemporal characteristics of current distributions in the unstable regions are similar as well. Therefore, by studying the patterns observed in the system with GD, we can judge the spatial structure of the current in a structure without a gas-filled gap. As is known, the nature of instability of the stationary current in si-GaAs with an N-like negative differential resistance (NDR) characteristic is related to the formation and motion of electrical domains. The above results lead to a conclusion that the state with a flat front of the electric domain in transversely extended si-GaAs samples may become unstable with respect to the transverse structure formation. This instability may give rise to a complicated pattern of charge transfer in the semiconductor, thus revealing a new property of systems with the N-like NDR characteristic. The spatiotemporal dynamics of the current distribution illustrated by images *1–8* in Fig. 2a resembles structures of the "guiding center" type extensively studied in the case of chemical reactors featuring oscillatory reaction regimes [7]. It should also be noted that the dynamic spatially inhomogeneous structures in the current distributions may negatively affect the characteristics of instruments based on si-GaAs [8].

Acknowledgments. The authors are grateful to E. Gurevich for his help in performing the experiments and to V. Abrosimova for conducting the zinc diffusion process.

This study was partly supported by the Russian Foundation for Basic Research (project no. 00-15-96750) and by a grant from Deutsche Forschungsgemeinschaft (DFG).

REFERENCES

1. A. Adamatzky, *Computing in Nonlinear Media and Automata* (Inst. of Physics Publ., Bristol, 2001).
2. V. L. Bonch-Bruevich, I. P. Zvyagin, and A. G. Mironov, *Electrical Domain Instabilities in Semiconductors* (Nauka, Moscow, 1972; Consultants Bureau, New York, 1975).
3. A. Neumann, J. Appl. Phys. **90** (1), 1 (2001).
4. C. Strümpel, Yu. A. Astrov, and H.-G. Purwins, Phys. Rev. E **65**, 066210 (2002).
5. Yu. A. Astrov, Fiz. Tekh. Poluprovodn. (St. Petersburg) **27** (11/12), 1971 (1993) [Semiconductors **27**, 1084 (1993)].
6. V. M. Marchenko, S. Matern, L. M. Portsel, *et al.*, Proc. SPIE **4669**, 1 (2002).
7. *Oscillations and Traveling Waves in Chemical Systems*, Ed. by R. J. Field and M. Burger (Wiley, New York, 1985).
8. J. V. Vaitkus, R. Irsigler, J. Andersen, *et al.*, Nucl. Instrum. Methods Phys. Res. A **460**, 204 (2001).

Translated by P. Pozdeev

Technical Physics Letters, Vol. 28, No. 11, 2002, pp. 913–915. Translated from Pis'ma v Zhurnal Tekhnicheskoĭ Fiziki, Vol. 28, No. 21, 2002, pp. 68–74.
Original Russian Text Copyright © 2002 by Zavilopulo, Snegursky.

Threshold Electron Impact Ionization of Molecules

A. N. Zavilopulo and A. V. Snegursky
Institute of Electron Physics, National Academy of Sciences of Ukraine, Uzhgorod, Ukraine
e-mail: an@zvl.iep.uzhgorod.ua
Received May 27, 2002

Abstract—Methods and results of an experimental investigation of the products of single ionization of molecules by electron impact in a near-threshold energy region are presented. The experiments were performed in a crossed beam geometry with ion separation and detection by a quadrupole mass spectrometer. Special attention is devoted to processing of the experimental data using a nonlinear weighing procedure for fitting by least squares based on the Marcwardt–Levenberg algorithm. *© 2002 MAIK "Nauka/Interperiodica".*

Previously, we reported the results of measurements of the threshold energies for the appearance of ionized products of the single and dissociative ionization of some complex organic [1, 2] and halogen-containing [3] molecules. The potentials of the appearance of fragment ions in such reactions were determined using a complicated procedure involving double differentiation of the initial portions of the ionization functions based on the method of Lossing (see [2]) with digital filtration and fitting by the Breit–Wigner formula.

However, subsequently [4], we established that, when this algorithm is employed and molecular nitrogen is used for the calibration, the presence of closely lying states of the N_2^+ ion near the threshold of rectification of the ionization function may lead to an additional error in determination of the true threshold energy for the appearance of fragment ions. In order to decrease the uncertainty of the energy scale and increase the accuracy of determination of the thresholds of appearance of the fragment ions, we have applied a special procedure based on a modified least-squares method. This procedure is described below.

The investigation was performed using a conventional scheme of crossed beams in a setup equipped with an MX-7303 quadrupole mass spectrometer. The experimental setup was described in detail previously [1]. Below, we will concentrate on the principal methodological aspects of the problem studied. The molecular beams were generated by a multichannel source of the effusion type, which allowed the density of ions in the region of interaction with the electron beam to be maintained at a level of 10^{10} cm^{-3}. The monoenergetic electron beam was generated by an electron gun. In the stabilized electron current regime, the gun produced a beam with energy variable from the process threshold to 20–30 eV at a beam current of 0.01–0.5 mA and an electron energy scatter not exceeding ΔE = 500 meV. The electron beam energy was automatically scanned by using a stepped voltage generator. Ions appearing in the region of collisions between electrons and atoms were analyzed on a real time scale using a quadrupole mass spectrometer and detected with a channel electron multiplier of the VEU-6 type.

In this series of experiments, we measured the functions of single and dissociative electron impact ionization of a series of molecules. Special emphasis was placed on a thorough analysis of the thresholds of appearance of both the main molecular ions and their fragments (daughter ions). The two main factors determining the behavior of the ionization cross section near the threshold are (i) the energy (velocity) of interacting particles and (ii) the energy distribution of ionizing electrons in the beam.

Uncertainty in the ionization cross section near the threshold is described by the Gauss function

$$S(E) = k\int_0^{\infty}\sigma(E-E_e)f(E_e)dE_e, \qquad (1)$$

where k is the detection constant, E is the energy determined by the accelerating electrode, E_e is the ionizing electron beam energy, σ is the ionization cross section, and $f(E_e)$ is the electron energy distribution function. An analysis of this relation shows that, for electron energies near the threshold, the main uncertainty is related to the electron energy scatter determined by the $f(E_e)$ function. The more homogeneous (monoenergetic) the beam, the more pronounced the effect of threshold processes upon the cross sections measured. The main reaction channels are as follows:

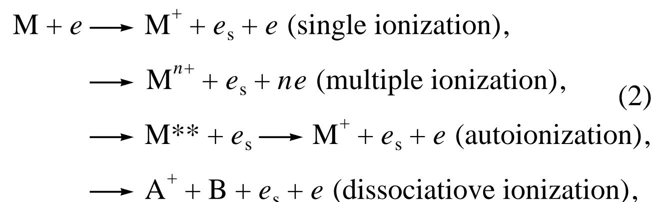

$$\begin{aligned} M + e &\longrightarrow M^+ + e_s + e \text{ (single ionization)}, \\ &\longrightarrow M^{n+} + e_s + ne \text{ (multiple ionization)}, \\ &\longrightarrow M^{**} + e_s \longrightarrow M^+ + e_s + e \text{ (autoionization)}, \\ &\longrightarrow A^+ + B + e_s + e \text{ (dissociatiove ionization)}, \end{aligned} \qquad (2)$$

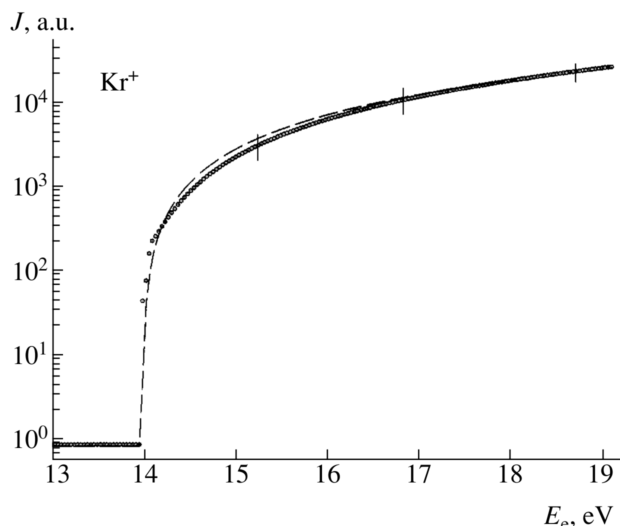

Fig. 1. Near-threshold region of the ionization function of krypton atom determined in this experiment (points) and plotted according to data from [4] (dashed curve).

where M, e_s, and e denote the molecules, scattered electrons, and emitted electrons, respectively.

Since the main purpose of our investigation was to establish the laws of behavior of the ionization function near the threshold, special attention was paid to absolute calibration of the energy scale. This problem is among the most difficult and important in modern mass spectrometry. Uncertainties in determining the real energy of ionizing electrons in the collision region are caused by the presence of contact potential differences between elements of the ion source of the quadrupole mass spectrometer, by a complicated configuration of the electrostatic field in the system, and by some other instrumental factors. Therefore, the accuracy of determination of the ionization potential and the potentials of appearance of various fragment ions in reactions (2) depends on the precision of determining the primary electron energy against an absolute scale.

In order to solve the problem, we employed a method of calibration based on reliable published reference data from [4, 5]. The reference gases for the calibration could be argon or krypton. However, the presence of two close-lying excited states ($^2P_{3/2}$ and $^2P_{1/2}$) of the Ar^+ ion with an energy difference ($\Delta E = 0.178$ eV) smaller than the energy resolution of our experimental setup could result in the appearance of a spurious structure in the ionization cross section near the threshold [4]. From this standpoint, krypton is preferable because the energy gap between the analogous states of the Kr^+ ion ($\Delta E = 0.666$ eV) exceeds the electron energy scatter in the primary beam ($\Delta E_e = 0.5$ eV) and will not lead to the aforementioned additional uncertainties.

In a control experiment, we measured the initial portion of the ionization function for Kr atom. Figure 1 shows this function in comparison to the published data obtained at an energy resolution of $\Delta E_e = 0.05$eV (see [4] and references therein). As can be seen, the two curves are in good agreement, which ensured reliable calibration of the energy scale and confirmed the validity of our experimental procedure. The calibration procedure was multiply (four to five times) repeated in each series of experiments, thus providing for a sufficient accuracy of the energy scale (at least one order of magnitude better than the scatter of electron energies in the primary beam).

As is known, the laws of ionization in the region of threshold energies were originally established by Wannier (see [6]). However, the classical threshold law is not always valid for molecules when the pattern of interactions is complicated by a number of competitive processes (2). Since these aspects have been considered in much detail by Märk (see, e.g, [7]), we will concentrate mostly on the possibility of determining exact values of the appearance thresholds (E_{ap}) for molecular ions and their fragments. This will be done using a nonlinear weighing procedure for fitting by least squares based on the Marcwardt–Levenberg algorithm applied to the standard ion source of a commercial mass spectrometer.

The essence of the proposed method is as follows. The experimentally measured dependence of the ionization cross section σ on the energy of ionizing electrons E_e was fitted near the threshold to a certain function $F(E_e)$ such that

$$F(E_e) = \begin{cases} b & \text{for} \quad E_e \le E_{ap}, \\ b + c(E_e - E_{ap})^n & \text{for} \quad E_e > E_{ap}. \end{cases} \tag{3}$$

As can be seen from Eq. (3), the fitting was performed with respect to four parameters: the background signal b, the energy of appearance of a given fragment ion E_{ap}, the proportionality factor c, and the exponent n in the well-known Wannier's threshold law (see [6]) for the single ionization of atoms. For simple light atoms, the exponent is $n = 1.127$, while the values for heavy atoms and polyatomic molecules can vary. The fitting algorithm was realized using SIGMAPLOT [4], a special program package capable of providing four optimized parameters and determining the corresponding standard deviations upon a large number of iterations. The instrumental electron energy distribution function was considered as a free parameter: it was approximated by the Gauss distribution function centered at a real point E_{ap} with a halfwidth of ΔE_e. The ionization probability, determined by numerical convolution of the fitting function with the electron energy distribution,

$$P(E) = \int_{-\infty}^{+\infty} e^{-\frac{(E_e - E_{ap})^2}{2\Delta E_e}} [b + c(E_e - E_{ap})^n] dE_e \tag{4}$$

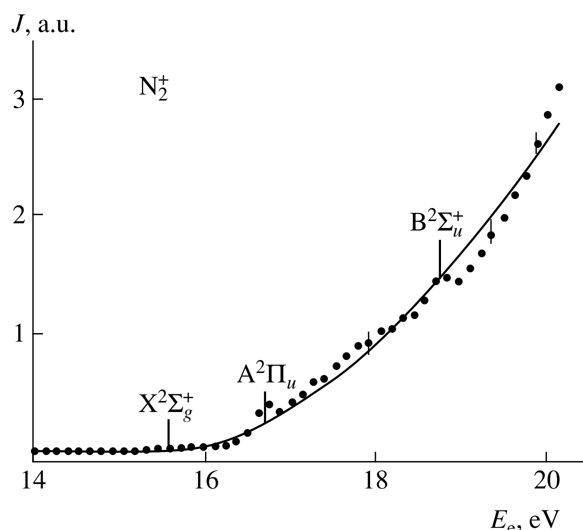

Fig. 2. Near-threshold region of the ionization function of a nitrogen molecule determined in this experiment (points) and fitted by least squares according to the proposed procedure (solid curve). Vertical lines indicate energies of the corresponding excited states.

was compared to experiment. From this procedure, it was possible to obtain information concerning a real halfwidth of the electron energy distribution function.

Figure 2 shows the initial portion of the ionization function for nitrogen molecule. As can be seen, the energy dependence obtained by fitting according to the method describe above (solid curve) perfectly agrees with the experimental plot (points). This allowed us to determine with high reliability the energy threshold of the ionization reaction (E = 15.59 eV). Note the fine structure in the near-threshold region of the cross section. This structure is due to a sequential contribution from the states of the molecular ion N_2^+. Deviation of the cross section from monotonic growth at the primary electron energies in the region of 16.7–18.5 eV is probably related to a contribution from the $A^2\Pi_u$-state of N_2^+ (E = 16.70 eV [8]). Inclusion of an additional ionization channel upon passage through the ionization threshold of states $B^2\sum_u^+$ (E = 18.75 eV [8]) leads to a noticeable bending of the ionization function, followed by a more rapid increase in the cross section. This structure can be explained to result from a contribution due to the process of autoionization to the vibrational levels of the aforementioned states.

Comparative data on the appearance thresholds E_{ap} for some atoms and molecules

Ion/target	E_{ap}, eV		
	NIST database [5]	Märk [7]	this study
Ar^+	15.759	15.749	15.78
Kr^+	13.990	13.999	14.00
N^+/N_2	14.534	–	14.63
O^+/O_2	13.618	–	13.69
N_2^+/N_2	15.581	15.590	15.59
O_2^+/O_2	12.069	12.073	12.09
H_2O^+	12.65	12.56	12.70
D_2O^+	12.6395	12.60	12.65

The values of the energy thresholds for the appearance of some molecular ions (both experimentally measured and determined using the proposed algorithm) are presented in the table. As can be seen, there is good agreement between our values, on the one hand, and the results of Märk [7] and the data taken from the reference electronic tables published by the US National Institute of Standards (NIST) [5], on the other hand. This coincidence confirms the wide possibilities of the method proposed for determining the appearance potentials of ions in experiments with electron beams monoenergetic to within 0.5 eV.

Acknowledgments. The authors are grateful to T.D. Märk and his colleagues from the Institute of Ion Physics (Innsbruck, Austria) for kindly providing the fitting algorithm and for helpful discussions.

REFERENCES

1. A. V. Snegursky and A. N. Zavilopulo, Phys. Res. B **126** (1), 301 (1997).
2. A. N. Zavilopulo, A. V. Snegurskiĭ, E. É. Kontrosh, and I. O. Tsapfel, Pis'ma Zh. Tekh. Fiz. **22** (1), 3 (1996) [Tech. Phys. Lett. **22**, 6 (1996)].
3. A. V. Snegursky, A. I. Zhukov, and A. N. Zavilopulo, in *Abstracts of Contributed Papers of IV European Conference on Atomic and Molecular Physics, ECAMP, Riga, 1992*, p. 424.
4. G. Hanel, B. Gstir, T. Fiegele, *et al.*, J. Chem. Phys. **116**, 2456 (2002).
5. G. Mallard and P. J. Linstrom, *NIST Standard Reference Database* (2000), Vol. 69, http://www.webbook.nist.gov.
6. F. H. Read, in *Electron Impact Ionization*, Ed. by T. D. Märk and G. H. Dunn (Springer-Verlag, Berlin, 1985), pp. 42–88.
7. T. D. Märk, Electr.-Molec. Interact. **1**, 251 (1984).
8. A. Lofthus and P. H. Krupenie, J. Phys. Chem. Ref. Data **6**, 113 (1977).

Translated by P. Pozdeev

Technical Physics Letters, Vol. 28, No. 11, 2002, pp. 916–918. Translated from Pis'ma v Zhurnal Tekhnicheskoĭ Fiziki, Vol. 28, No. 21, 2002, pp. 75–80.
Original Russian Text Copyright © 2002 by Kanareykin, Sheinman, Al'tmark.

Frequency Control in Wake Field Waveguide Structures

A. D. Kanareykin, I. L. Sheinman, and A. M. Al'tmark

St. Petersburg State Electrotechnical University, St. Petersburg, 197376 Russia

e-mail: lab@physics.etu.spb.ru

Received April 12, 2002

Abstract—The possibility to control the frequency spectrum of Vavilov–Cherenkov radiation in a waveguide accelerator structure with the aid of an external ferroelectric layer is studied. A decrease in the permittivity of a ferroelectric material under the action of an applied electric field leads to an increase in the frequency of the wake radiation field of a relativistic electron bunch. Parameters of the ferroelectric layer are calculated proceeding from the required interval of control of the wake field frequency and the tolerable power losses in the waveguide system. *© 2002 MAIK "Nauka/Interperiodica".*

A new method for the acceleration of charged particles, which makes use of the wake fields existing behind electron bunches passing through a dielectric waveguide structure, is now being extensively studied by both experimental and theoretical methods [1]. A complex investigation of the wake acceleration processes in dielectric waveguides is now underway at the St. Petersburg State Electrotechnical University in cooperation with the Argonne National Laboratory (USA).

Wake field acceleration implies a system of energy transfer from a high-current low-energy electron bunch to a low-current high-energy bunch. The primary low-energy bunches excite a Cherenkov electromagnetic wave in a waveguide medium, the longitudinal electric field component of which (with a potential difference of up to ~100 MV) is used to accelerate the low-current electron bunch.

A widely used type of dielectric waveguide [1, 2] is a single-layer waveguide in the form of an evacuated dielectric tube with an internal channel of radius R_c in which electron bunches travel. The external surface of the dielectric tube with a radius of R_w is metal-coated. An important requirement for the waveguide structure of a wake field accelerator is a minimum level of electromagnetic energy losses in the waveguide material. For this reason, waveguides are made of high-Q ceramics with a loss tangent $\tan\delta$ not exceeding 5×10^{-5} and $Qf = 10^5$ at a frequency of $f = 10$ GHz. The permittivity ε_1 of the dielectric is determined by the type of the structural material and can vary within broad limits ($\varepsilon_1 = 4$–36) [1].

The phase relations (ensuring that a low-current bunch is kept in phase with the accelerating wave) pose strict requirements to the waveguide structure parameters and the bunch positioning. By changing the permittivity of the waveguide system, it would be possible to control phase relations in the wave–bunch system so as to ensure the most favorable energy conditions for the acceleration process. This problem is solved by creating a system to control the frequency spectrum of the waveguide which employs a ferroelectric film applied onto the external surface of the dielectric waveguide.

The aim of this study was to model by numerical methods a two-layer waveguide with an additional ferroelectric layer between a dielectric layer with an external radius of R_d and a metal film of radius R_w. In such a waveguide, the spectrum can be controlled by changing the permittivity ε_2 of the dielectric layer under the action of an applied electric field. In other words, the wake field spectrum can be modified on a real time scale in the course of an experiment.

Expressions for the accelerating and deflecting wake fields created by a point relativistic electron bunch in a vacuum channel of the dielectric waveguide can be derived from the Maxwell equations with appropriate boundary conditions in the waveguide:

$$E_z(\zeta, r) = \sum_{n=1}^{\infty} E_{zn}(f_n, r)\cos\left(\frac{2\pi f_n}{c}\zeta\right), \quad (1)$$

$$E_r(\zeta, r) = \sum_{n=1}^{\infty} E_{rn}(f_n, r)\sin\left(\frac{2\pi f_n}{c}\zeta\right), \quad (2)$$

where $\zeta = z - vt$ is the distance behind the bunch, v is the bunch velocity, c is the speed of light in vacuum, f_n are the natural mode frequencies depending on the waveguide geometry and the permittivities of the dielectric (ε_1) and ferroelectric (ε_2) layers, and $E_{zn}(f_n, r)$ and $E_{rn}(f_n, r)$ are the coefficients of series depending on the waveguide geometry, permittivities (ε_1, ε_2), and the bunch charge q.

Real electron bunches are characterized by a spatial distribution of the charge, which is usually described by the normal (Gauss) law. The field of a gaussian bunch can be determined as an integral convolution of the

point-charge field described by Eqs. (1) and (2) with the charge distribution function $p(\zeta)$:

$$F_{z,r}(r,\zeta) = \int_{-\infty}^{\zeta} p(s)E_{z,r}(r, s-\zeta)ds. \qquad (3)$$

The amplitude–frequency characteristic depends on the bunch length: an increase in the length suppresses the high-frequency modes. For a bunch with a length of 0.4 cm moving in a waveguide with $R_c = 0.5$ cm and $R_d = 0.7$ cm, it is sufficient to take into account only the first (lowest frequency) mode.

The ferroelectric layer can be represented by a film of barium strontium titanate $(Ba_{0.6}, Sr_{0.4})TiO_3$ doped with 1% manganese operating at room temperature (300 K). This composition allows the permittivity ε_2 at a frequency of 10 GHz to be varied from 800 (at a loss tangent of $\tan\delta \approx 2 \times 10^{-3}$) to 1820 ($\tan\delta \approx 6 \times 10^{-3}$), which corresponds to a change in the control electrostatic field from 4×10^6 V/m to zero [3]. Increasing the control electrostatic field up to 10^7 V/m decreases the permittivity ε_2 to 365. At a ferroelectric film thickness of 100 μm (in contrast to the 1-μm-thick film studied in [3]), the dielectric loss tangent may exhibit an increase related to inhomogeneities in the film structure. In connection with this, the energy losses presented below were calculated for $\tan\delta = 2 \times 10^{-2}$ (at $\varepsilon_2 = 1800$), 10^{-2} ($\varepsilon_2 = 800$), and 5×10^{-3} ($\varepsilon_2 = 400$).

Figure 1 shows plots of the fundamental frequency of the wake field of the bunch versus permittivity ε_2 calculated for a three-layer dielectric waveguide with $R_c = 0.5$ cm, $R_d = 0.7$ cm, and three values of the waveguide permittivity ($\varepsilon_1 = 5, 7, 9$). The ferroelectric layer thickness $h = R_w - R_d$ was selected so that the field frequency corresponding to the middle of the range of variation of the ferroelectric permittivity ε_2 would be equal to 11.42 GHz, which is the main working frequency of the planned experiment. As can be seen from Fig. 1, the frequency can be varied within ±25% relative to the central wake field frequency $f = 11.42$ GHz at $\varepsilon_1 = 5$. An increase in the permittivity of the dielectric ε_1 leads to narrowing of the frequency control range. The range of the controlled waveguide frequency can be significantly expanded by selecting another relation between the thicknesses of the dielectric and ferroelectric layers, but this leads to a sharp increase in the electrical power losses in the system and deteriorates the bunch acceleration parameters.

The total power losses in the waveguide include the electrical losses in the dielectric and ferroelectric layers and the magnetic losses related to a finite conductivity of the metal film: $w_r = w_d + w_m$. The dielectric losses were calculated by integrating the specific losses over the dielectric and ferroelectric layers: $w_d = \sigma_d \int_V \mathbf{E}\dot{\mathbf{E}}\, dV$.

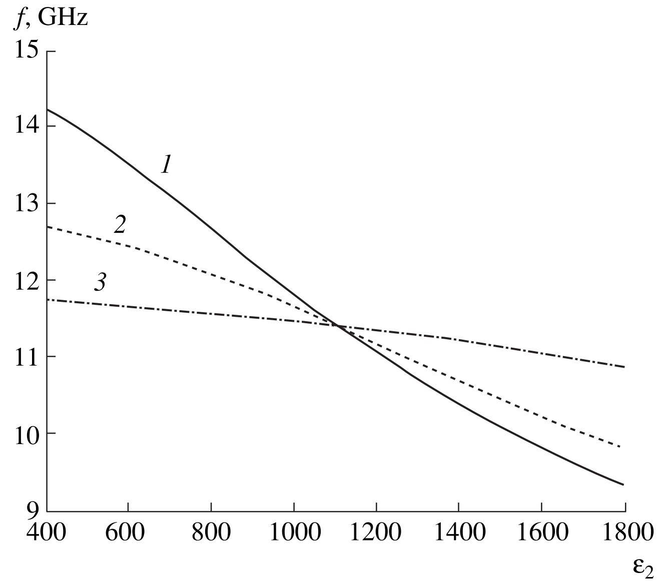

Fig. 1. Plots of the fundamental frequency of the wake field of the bunch versus permittivity of the ferroelectric layer ε_2 calculated for $\varepsilon_1 = 5$ (*1*), 7 (*2*), 9 (*3*) and the ferroelectric layer thickness $h = 0.132$ (*1*), 0.168 (*2*), and 0.183 mm (*3*).

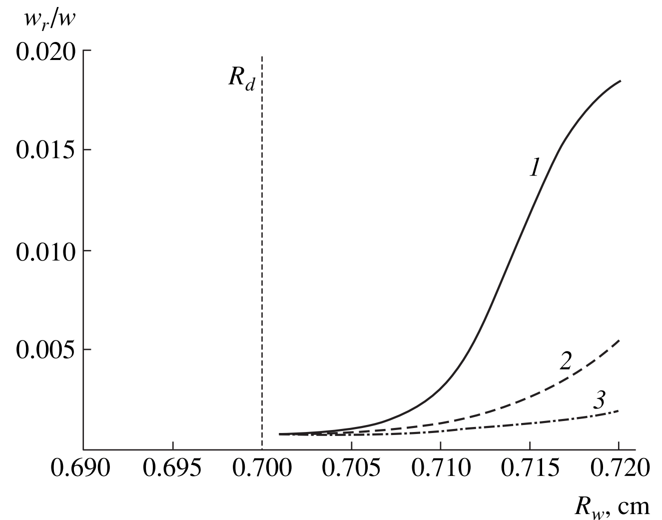

Fig. 2. Plots of the relative energy losses versus the external waveguide radius R_w calculated for $\varepsilon_1 = 9.4$ and $\varepsilon_2 = 1800$ (*1*), 800 (*2*), and 400 (*3*).

The conductivity σ_d is determined from the condition $\tan\delta = \sigma_d/(\omega\varepsilon)$, where ω is the circular frequency. The components of the field $\mathbf{E}$ were calculated using expressions (3) for the wake field behind the relativistic charged bunch. The losses of power in the metal film were calculated as the real part of the flux of the complex Poynting vector through the total conductor area. This value is determined by the tangent component of the magnetic field strength H_τ at the conductor surface: $w_m = 1/(2\Delta\sigma_m)\oint_S H_\tau^2\, ds$. Here, Δ is the skin layer thick-

ness determined by the field frequency ω and the metal conductivity σ_m: $\Delta = \sqrt{2/(\omega\mu\mu_0\sigma_m)}$.

Figure 2 shows plots of the ratio of the total power losses to the power stored in the waveguide versus the external radius R_w for $\varepsilon_1 = 9.4$ and various ε_2. It should be noted that the presence of a ferroelectric layer not only leads to dissipation of a considerable fraction of energy in this layer but also accounts for a sharp increase in losses in the metal film. As a result, the contribution of magnetic losses to the total energy losses in the system becomes dominant and rapidly increases with the permittivity of the ferroelectric layer. This circumstance poses limitations on the ferroelectric film thickness, thus restricting the possibilities of wake field frequency control in the waveguide.

It is also necessary to pay attention to problems related to the effect of high-frequency radiation components on the controllability of a thin ferroelectric layer. Note that the intensity of the high-frequency electric field component significantly decreases in the ferroelectric layer, which minimizes this effect. We believe that this problem can be solved by using the selective methods [4], which will allow the frequency spectrum to be controlled without any influence from an accelerating field.

REFERENCES

1. A. D. Kanareykin, I. L. Sheinman, E. A. Nenasheva, *et al.*, in *Physics at the Turn of the 21st Century: Proceedings of the International Conference, St. Petersburg, Russia, 1998*, p. 57.
2. M. Rosing and W. Gai, Phys. Rev. D **42** (5), 1829 (1990).
3. H.-D. Wu and F. S. Barnes, Integr. Ferroelectr. **22**, 300 (1998).
4. W. Gai and Ching-Hung Ho, J. Appl. Phys. **70** (7), 3955 (1991).

Translated by P. Pozdeev

Technical Physics Letters, Vol. 28, No. 11, 2002, pp. 919–922. Translated from Pis'ma v Zhurnal Tekhnicheskoĭ Fiziki, Vol. 28, No. 21, 2002, pp. 81–90.
Original Russian Text Copyright © 2002 by Gundienkov, Yakovlenko.

The Interaction between Charged Dust Particles in a Plasma

V. A. Gundienkov and S. I. Yakovlenko

Institute of General Physics, Russian Academy of Sciences, Moscow, 117924 Russia

Received April 4, 2002

Abstract—A solution to the Poisson–Boltzmann equation for a cloud of charges surrounding two charged dust particles, considered as Debye atoms forming a Debye molecule, is studied by numerical methods. It is demonstrated that attractive forces between the particles arise when two conditions are satisfied. First, the Debye screening radius, corresponding to the electron density at a half average spacing between particles, must be equal to approximately half of this distance. In this case, the attraction arises at a distance equal approximately to the average spacing between particles. Second, charges of one sign must be concentrated predominantly on the particles. Should the particles possess only a small fraction of charges of one sign, they will repulse at any distance. Estimates of the electrostatic pressure and surface tension in a gas of dust particles are obtained. © *2002 MAIK "Nauka/Interperiodica".*

Introduction

This paper is a continuation of our study [1] of the interaction between charged dust particles occurring in a cloud (plasma) of thermodynamically equilibrium charges. Previously [1], the analysis was concentrated on a thermoemission plasma, in which case positively charged particles are surrounded by a cloud of electrons. Here, we pay more attention to a different situation, whereby the particles are surrounded by a plasma containing charges of both signs.

Formulation of the Problem

Poisson–Boltzmann equation. Similar to the previous considerations [1–9], this analysis proceeds from the Poisson–Boltzmann equation in the dimensionless form:

$$\Delta\varphi = \exp(\varphi) - \delta\exp(-\varphi),$$
$$\nabla\mathbf{E} = -(\exp(\varphi) - \delta\exp(-\varphi)), \quad \mathbf{E} = -\nabla\varphi. \tag{1}$$

Here, the distances are expressed in units of the Debye screening radius $r_D = (T/4\pi e^2 N_{e0})^{1/2}$, corresponding to the electron density N_{e0} at the points of zero potential, and T is the gas temperature. The dimensionless variables (potential φ, field strength $\mathbf{E}$, and electron density n_e) are defined through the corresponding dimensional quantities (ϕ, $-\nabla\phi$, N_e) by the following relations: $\varphi = \phi e/T$, $\mathbf{E} = -\nabla\phi e r_D/T$, and $n_e = r_D^3 N_e = n_D\exp(\varphi)$, where $n_D^3 = r_D N_{e0}$. In Eq. (1), $\delta = N_{i0}/N_{e0}$ is a parameter characterizing additional ionization of the gas and N_{i0} and N_{e0} are the ion and electron densities at the points of zero potential. Owing to the quasi-neutrality of the plasma, $0 \le \delta \le 1$.

In the numerical estimates, we will usually proceed from the experimental conditions in [10], according to which $N_{e0} = 2.5 \times 10^{10}$ cm^{-3} and $T = 0.146$ eV = 1700 K. In this case, the characteristic values are as follows: $r_D = 18$ μm, $T/e = 0.146$ V, and $T/er_D = 80$ V/cm. For an average particle radius of $r_p = 0.4$ μm ($r_0 = r_p/r_D = 2.23 \times 10^{-2}$) and a charge of $Z_p e = 500e$, the electric field strength at the particle surface is estimated at $Z_p e/r_0^2 = 4.5 \times 10^4$ V/cm ($E_0 = E(r_0) = 550$).

Boundary conditions. The particles surface is characterized by a constant potential $\varphi|_S = \varphi_0 = \text{const}$. A solution to the Poisson–Boltzmann equation gives the field strength $\mathbf{E}_0$ on the particle surface. The resultant force is determined by integrating the electrostatic pressure over the particle surface. The particle charge is determined upon properly selecting the potential φ_0. The force of interaction between particles F is related to the dimensionless force f as $F = (T^2/8\pi e^2)f$.

Results for a Debye Molecule in a Cloud of Charges of the Same Sign ($\delta = 0$)

Selecting the calculation parameters. For exact determination of the force acting upon a particle, the method used for solving the Poisson–Boltzmann equation has to provide for maximum accuracy in the vicinity of the particle surface. Of most interest is the case when the distances between particles significantly exceed their diameters. This is difficult to achieve in the usual systems of coordinates. For this reason, we have used special coordinates constructed for a particular case (see [1] for details), the well-known oval of Cassini [11, 12].

The numerical calculations were performed for the parameters φ_0, r_0, and a_0, which correspond to a single Debye atom at $d \gg a_0$. For this purpose, we first solved a spherically symmetric problem in which the field strength and potential at $r = a_0$ were set equal to zero.

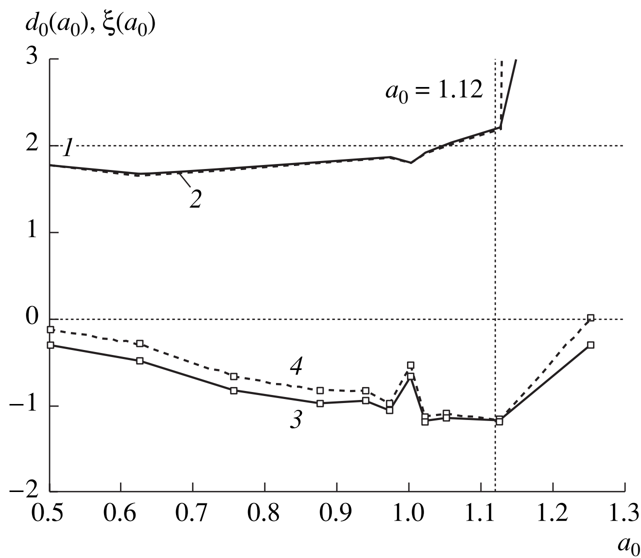

Fig. 1. Plots of (*1*, *2*) the coordinate d_0 of the point where the force changes sign and (*3*, *4*) the force slope ξ at d_0 versus the Debye atom size a_0. Solid curves (*1*, *3*) correspond to the case when the potential φ_0 on the particle surface is independent of d; dashed curves (*2*, *4*) correspond to a constant particle charge at a selected $\varphi_0(d)$. The φ_0 value was determined for $r_0 = 1$ at a given a_0.

From a solution to this problem, we determined the potential φ_0 on a particle of the given radius r_0. With this set of φ_0, r_0, and a_0 values, we solved a two-center problem for $d = 10a_0$. The results for the spherically symmetric and two-center problem coincided to a high precision. The subsequent series of calculations was performed for smaller d values.

In order to determine how the force of interaction between particles depends on the distance d between them, we performed a series of calculations with various sets of φ_0, r_0, and a_0. However, the particle charge z_0 proved also to depend on d (here, z_0 is the dimensionless charge related to the particle charge Z_p expressed in units of the elementary charge by the formula $Z_p = 4\pi z_0 n_D$). For this reason, additional calculations were performed using φ_0 or a_0 modified so as to make the z_0 value independent of d.

The force of interaction between particles as a function of the distance. The calculations showed that repulsion takes place at small distances ($d \sim r_0$) between particles. In the previous calculation [1], oriented to the parameters of a thermoemission plasma ($a_0 = 7.55$) [10], the attraction changes to repulsion at a distance $d_0 \approx 1.3$, which is slightly smaller than the average spacing between particles $2a_0 = 1.51$. The value of the equilibrium distance $d = d_0$ depends only weakly on the type of quantities (φ_0, a_0 versus z_0, a_0) set constant in the course of the distance variation. Once the force of attraction $F(2a_0)$ between particles for the average spacing between them is known, we can estimate the electrostatic pressure compressing a gas of such dust particles,

$$P_E \approx F(2a_0)N_p^{2/3} = (T^2/8\pi e^2)N_p^{2/3}f(2a_0),$$

and the surface tension in a “dust fluid,”

$$\sigma_E \approx FN_p^{1/3} = (N_p^{1/3}T^2/8\pi e^2)f(2a_0),$$

by comparing the electrostatic pressure to the gaskinetic pressure of the particles:

$$P_E/N_pT = (T/8\pi e^2 N_p^{1/3})f(2a_0).$$

Under the experimental conditions [10]: $|f(2a_0)| \approx 0.2$, $P_E = 9.7 \times 10^{-7}|f(2a_0)|$ Torr $\approx 2 \times 10^{-7}$ Torr, $\sigma_E = 3.5 \times 10^{-9}|f(2a_0)|$ N/m $\approx 7 \times 10^{-10}$ N/m, and $P_E/N_pT \approx 20$. We may suggest that, under these experimental conditions, a gas of Debye atoms mixed with an inert gas will exhibit a tendency to contraction. Such a situation was considered in [13–15]. An analysis of the effect of the interaction between Debye atoms on the gasdynamic properties of a dusty plasma falls outside the scope of this short publication.

Dependence on the size of a Debye atom. We performed a series of calculations with various values of a_0 (Fig. 1). The results showed that attraction takes place only for $a_0 \leq 1$; even at a spacing of $a_0 > 1.12$, the point where the force changes sign goes to a large distance ($d_0 > 4a_0$).

The condition of $a_0 = a_p/r_D < 1$ can be rewritten for the dimensional quantities as $N_{e0} > N_{ecr} \equiv \dfrac{T}{\pi e^2}N_p^{3/2}$. The electrostatic compressive forces vanish when $d_0 = 2a_0$ (i.e., when $a_0 = 1$). Accordingly, the relation $a_0 = 1$ or $N_e = N_{ecr}$ is the condition of equilibrium for a gas of Debye atoms. The condition of a sufficiently large particle charge ($z_p > 1/3$) can be rewritten for the particle charge expressed in the units of electron charge: $Z_p > Z_{ecr} \equiv \dfrac{\pi}{6}\dfrac{N_{ecr}}{N_p}$. Under the experimental conditions, $N_{ecr} = 4.4 \times 10^{10}$ cm^{-3} and $Z_{ecr} = 460$, which agrees with the experimentally measured values of $N_{e0} \approx 2.5 \times 10^{10}$ cm^{-3} and $Z_p \approx 500$ [10].

The force of interaction between Debye atoms can be characterized by the slope of the dimensionless force at the point of intersection with the abscissa axis:

$$\xi = f'(d)|_{d = d_0} = U''(d)|_{d = d_0}.$$

Using the ξ value, we can express the frequency of oscillations of the dust particles around their equilibrium positions as $\omega = |\xi|^{1/2}\omega_0$, where $\omega_0 = v_T/a_p$, $v_T = (2T/m_p)^{1/2}$ is the thermal velocity of the particles, and m_p is the particle mass. Under the experimental conditions of [10], $m_p \sim 2 \times 10^{-12}$ g, $v_T \sim 0.5$ cm/s, and $a_p \sim 1.4 \times$

10^{-3} cm. This yields $\omega_0 = 357$ s^{-1} for the oscillation frequency and $2\pi/\omega_0 = 18$ ms for the period of oscillations. As can be seen from Fig. 1, the strongest attraction takes place for $0.5 < a_0 < 1$. Under these conditions, a gas of Debye atoms tends to contraction (cf. [15]).

Effect of the dust particle size. Let us consider the case when a small conducting ball is replaced by an analogous ball of greater size with the charge partly compensated by free charges on the shell of the Debye atom. There arises a natural question as to how adequate this change is. We performed several series of calculations using different values of r_0 and, accordingly, φ_0. When the particle radius was small compared to the Debye radius a_0, the difference was insignificant (Fig. 2). For example, in the case of $a_0 = 0.755$, variation of the particle radius in the interval of $r_0 = 0.1$–0.2 (with the φ_0 value corresponding to a given r_0), the point where the attraction changes to repulsion ($d_0 = 1.28$) exhibits a scatter of less than 2%, which agrees with the accuracy of our calculations.

The dust particle size becomes significant for $r_0 > 0.3a_0$. For $r_0 > 0.4$, the polarization attraction decreases very significantly, so that the distance at which the attraction changes to repulsion significantly exceeds the average spacing between particles ($d_0 > 2a_0$). From this we conclude that a considerable contribution to the polarization forces comes from charges occurring at distances $r \approx 0.3a_0$ from the particle center, rather than only from the periphery of the Debye atom ($r \approx a_0$).

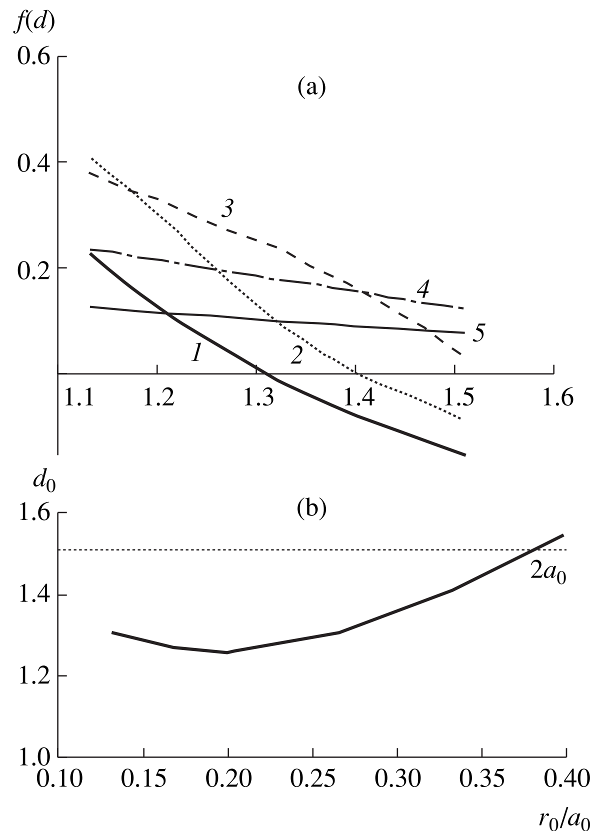

Fig. 2. Data illustrating the dependence of the coordinate d_0 at which the repulsion changes to attraction on the dust particle radius r_0: (a) plots of the force f versus distance d between particles in the vicinity of the coordinate d_0 for r_0 = 0.2 (*1*), 0.25 (*2*), 0.3 (*3*), 0.4 (*4*), and 0.5 (*5*); (b) plots of d_0 versus r_0/a_0, where r_0 can be considered as the radius of a region in which polarization of the charged cloud is ignored. The potential φ_0 for $r = r_0$ was determined at $a_0 = 0.755$.

Results for a Debye Molecule in a Cloud of Charges of Both Signs ($\delta \neq 0$)

The force of interaction between particles as a function of the distance. Similarly to the case of $\delta = 0$, the dependence of the force of interaction between particles on the distance d was determined by conducting a series of calculations with various sets of φ_0, r_0, and a_0 for the Debye atom. Additional calculations were also performed using φ_0 or a_0 modified so as to make the particle charge z_0 independent of d. Also as in the case of $\delta = 0$, the value of r_0 was selected to exceed the atomic core radius, so as to model the dust particle using a conducting ball of greater size with the charge partly compensated by free charges on the shell of the Debye atom. Thus, the atomic core polarization was ignored.

The results presented in Fig. 3 were calculated using the a_0 values selected for different δ so as to correspond to a limiting (maximum possible) charge for the experimental dust particle radius $r_0 = 2.23 \times 10^{-2}$ [10]. This was performed using trial methods. The so obtained functions $z(r)$ and $\varphi(r)$ were used to calculate $z_0 = z(r_0)$ and $\varphi_0 = \varphi(r_0)$ for $r_0 = 0.1$.

For $1 - \delta \ll 1$, the dust particles never exhibited attraction at a distance shorter that the average spacing between them. The attraction for $d < 2a_0$ appears only when the particles bear a considerable fraction of the overall positive charge of the plasma (see Fig. 3 for $\delta < 0.5$). The smaller the fraction of charge in the plasma, the stronger the maximum attractive force and the deeper the potential well.

The decrease in the attractive forces with increasing δ is readily explained. Indeed, the attractive forces appear because electrons accumulate at the axis x between the centers of particles, thus ensuring their attraction to the center of the Debye molecule. This attraction exceeds the repulsion of particle charges screened by the internal layers of the electron shells of the Debye atoms. For $1 - \delta \ll 1$, the effect of the particle charge screening by the internal layers of the electron shells remains the same, but the attraction toward the center of the Debye molecule significantly weakens because not only electrons (binding the particles), but also the positive charges (inducing repulsion), tend to concentrate at the center of the Debye molecule.

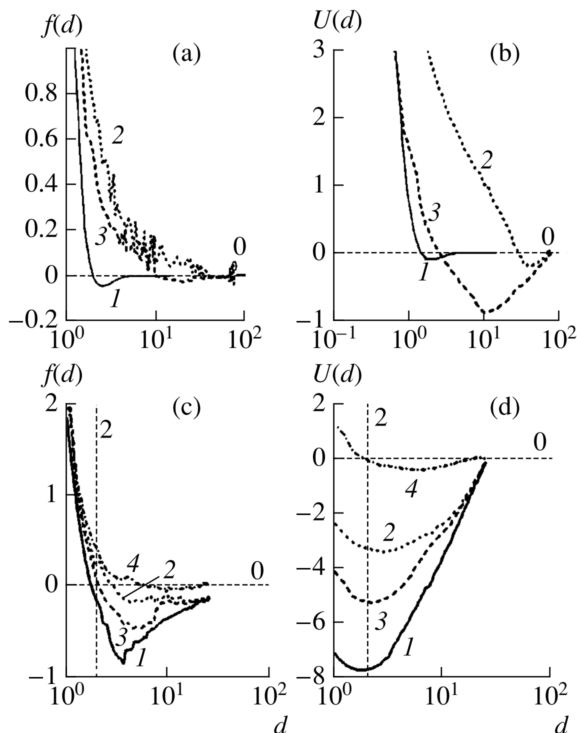

Fig. 3. Plots of (a, c) the force projection f onto the x axis and (b, d) the potential energy of interaction U versus distance d between particles for various $\delta \neq 0$ (the potential energy is normalized so that $U(75) = 0$ (b) and $U(25) = 0$ (d)); in all cases, $r_0 = 0.1$): (a, b) curves *1* correspond to the analytical expression taken from [17]: $f(d) = \text{const}(1/d)(1 + d - 1/2d^2)\exp(-d)$; $U(d) = \text{const}(1/d^2)(1 - 1/2d)\exp(-d)$; the repulsive part of the curves was matched to the results of numerical calculations by setting const = 12; $\delta = 0.999$ (*2*) and 0.9 (*3*); (c, d) $\delta = 0.1$ (*1*), 0.3 (*2*) 0.5 (*3*) and 0.7 (*4*).

Regarding analytical approaches. The above conclusion concerning the absence of attraction for $1 - \delta \ll 1$ is at variance with the results of recent approximate analytical descriptions [16, 17], (Fig. 3). According to these results [16, 17] based on the linearized Poisson–Boltzmann equation, dust particles must attract for $\delta = 1$ in the region of $r > (3^{1/2} + 1)/2^{1/2} = 1.93$.

We believe that the results obtained in [16, 17] are misleading, apparently, for the following reasons. According to [16, 17], the force acting directly on a particle is supplemented by an attractive force acting on the electron shell of one particle from another particle. This approximation would be justified if the charged shells of the particles were tightly bound to them by some other forces. However, no such additional forces are involved in the problem under consideration. The presence of an additional force attracting the electron shell of one atom to another charge [16, 17] is only indicative that this charged shell configuration is nonequilibrium: the force of attraction to the other charge will lead to polarization of the charged shell, which was not taken into account in [16, 17]. There are no reasons to add this polarization force to the force acting directly upon a dust particle.

Conclusion

Taking into account that the attractive forces arise only at a distance on the order of the average spacing between particles, the problem of description of the properties of dusty fluids and crystals can be correctly solved only with allowance made for the many body interactions in the system of particles. In fact, the polarization forces acting upon the dust particles fluctuate and depend on the arrangement of the surrounding particles. However, the results of our analysis indicate that an equilibrium configuration of such particles has to take place.

Acknowledgments. The authors are grateful to A.N. Tkachev for fruitful discussion of our results and papers [13, 14] and to Yu.I. Syts'ko for discussions concerning computational aspects of the problem.

REFERENCES

1. V. A. Gundienkov and S. I. Yakovlenko, Pis'ma Zh. Tekh. Fiz. **28** (10), 46 (2002) [Tech. Phys. Lett. **28**, 422 (2002)].
2. A. N. Tkachev and S. I. Yakovlenko, Zh. Tekh. Fiz. **69** (1), 53 (1999) [Tech. Phys. **44**, 48 (1999)].
3. A. N. Tkachev and S. I. Yakovlenko, Pis'ma Zh. Tekh. Fiz. **25** (1), 52 (1999) [Tech. Phys. Lett. **25**, 21 (1999)].
4. S. I. Yakovlenko, Pis'ma Zh. Tekh. Fiz. **25** (16), 83 (1999) [Tech. Phys. Lett. **25**, 670 (1999)].
5. S. I. Yakovlenko, Kratk. Soobshch. Fiz., No. 9, 3 (1999).
6. S. I. Yakovlenko, Pis'ma Zh. Tekh. Fiz. **26** (8), 47 (2000) [Tech. Phys. Lett. **26**, 337 (2000)].
7. S. I. Yakovlenko, Pis'ma Zh. Tekh. Fiz. **26** (23), 38 (2000) [Tech. Phys. Lett. **26**, 1045 (2000)].
8. S. I. Yakovlenko, Pis'ma Zh. Tekh. Fiz. **27** (9), 83 (2001) [Tech. Phys. Lett. **27**, 389 (2001)].
9. S. I. Yakovlenko, Kratk. Soobshch. Fiz., No. 1, 3 (2002).
10. V. E. Fortov, A. P. Nefedov, O. F. Petrov, *et al.*, Zh. Éksp. Teor. Fiz. **111** (2), 467 (1997) [JETP **84**, 256 (1997)].
11. *Mathematical Encyclopedia*, Ed. by Yu. V. Prokhorova (Bol'shaya Ross. Éntsiklopediya, Moscow, 1995).
12. I. N. Bronshteĭn and K. A. Semendyaev, *Mathematical Handbook* (Nauka, Moscow, 1964).
13. S. A. Mayorov, A. N. Tkachev, and S. I. Yakovlenko, Usp. Fiz. Nauk **164** (3), 298 (1994) [Phys. Usp. **37**, 279 (1994)].
14. S. A. Mayorov, A. N. Tkachev, and S. I. Yakovlenko, Phys. Scr. **51**, 498 (1995).
15. S. I. Yakovlenko, Izv. Vyssh. Uchebn. Zaved., Fiz. **38** (4), 3 (1995); Russ. Phys. J. **38** (4), 329 (1995).
16. D. N. Gerasimov and O. A. Sinkevich, Teplofiz. Vys. Temp. **37** (6), 853 (1999).
17. A. S. Ivanov, Phys. Lett. A **290**, 304 (2001).

Translated by P. Pozdeev

Technical Physics Letters, Vol. 28, No. 11, 2002, pp. 923–924. Translated from Pis'ma v Zhurnal Tekhnicheskoĭ Fiziki, Vol. 28, No. 21, 2002, pp. 91–94.
Original Russian Text Copyright © 2002 by Malkovich.

Alternative Analytical Solutions of the Diffusion (Thermal Conductivity) Equation for an Arbitrary Initial Concentration (Temperature) Distribution

R. Sh. Malkovich

Ioffe Physicotechnical Institute, Russian Academy of Sciences, St. Petersburg, 194021 Russia

Received June 20, 2002

Abstract—Alternative analytical solutions of the diffusion (or thermal conductivity) equation are presented, which ensure rapid convergence even for small values of Dt/l^2 ($\alpha t/l^2$), where D is the diffusion coefficient, α is the thermal diffusivity, t is the time, and l is the characteristic size. The solutions possess a general character and are valid for an arbitrary initial distribution of the concentration (temperature). © *2002 MAIK "Nauka/Interperiodica".*

For the diffusion (or thermal conductivity) equation

$$\frac{\partial c}{\partial t} = D\frac{\partial^2 c}{\partial x^2}\left(\text{or } \frac{\partial T}{\partial t} = \alpha\frac{\partial^2 T}{\partial x^2}\right), \tag{1}$$

where c is the diffusant concentration, T is the absolute temperature, x is the coordinate, t is the time, D is the diffusion coefficient, and α is the thermal diffusivity, the well-known analytical solutions are conventionally expressed for a finite body (with a characteristic size l) in the form of a series. Convergence of this series depends on the quantity Dt/l^2 (at/l^2): the greater this value, the higher the rate of convergence. For a small value of the ratio, the series converges rather slowly.

This Letter presents alternative analytical solutions of the diffusion (or thermal conductivity) equation, which ensure rapid convergence for small values of Dt/l^2 (at/l^2), for example, in early stages of the process. The proposed solutions possess a general character and are valid for an arbitrary initial distribution of the concentration (temperature). To the author's knowledge, general solutions of this type have never been reported in the literature. For the sake of brevity, we will consider only the diffusion equation; all results are readily applicable to the case of thermal conductivity.

Consider a finite body ($0 \le x \le l$) with absorbing [$c(0, t) = c(l, t) = 0$, $t > 0$] or impermeable [$\frac{\partial c}{\partial x}(0, t) = \frac{\partial c}{\partial x}(l, t) = 0$, $t > 0$] boundaries. By using the Laplace transform

$$w(x) = \int_0^\infty \exp(-pt)c(x, t)dt, \tag{2}$$

Eq. (1) can be written as

$$D\frac{d^2 w}{dx^2} - pw + c(x, 0) = 0, \tag{3}$$

where $c(x, 0)$ is the initial concentration distribution. As can be readily shown, a solution to Eq. (3) can be written as follows:

$$w(x) = \frac{1}{2qD\sinh ql}\left\{\int_0^x c(\xi, 0)[\cosh q(l - x + \xi) \mp \cosh q(l - x - \xi)]d\xi + \int_x^l c(\xi, 0) \times [\cosh q(l + x - \zeta) \mp \cosh q(l - x - \xi)]d\xi\right\}, \tag{4}$$

where $q = \sqrt{p/D}$ and the upper (lower) sign corresponds to the absorbing (impermeable) boundaries. By expanding the quantity $\frac{\cosh qz}{\sinh ql}$ (z is a parameter) into series with respect to exponents and passing to the original, we eventually arrive at

$$c(x, t) = \frac{1}{2\sqrt{\pi Dt}}\int_0^l c(\xi, 0)$$

$$\times\left\{\left[\exp\left(-\frac{(\xi-x)^2}{4Dt}\right)\mp\exp\left(-\frac{(\xi+x)^2}{4Dt}\right)\right]\right.$$

$$+\sum_{k=1}^{\infty}\left[\exp\left(-\frac{(2kl+x-\xi)^2}{4Dt}\right)+\exp\left(-\frac{(2kl-x+\xi)^2}{4Dt}\right)\right. \tag{5}$$

$$\left.\left.\mp\exp\left(-\frac{(2kl+x+\xi)^2}{4Dt}\right)\mp\exp\left(-\frac{(2kl-x-\xi)^2}{4Dt}\right)\right]\right\}d\xi,$$

where the upper (lower) sign corresponds, as above, to the case of absorbing (impermeable) boundaries.

The obtained expression (5) provides for a rapid convergence even with small values of the ratio Dt/l^2. For example, in the case of diffusion into an infinitely thin layer with impermeable boundaries occurring in the plane $x = 0$, the exact solution $c(0, t) = 5.641896Q/l$ (Q is the amount of a substance in the layer) for $Dt/l^2 = 0.01$ is obtained via traditional formulas [1–3] using twelve terms of the series, while formula (6) gives the same value as the first term in the expansion. For $\frac{l}{\sqrt{Dt}} = \infty$, formula (5) converts into the well-known expressions for diffusion into a semibounded body ($0 \le x \le \infty$) with an absorbing [$c(0, t) = 0$, $t > 0$] or impermeable [$\frac{\partial c}{\partial x}(0, t) = 0$, $t > 0$] boundary [1–3].

In addition to the case of diffusion with an arbitrary initial distribution of the diffusant concentration, let us consider the case of a finite body ($0 \le x \le l$) in which the impurity is absent at the initial time instant but is maintained at a constant concentration on both boundaries during the whole process: $c(x, 0) = 0$, $c(0, t) = c_1$, $c(l, t) = c_2$, $t > 0$.

In this case, a solution to Eq. (3) can be written as follows:

$$w(x) = \frac{c_1}{p}\frac{\sinh q(l-x)}{\sinh ql}+\frac{c_2}{p}\frac{\sinh qx}{\sinh ql}. \tag{6}$$

Upon expanding the quantity $\frac{\sinh qz}{\sinh ql}$ (z is a parameter) into series with respect to exponents and passing to the original, we obtain

$$c(x,t) = \sum_{k=0}^{\infty}\left\{c_1\left[\operatorname{erfc}\frac{2kl+x}{2\sqrt{Dt}}-\operatorname{erfc}\frac{2(k+1)l-x}{2\sqrt{Dt}}\right]\right.$$

$$\left.+c_2\left[\operatorname{erfc}\frac{2(k+1)l-x}{2\sqrt{Dt}}-\operatorname{erfc}\frac{2(k+1)l+x}{2\sqrt{Dt}}\right]\right\}. \tag{7}$$

This solution, like expression (5) above, provides for a rapid convergence even when the Dt/l^2 value is small. For example, in the case of $Dt/l^2 = 0.01$, $c_1 = 1$, and $c_2 = 2$, the exact solution $c(0.05l, t) = 0.723674$ is obtained via traditional formulas [1–3] using eleven terms of the series, while formula (7) again gives the same value as the first term in the expansion.

REFERENCES

1. J. Crank, *The Mathematics of Diffusion* (Clarendon, Oxford, 1956).
2. H. S. Carslaw and J. C. Jaeger, *Conduction of Heat in Solids* (Clarendon Press, Oxford, 1956; Nauka, Moscow, 1964).
3. R. Sh. Malkovich, *The Mathematics of Diffusion in Semiconductors* (Nauka, St. Petersburg, 1999).

Translated by P. Pozdeev

Technical Physics Letters, Vol. 28, No. 11, 2002, pp. 925–926. Translated from Pis'ma v Zhurnal Tekhnicheskoĭ Fiziki, Vol. 28, No. 22, 2002, pp. 1–6.
Original Russian Text Copyright © 2002 by Meshkovsky, Shannikov.

Phase Distortions in an Anisotropic Luneberg Lens

I. K. Meshkovsky and D. V. Shannikov

Institute of High-Precision Mechanics and Optics (Technical University), St. Petersburg, Russia

e-mail: igorkm@spb.runner.ru

Received May 29, 2002

Abstract—The field phase distribution over the aperture of a Luneberg lens composed of radial dielectric rods is approximately calculated, and the influence of this distribution on the directivity pattern of this antenna is estimated. The results of calculations of the difference of electrical pathlengths for the angles $\varphi = 0$ and 90° for $\Delta\varepsilon = 0.2$ are presented. © *2002 MAIK "Nauka/Interperiodica".*

In recent years, a large number of investigations were devoted to electrodynamic calculations of spherical microwave lens antennas (see, e.g., [4, 5]). Such an antenna typically represents a system of spherical layers possessing different permittivities, which are selected so as to ensure (to within a certain accuracy) the required radial permittivity profile calculated using the laws of geometric optics. In the simplest case, when the permittivity of the outermost layer tends to unity, the profile is described by the Luneberg law [3].

Since manufacturing spherical layered structures is rather difficult, spherical lenses are usually made of dielectric elements of various types [1, 2]. Recently [2], we suggested composing a lens from cone-shaped dielectric rods of variable radius originating from the center (Fig.1). By using rods with a properly selected variation of the radius along the length, it is possible to obtain a required radial profile of the effective permittivity. However, there arises another problem because the artificial medium is anisotropic and the permittivity is essentially a tensor quantity. As an electromagnetic wave propagates in such a lens, orientation of the electric field vector relative to the axes of dielectric rods changes differently in various cross sections of the lens. This breaks the central symmetry of the lens structure and leads to defocusing of the wave.

Below, we present an approximate calculation of the field phase distribution over the aperture of a lens composed of radial dielectric rods and estimate the influence of such a distribution on the directivity pattern of this antenna.

Dielectric permittivity tensor. Consider an infinite structure composed of dielectric rods of the same diameter remaining constant along the rod. With the diameter of rods and their spacing (spatial period) properly selected, this structure can model a region inside the lens in which the divergence of rods can be ignored. If the spacing of rods is small as compared to the wavelength, the effective permittivity can be calculated in the quasi-static approximation. In the case when the field vector is parallel to the axis of the rod, the calculation yields

$$\varepsilon_{\mathrm{eff}\parallel} = 1 + d(\varepsilon - 1), \quad (1)$$

and for the perpendicular orientation, we obtain

$$\varepsilon_{\mathrm{eff}\perp} = \frac{\varepsilon + 1 + d(\varepsilon - 1)}{\varepsilon + 1 - d(\varepsilon - 1)}, \quad (2)$$

where d is the relative volume fraction filled by the dielectric material and ε is the relative permittivity of this material. Relations (1) and (2) indicate that a maximum difference between $\varepsilon_{\mathrm{eff}\perp}$ and $\varepsilon_{\mathrm{eff}\parallel}$ takes place for

$$d = \frac{\varepsilon + 1}{\varepsilon - 1}\left(1 - \sqrt{\frac{2}{\varepsilon + 1}}\right), \quad (3)$$

amounting

$$\Delta\varepsilon = \varepsilon_{\mathrm{eff}\parallel} - \varepsilon_{\mathrm{eff}\perp} = d(1 - d)\frac{(\varepsilon - 1)^2}{\varepsilon + 1 - d(\varepsilon - 1)}. \quad (4)$$

For $\varepsilon = 2.5$ (a material of the polystyrene type), this yields $d = 0.57$ and $\Delta\varepsilon = 0.215$. The experiments performed for the structure with a spatial period of 0.3λ and a permittivity of $\varepsilon = 2.5$ [7] confirmed the validity of the above relations. Once the $\varepsilon_{\mathrm{eff}\perp}$ and $\varepsilon_{\mathrm{eff}\parallel}$ values are known, the permittivity tensor of a medium of this type can be determined.

Let the axes of rods be parallel to the plane of the electric vector of a wave propagating in the medium under consideration. According to [6], the effective retardation coefficient of this wave can be written as

$$\frac{1}{n_{\mathrm{eff}}^2} = \frac{\sin^2\gamma}{\varepsilon_{\mathrm{eff}\parallel}} + \frac{\cos^2\gamma}{\varepsilon_{\mathrm{eff}\perp}}, \quad n_{\mathrm{eff}}^2 = \varepsilon_{\mathrm{eff}}, \quad (5)$$

where γ is the angle between the direction of the electromagnetic wave propagation and the axis of the rod. Taking into account that $\Delta\varepsilon$ is small, we obtain

$$\varepsilon_{\mathrm{eff}} = \varepsilon_{\mathrm{av}} - \frac{\Delta\varepsilon}{2}\cos 2\gamma. \quad (6)$$

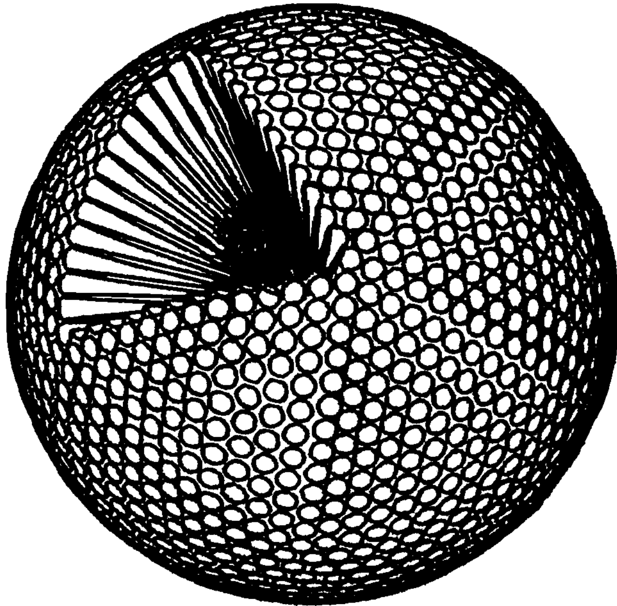

Fig. 1. Schematic diagram of the proposed lens structure.

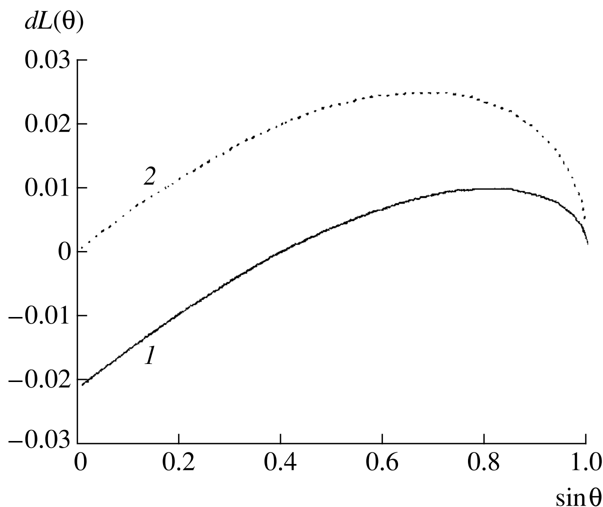

Fig. 2. The field phase distribution in an anisotropic lens calculated for $\varphi = 0$ (*1*) and 90° (*2*).

The value of γ can be determined from the beam refraction equation

$$n_0 \sin\gamma_0 = rn(r)\sin\gamma(r), \tag{7}$$

where γ_0 and n_0 are the known angle and index of refraction at the beam entrance in and exit out of the crystal. Assuming the fraction d of the volume filled by the dielectric to be small and considering $\varepsilon_{\rm eff}$ and $n_{\rm eff}$ as linear functions of d, we obtain

$$\varepsilon_{\rm eff} = 1 + (\varepsilon_{\rm av} - 1)\left(1 - \frac{\Delta\varepsilon}{2}\cos 2\gamma\right), \tag{8}$$

$$n_{\rm eff} = 1 + (\varepsilon_{\rm av} - 1)\left(1 - \frac{\Delta\varepsilon}{2}\cos 2\gamma\right). \tag{9}$$

Wave phase distortion in an anisotropic lens. The wave phase distribution over the lens aperture can be approximately calculated taking into account that the anisotropy is usually small and assuming that the beam trajectories in an anisotropic lens differ only slightly from those in an isotropic one, in which $n(r)$ coincides with $n_{\rm av}(r)$ for the anisotropic lens. The field phase on the aperture is determined by the electrical pathlength of the wave traveling from the radiator to the exit aperture. Consider the case when $n_{\rm av}(r)$ corresponds to the Luneberg law and ensures the equiphase condition for the field on the aperture of an isotropic lens. Then, the phase difference at a point on the aperture of the anisotropic lens under consideration can be determined using the relation

$$\Delta L(\rho, \varphi) = \int\limits_{l(\rho,\varphi)} (n_{\rm eff}(l) - n_{\rm av}(l))dl, \tag{10}$$

where $\Delta L(\rho, \varphi)$ is a change in the electrical pathlength, $l(\rho, \varphi)$ is the wave pathlength in the lens body, of the wave within the lens body; ρ and φ are the polar coordinates of the given point.

For the calculation, the φ value was fixed and the selected cross section was characterized by two components of the electric field vector, one lying in this section and the other, perpendicular to this plane. Obviously, $n_{\rm eff}$ for the latter component corresponds to the case of $\gamma = 0$. Therefore, the wave field on the aperture obeys the equiphase condition and is elliptically polarized.

Figure 2 presents the results of the calculation of the electrical pathlength difference using Eq. (10) for the polar angles $\varphi = 0$ (curve *1*) and 90° (curve *2*) in a lens made of rods with $\Delta\varepsilon = 0.2$. The former case corresponds to the electric field vector **E** lying in the cross section, while the latter case represents the field component perpendicular to this plane. The results of this calculation allow the field structure on the lens aperture to be described for an arbitrary radiator.

REFERENCES

1. K. A. Zimmerman and D. L. Runyan, *Luneberg Lens and Method of Constructing Same*, US Patent No. 5677796 (1997).
2. I. K. Meshkovsky and D. V. Shannikov, RF Patent No. 3333333 (2000).
3. S. P. Morgan, J. Appl. Phys. **29**, 1358 (1958).
4. H. Schrank and J. Sanford, IEEE Antennas Propag. Mag. **37** (1), 76 (1995).
5. A. D. Greenwood and J. M. Jin, IEEE Antennas Propag. Mag. **41** (5), 9 (1999).
6. L. D. Landau and E. M. Lifshitz, *Course of Theoretical Physics*, Vol. 8: *Electrodynamics of Continuous Media* (Nauka, Moscow, 1992; Pergamon, New York, 1984).
7. D. V. Shannikov and B. B. Lebedev, in *Proceedings of the V All-Russia Conference on Problems in Science and the Higher School, St. Petersburg, 2001*, p. 135.

Translated by P. Pozdeev

Technical Physics Letters, Vol. 28, No. 11, 2002, pp. 927–928. Translated from Pis'ma v Zhurnal Tekhnicheskoĭ Fiziki, Vol. 28, No. 22, 2002, pp. 7–10.
Original Russian Text Copyright © 2002 by Saidov, Razzakov, Saparov.

Liquid Phase Epitaxy of $(Sn_2)_{1-x}(InSb)_x$ Solid Solution Layers

A. S. Saidov, A. Sh. Razzakov, and D. V. Saparov

Physical Engineering Institute, "Solar Physics" Research and Production Corporation, Academy of Sciences of the Republic of Uzbekistan, Tashkent, Uzbekistan

Received March 14, 2002

Abstract—Epitaxial layers of $(Sn_2)_{1-x}(InSb)_x$ solid solutions were grown from an indium-based solution melt confined between two horizontal GaAs substrates in a temperature interval from 325 to 200°C. Scanning microprobe and X-ray diffraction investigations of the GaAs–$(Sn_2)_{1-x}(InSb)_x$ heterostructures showed that crystallographic perfection of the epitaxial layers depends on the epitaxial growth conditions. *© 2002 MAIK "Nauka/Interperiodica".*

The development of IR detectors, in particular, for IR viewers, has stimulated investigations aimed at obtaining and characterizing new narrow-bandgap materials and related device structures. From this standpoint, the synthesis and study of semiconductor materials belonging to $(C_2^4)_{1-x}(A^3B^5)_x$ narrow-bandgap solid solutions are among the important problems of microelectronic technology. Previously [1, 2], we demonstrated the principal possibility of growing epitaxial layers of solid solutions of the $(C_2^4)_{1-x}(A^3B^5)_x$ and $(C_2^4)_{1-x}(A^2B^6)_x$ types.

Here, we report on the possibility of growing solid solutions of the $(Sn_2)_{1-x}(InSb)_x$ system by liquid phase epitaxy (LPE) from a limited volume of an In–Sn–Sb solution melt confined between substrates in a temperature interval from 325 to 200°C. The substrates were (100)-oriented polished plates of *n*-GaAs with a free charge carrier density of $(4–7) \times 10^{17}$ cm^{-3} and plates of semiinsulating GaAs with a resistivity of $\rho \geq 10^7$ Ω cm. The In–Sn–Sb solution–melt composition was determined from using the corresponding phase diagrams [3] using solubility data for the binary components. The epitaxial growth onset temperature was 325–260°C; the melt cooling rate was 0.5–2 K/min. The epitaxial layer thicknesses varied from 4 to 154 μm, depending on the spacing between substrates and on the epitaxial growth regime. Under certain selected LPE conditions, we succeeded in growing perfect crystalline mirror-smooth epitaxial films.

The surface composition of the samples grown as described above was studied using a JEOL X-ray microprobe. It was established that the epitaxial material represents a solid solution with the composition $(Sn_2)_{0.05}(InSb)_{0.95}$. The scanning micrographs of the sample surface measured using the SnK_α, InK_α, and SbK_α characteristic X-ray emission lines showed that macroscopic defects and metal inclusions were absent and the solid solution components were homogeneously distributed over the epitaxial layer.

The structural perfection of the epitaxial layers was also checked by X-ray diffraction. The measurements were performed on a DRON-UM1 diffractometer using specially prepared epitaxial layers with a thickness of d = 4–5 μm. The diffraction spectra were obtained by continuous recording using the CuK_α (λ_α = 1.5418 Å) and CuK_β (λ_β = 1.3922 Å) radiations from an X-ray tube with a copper anode operating at 30 kV and 10 mA. The time of exposure was varied within 1–3 h.

The typical diffractogram presented in Fig. 1 displays, in addition to a diffraction maximum due to the substrate (a_{GaAs} = 5.654 Å), two clearly pronounced and closely spaced peaks due to the film, which correspond to the lattice parameters of InSb (a_{InSb} = 6.475 Å) and the $(Sn_2)_{0.05}(InSb)_{0.95}$ solid solution (a_{ss} = 6.486 Å). The

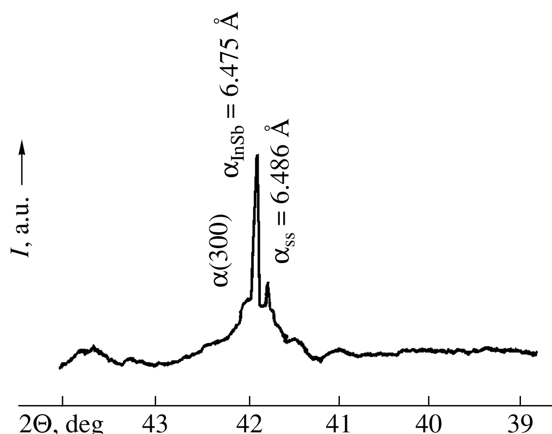

Fig. 1. A typical X-ray diffractogram of the GaAs–$(Sn_2)_{1-x}(InSb)_x$ epitaxial heterostructure with $x = 0.95$.

1063-7850/02/2811-0927$22.00 © 2002 MAIK "Nauka/Interperiodica"

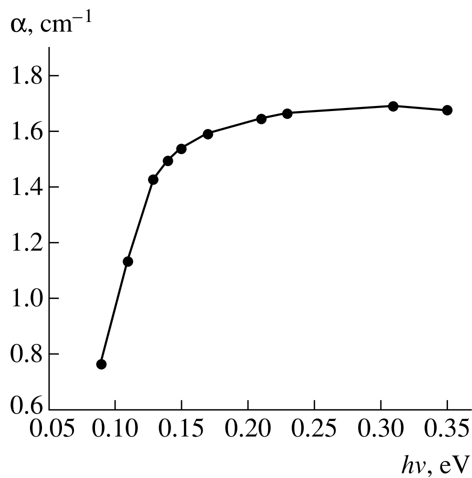

Fig. 2. A typical spectral dependence of the optical absorption of GaAs–$(Sn_2)_{1-x}(InSb)_x$ heterostructures.

absence of other peaks in the diffractogram is additional evidence of a single crystal structure of the epitaxial layers [4]. It was established that the shapes and positions of diffraction peaks depend on the LPE conditions.

An analysis of the surface distribution of components using the X-ray fluorescence spectra measured on a Siemens SPS-300 spectrometer confirmed that the concentration of Sn in the solid solution amounts to 5.1 at. %.

We also measured the optical absorption spectra of the GaAs–$(Sn_2)_{1-x}(InSb)_x$ heterostructures in the far IR region. The measurements were performed with a double-beam Specord 71-IR spectrophotometer. The spectrum presented in Fig. 2 shows that the absorption edge of the film is shifted toward longer wavelengths, which indicates a decrease in the bandgap width as compared to that of InSb (indeed, estimated from the half-decay of the absorption intensity, the bandgap width of the film studied is $E_g = 0.11– 0.12$ eV).

Thus, the results of our investigations showed, for the first time, the existence of $(Sn_2)_{1-x}(InSb)_x$ solid solutions with a tin content of 5.1 at. % and a bandgap width of $E_g = 0.11–0.12$ eV. Intentionally undoped, epitaxial layers of the $(Sn_2)_{1-x}(InSb)_x$ solid solutions grown exhibited conductivity of the *p*-type. Under specially selected growth conditions, it is possible to obtain crystallographically perfect epitaxial layers of $(Sn_2)_{1-x}(InSb)_x$ solid solutions by LPE on GaAs substrates.

REFERENCES

1. Zh. I. Alferov, M. Z. Zhingarev, S. G. Konnikov, *et al.*, Fiz. Tekh. Poluprovodn. (Leningrad) **16** (5), 831 (1982) [Sov. Phys. Semicond. **16**, 532 (1982)].
2. M. S. Saidov, A. S. Saidov, É. A. Koshchanov, and A. Sh. Razzakov, Dokl. Akad. Nauk **359** (2), 188 (1998) [Dokl. Phys. **43**, 169 (1998)].
3. M. Hansen and K. Anderko, *Constitution of Binary Alloys* (McGraw-Hill, New York, 1958; Metallurgizdat, Moscow, 1962), Vol. 2.
4. A. S. Saidov, É. A. Koshchanov, and A. Sh. Razzakov, Pis'ma Zh. Tekh. Fiz. **24** (2), 12 (1998) [Tech. Phys. Lett. **24**, 47 (1998)].

Translated by P. Pozdeev

Technical Physics Letters, Vol. 28, No. 11, 2002, pp. 929–931. Translated from Pis'ma v Zhurnal Tekhnicheskoĭ Fiziki, Vol. 28, No. 22, 2002, pp. 11–16.
Original Russian Text Copyright © 2002 by Kamilov, Khusanov, Bakhadyrkhanov, Kobilov.

Nonselective Polycrystalline Radiation Detectors Based on Higher Manganese Silicides

T. S. Kamilov, A. Zh. Khusanov, M. K. Bakhadyrkhanov, and D. K. Kobilov

Tashkent State Aviation Institute, Tashkent, Uzbekistan
Kokand State Pedagogical Institute, Kokand, Uzbekistan
Tashkent State Polytechnical University, Tashkent, Uzbekistan

Received June 11, 2002

Abstract—The films of higher manganese silicides (HMSs) obtained by the oblique deposition of manganese vapor onto silicon substrates possess a preferred texture and exhibit anisotropic thermo emf. The main parameters of IR detectors based on these HMS films have been studied. It is shown that the detectors with ~5-μm-thick HMS films possess an electric resistance of ~200 Ω and are capable of monitoring time variations of the incident radiation with a characteristic response time of $\leq 10^{-6}$ s and a transformation coefficient of 500 μV/W. *© 2002 MAIK "Nauka/Interperiodica".*

Experimental data on the electrical characteristics of polycrystalline films of higher manganese silicides (HMSs) with the composition $MnSi_{1.71-1.75}$ are very restricted [1, 2]. However, investigation of the kinetic properties of these films is of interest from the standpoint of both basic knowledge and practical applications. It was established [3–5] that massive single crystal HMS samples exhibit a strongly anisotropic kinetic behavior at $T \geq 300$ K which is retained in the range of intrinsic conductivity at temperatures up to 1000 K. Below, we report on the possibility of obtaining HMS films possessing anisotropic thermo emf by the deposition of manganese vapor at high temperatures onto silicon substrates.

In the detectors possessing anisotropic thermo emf [6], the response signal is measured in the direction perpendicular to the temperature gradient caused by the radiation. The response speed of such detectors is characterized by the time of establishing the temperature gradient across the thickness h of the sensitive element [6]:

$$\tau = \frac{h^2}{a}, \qquad (1)$$

where $a = \lambda/c\rho$ is the thermal diffusivity [m^2/s], λ is the thermal conductivity [W/(m K)], c is the specific heat [J/(kg K)], and ρ is the density [kg/m^3]. According to [6, 7], the conversion coefficient S for single crystals is independent of the sensor thickness:

$$S = k\frac{\Delta a}{2\lambda b}\sin 2\varphi, \qquad (2)$$

where k is the absorption coefficient [m^{-1}], $\Delta\alpha = \alpha_\parallel - \alpha_\perp$, $\alpha_\parallel$ is the thermo emf along the tetragonal crystal axis (c axis) [V/K], $\alpha_\perp$ is the thermo emf in the direction perpendicular to the c axis[V/K], b is the distance between contacts [m], and φ is the angle between the normal to the surface and the c axis.

Fabrication of single crystal plates with thicknesses $h \leq 10$ μm, which, according to (1), possess a characteristic time of $\tau \leq 10^{-5}$ s, is a difficult task to solve and requires the consumption of a massive initial material. According to [3], the deposition of metals possessing anisotropic properties in the single crystal state, with a molecular beam of the evaporated metal making an angle θ (deposition angle) with the substrate normal, leads to textured films with preferred orientation in one of the crystallographic directions at an angle $\varphi \neq 0$ relative to the substrate surface normal. Therefore, oblique deposition allows films possessing anisotropic thermo emf to be obtained [6, 7].

The HMS films on silicon substrates were obtained in a high-vacuum reactor evacuated to a dynamic residual pressure of 10^{-5}–10^{-6} Torr by a high-speed pumping stage (450 l/s). The films were deposited onto (111)-oriented single crystal silicon substrates of the KDB-10 and KDB-3000 grades. Prior to charging substrates into the reactor, their surfaces were mechanically ground and chemically polished. Manganese was preliminarily purified by double sublimation and evaporated at $T \geq$ 1130°C for 15–20 min. The amount of evaporated metal was determined by calculating the evaporation time required for the complete deposition onto a given substrate. The films were formed in the course of a reactive diffusion of manganese vapor into the silicon substrate. A single technological cycle in such a reactor could be used to obtain films of manganese silicides at various substrate temperatures (T_1) and manganese vapor deposition angles (θ = 0–90°), which allowed optimum values of the temperature and angle ensuring synthesis of the desired phases and structures to be determined.

1063-7850/02/2811-0929$22.00 © 2002 MAIK "Nauka/Interperiodica"

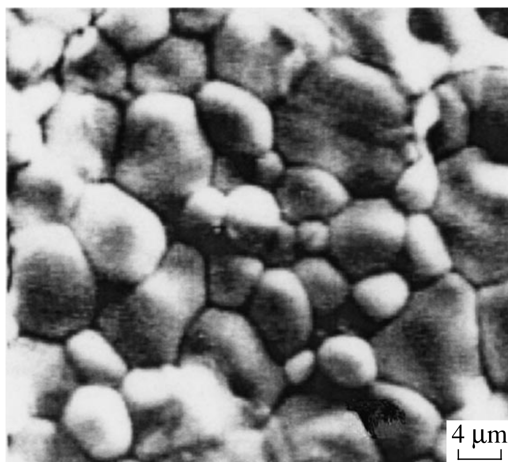

Fig. 1. Surface morphology of an HMS film.

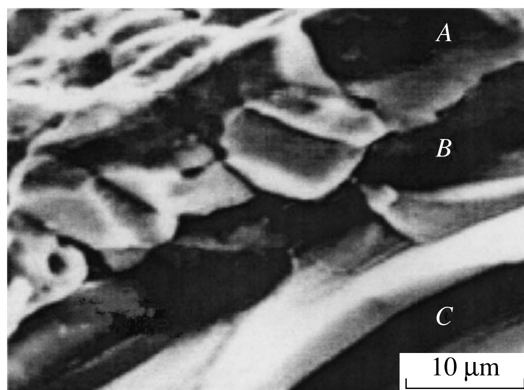

Fig. 2. Micrograph of the transverse cut of an HMS film on a silicon substrate showing (*A*) the columnar structure (texture) of HMS microcrystals, (*B*) the amorphized transition or polycrystalline layer, and (*C*) the silicon substrate.

The deposited films were studied using the Van der Pauw method to determine the electric resistance and the Hall coefficient. The Hall coefficient was positive in the entire temperature range; the charge carrier concentration was $p \cong 10^{19}$–10^{20} cm^{-3}; and the thermo emf ranged within $\alpha = 150$–200 μV/K, and the electric conductivity ranged within $\sigma = 10$–15 $(\Omega\ \mathrm{cm})^{-1}$, depending on the substrate temperature T_1. The compositions and structures of the HMS films were studied using X-ray diffraction and electron microscopy. Analyses for the phase compositions and structures of the deposits were performed using X-ray scattering, electron diffraction, and transmission electron microscopy [2, 8]. The results of these investigations allowed us to determine optimum conditions for the synthesis of polycrystalline films at a substrate temperature from 950 to 1040°C. The films deposited under these conditions consisted predominantly of higher manganese silicides and monosilicide.

Figure 1 shows a typical morphology of the HMS film surface examined using a scanning electron microscope. As can be seen from these data, the films of manganese silicide grown at $T_1 = 1020$–1040°C consist predominantly of grains with dimensions ranging from 3 to 12 μm. Figure 2 presents a micrograph of the transverse cleavage of a typical sample. In this image, region *A* represents a columnar structure (texture) of HMS grains [8, 9], region *B* is a transition layer, and region *C* is the silicon substrate. According to [10], the concentration of boron in the transition layer *B* at the film–substrate interface is smaller than that in the volume of silicon, which is explained by the impurity segregation. This circumstance decreases shunting of the films by the substrate. As can be seen from Fig. 2, the columnar structure exhibits deviation from the substrate normal, which gives rise to anisotropic thermo emf. The possibility of growing columnar structures with different angles of deviation from the substrate normal will be reported in a separate publication.

The response speed characteristic τ and the conversion coefficient S of the films were studied on samples placed into a shielded case. The emf arising between contacts of a sample was measured with the aid of an oscillograph or a measuring amplifier of the V7-8 type. The contacts were formed by depositing 1-mm-wide silver or aluminum strips spaced at 8 mm. The S and τ values were measured using (i) radiation pulses with a wavelength of $\lambda = 1.06$ μm and a pulse duration of 40–200 ns, (ii) radiation with $\lambda = 10.6$ μm modulated at a frequency of 10^2–10^4 Hz or a pulse width of 0.1–0.5 μs, and (iii) radiation of an incandescent lamp with the same modulation. It was found that HMS films with a thickness of 5–7 μm on silicon substrates are characterized by a response time $\tau \le 10^{-6}$ s and S above 500 μV/W (irrespective of the radiation wavelength).

Based on the data of structural analysis and examination of the morphology of the samples deposited at $T_1 = 1000$–1040°C, we established that the HMS films possess a continuous columnar fine-grained polycrystalline morphology and consist mostly of HMS phases with the crystals oriented predominantly along the substrate normal. These HMS films offer the following advantages:

(i) anisotropic thermo emf;

(ii) chemical resistance to aggressive media in a broad temperature range;

(iii) HMS film formation through reactive diffusion of manganese vapor into the silicon substrate, which accounts for a high adhesion of the film to the matrix and for good stability under the action of mechanical factors;

(iv) technical parameters: spectral sensitivity in a wavelength range of up to 200 μm; conversion coefficient at $\lambda = 10.6$ μm, $S = 500$–2000 μV/W; time constant (response speed), $\tau \le 10^{-6}$ s; cell resistance, not exceeding 200 Ω.

Based on the HMS films, it is possible to create nonselective detectors of thermal radiation capable of measuring the fast-rate processes involved in data recording in memory devices and data transfer via various channels.

REFERENCES

1. Ch. Krontiras, K. Pomoni, and M. Roilos, J. Phys. D **21**, 509 (1988).
2. S. I. Adasheva, I. Abdullaev, E. A. Vyaz'mina, *et al.*, Izv. Akad. Nauk, Ser. Fiz. **57** (2), 133 (1993).
3. *Silicides of Transition Metals from Fourth Period*, Ed. by P. V. Gel'd and F. A. Sidorenko (Metallurgiya, Moscow, 1971).
4. G. V. Samsonov, L. A. Dvorina, and B. M. Rud', *Silicides* (Metallurgiya, Moscow, 1979).
5. V. I. Andreev, A. B. Granovskii, A. E. Engalychev, *et al.*, in *Abstracts of VI All-Union Conference, Moscow, 1986*, p. 22.
6. V. K. Zaitsev, in *CRC Handbook of Thermoelectrics*, Ed. by D. M. Rowe (CRC Press, Boca Raton, 1985), p. 299.
7. L. I. Anatychuk, *Thermoelements and Thermoelectric Devices* (Naukova Dumka, Kiev, 1979).
8. V. I. Andreev, A. B. Granovskii, and V. A. Yakovlev, Kvantovaya Élektron. (Moscow) **12** (6), 1295 (1985).
9. T. S. Kamilov, B. L. Sadullaev, U. Sh. Ganiev, and B. T. Kamilov, Semicond. Sci. Technol. **13**, 496 (1998).
10. T. S. Kamilov, V. A. Chirva, and D. K. Kobilov, Semicond. Sci. Technol. **14**, 1012 (1999).

Translated by P. Pozdeev

Technical Physics Letters, Vol. 28, No. 11, 2002, pp. 932–934. Translated from Pis'ma v Zhurnal Tekhnicheskoĭ Fiziki, Vol. 28, No. 22, 2002, pp. 17–22.
Original Russian Text Copyright © 2002 by Parchinskii.

The Effect of γ Radiation on the Electrical Properties of Passive Coatings Based on Lead Borosilicate Glasses

P. B. Parchinskii

National University of Uzbekistan, Tashkent, Uzbekistan

e-mail: pavelphys@mail.ru

Received June 19, 2002

Abstract—The effect of irradiation with γ-quanta in a dose range from 10^4 to 2×10^7 rad on the electrical properties of passive coatings based on low-melting lead borosilicate glasses was studied. It is shown that the irradiation leads to accumulation of a positive charge in the volume of passive coatings. The radiation-induced charge exhibits saturation at an irradiation dose above 5×10^6 rad. *© 2002 MAIK "Nauka/Interperiodica".*

Low-melting lead borosilicate glasses are widely used in semiconductor microelectronics for obtaining passive and insulating layers [1, 2]. For this reason, it is important to study the influence of various external factors, in particular, radiation, on the electrical properties of these coatings. An important parameter determining the effect of irradiation upon the characteristics of such passive coatings is the effective density of the radiation-induced surface charge Q_S accumulated per unit area of the semiconductor–insulator interface [3]. This paper presents the results of investigating the effect of γ radiation on the Q_S value of passive lead borosilicate glass coatings on silicon substrates, which were determined by the method of high-frequency capacitance–voltage (*C*–*V*) measurements.

The passive glass coatings were deposited onto (111)-oriented *n*-Si substrates from a suspension of finely dispersed glass in isopropyl alcohol. The deposition was performed by electrophoresis and followed by fusing the deposit for 5–10 min at 700°C. The glass coating composition and initial electrical characteristics were analogous to those reported previously [4]. The high-frequency *C*–*V* measurements were performed on samples representing metal–insulator–semiconductor (MIS) structures prepared by vacuum deposition of a control electrode with an area of 0.01 cm^2 onto the glass surface and of an ohmic contact onto the silicon substrate. The material used for both the control electrode and the ohmic contact was aluminum. The average thickness of a passive glass coating determined from the maximum capacitance of the MIS structures was $(3 \pm 0.3) \times 10^{-4}$ cm. The *C*–*V* curves were measured at a probing voltage frequency of 150 kHz; the measurements were performed at 23°C in the dark. The samples were irradiated (in a nonbiased state) by γ-quanta emitted from a ^{60}Co source.

Figure 1 shows typical high-frequency *C*–*V* curves obtained for one of the sample structures before and after irradiation with γ-quanta to various doses in the range from 10^4 to 2×10^7 rad (for the sake of clarity, the curve corresponding to a dose of 10^7 rad is omitted). All curves are normalized to a maximum value of C_0 = 22 pF. As can be seen, irradiation with an increased dose of γ-quanta leads to a shift of the *C*–*V* curves toward more negative voltages. This fact is indicative of

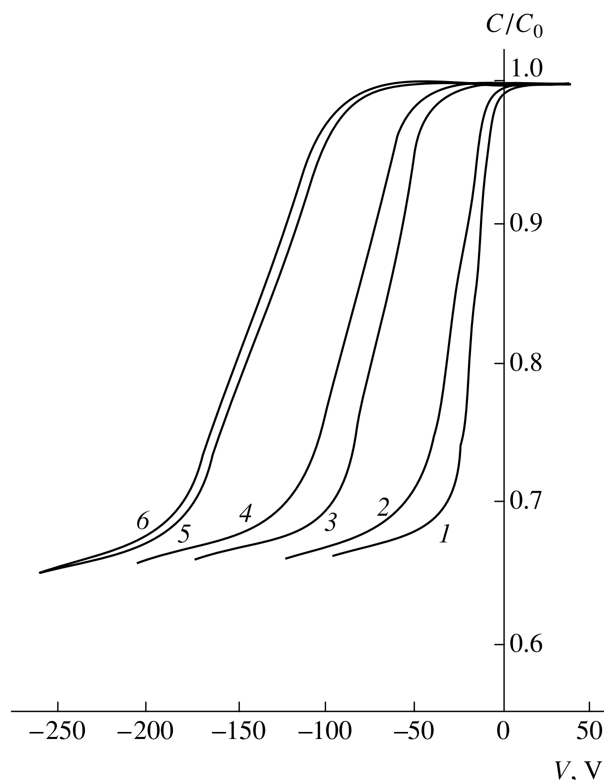

Fig. 1. Typical high-frequency *C*–*V* curves of an MIS structure measured (*1*) before and after irradiation with γ-quanta to a dose of 10^4 rad and (*2*–*6*) after irradiation to a dose of 10^5, 5×10^5, 10^6, 5×10^6, and 2×10^7 rad, respectively.

1063-7850/02/2811-0932$22.00 © 2002 MAIK "Nauka/Interperiodica"

a positive charge Q_S being accumulated in the glass, the amount of which increases with the irradiation dose. This is accompanied by a change in the slope of the *C–V* curves, which is evidence of an increase in the density of surface states at the Si–glass interface [3]. A certain decrease in the minimum capacitance of the MIS structures observed for the irradiation doses above 10^6 rad can be explained by partial charge compensation in the semiconductor substrate taking place as a result of the radiation-induced defect formation [5]. Indeed, the effective charge carrier concentration in the structures studied, determined by the method described in [6], decreased from $n_0 = 1.2 \times 10^{14}$ cm^{-3} before irradiation to $n_0 = 1 \times 10^{14}$ cm^{-3} in the samples irradiated to a maximum dose of 2×10^7 rad.

The radiation-induced surface charge Q_S and its influence on the characteristics of the subsurface region of silicon are conveniently characterized by the value of the flat band potential $V_{\rm fb}$ determined as

$$V_{\rm fb} = Q_{SF}/C_0, \quad (1)$$

where Q_{SF} is the effective surface charge density corresponding to the flat band potential and C_0 is the capacitance of the sample structure [3].

Figure 2 shows the dose dependence of the $V_{\rm fb}$ value determined by comparing the experimental *C–V* curves presented in Fig. 1 with the theoretical curves calculated as described in [3]. A change in the flat band voltage from $V_{\rm fb} = -14$ V in the unirradiated samples to $V_{\rm fb} = -132$ V in the structures irradiated to 2×10^7 rad corresponds to accumulation of a positive charge at a surface density of about $Q_{SF} = 2.5 \times 10^{-7}$ C/cm^2.

At the same time, it should be noted that the samples irradiated to a small dose of 10^4 rad exhibit neither a shift of the *C–V* curve nor a change in the $V_{\rm fb}$ value, which implies that no charge is accumulated in the glass volume. This is evidence of a considerable radiation stability of passive coatings based on the glasses studied, which is higher than the radiation stability of some other widely used coating materials, such as silicon dioxide obtained by the thermal oxidation of silicon (in the latter oxide film, a considerable accumulation of charge is observed already after irradiation to a dose of 10^4 rad [5, 7]). Another feature to be noted is that irradiation to a dose above 5×10^6 rad leads to a less pronounced shift of the *C–V* curves along the voltage axis, while the $V_{\rm fb}$ value virtually ceases to change. This is evidence of a "saturation" of the amount of charge Q_S accumulated in the volume of passive glass coatings.

The appearance of the radiation-induced surface charge Q_S in the volume of a glass coating can be explained by the production of "spatially separated" electron–hole pairs. Electrons not involved in the recombination can leave the dielectric, while less

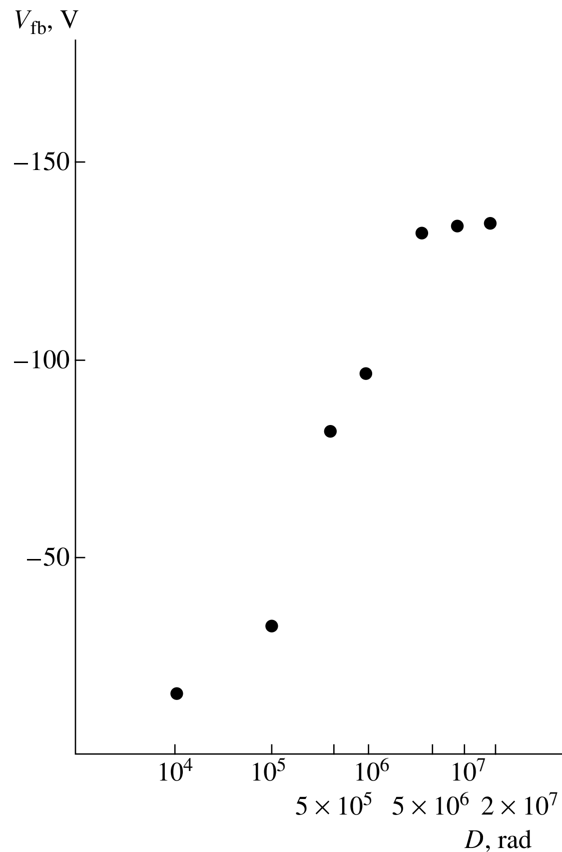

Fig. 2. A plot of the flat band voltage $V_{\rm fb}$ versus γ-radiation dose *D* for the MIS structures studied.

mobile holes are captured on the traps in the glass volume [7]. In the glasses under consideration, the role of such traps can be performed by the atoms of nonbridging oxygen [8] and/or by the ions of trivalent silicon [7, 8]. An increase in the amount of charge trapped in the glass gives rise to an internal electric field, which hinders spatial separation of the electron–hole pairs and increases the probability of their recombination [6]. In addition, the presence of a positive charge in the dielectric layer leads to the formation of an electron-rich layer in the subsurface region of Si, which accounts for the possible injection of electrons from this layer into the glass volume [4] (the injection of electrons from an enriched layer to the volume of lead boron silicate glasses was observed in [9]). The above factors account for stabilization of the Q_S value despite a further increase in the irradiation dose.

The radiation stability of the passive coatings based on the glasses studied, which is higher than the radiation stability of silicon dioxide films obtained by the thermal oxidation of silicon, can be explained by the presence of trapping centers for both electrons and holes in these coatings. The role of such traps can be performed by positively charged lead ions (Pb^{2+}) [8]. The presence of such centers may lead to a partial compensation of the hole charge (captured on traps) by the

trapped electrons. This leads to a decrease in the Q_S value found in the volume of passive coatings based on the lead borosilicate glasses.

REFERENCES

1. P. L. Flowers, J. Electrochem. Soc. **128** (10), 2179 (1981).
2. M. Shimbo, K. Furukava, K. Tanzava, *et al.*, J. Electrochem. Soc. **134** (1), 156 (1987).
3. S. Sze, *Physics of Semiconductor Devices* (Wiley, New York, 1981; Mir, Moscow, 1984), Vol. 1.
4. S. I. Vlasov, P. B. Parchinskii, and B. A. Olmatov, Neorg. Mater. **36** (5), 608 (2000).
5. V. S. Vavilov, B. M. Gorin, N. S. Danilin, A. E. Kiv, Yu. A. Nurov, and V. I. Shakhovtsev, *Radiation Methods in Solid-State Electronics* (Radio i Svyaz', Moscow, 1990).
6. K. H. Zaineger and F. P. Heiman, Solid State Technol. **13**, 49 (1970).
7. V. S. Pershenkov, V. D. Popov, and A. V. Shal'nov, *Surface Radiation Effects in Integrated Circuits* (Énergoatomizdat, Moscow, 1998).
8. Yu. V. Shchapova and A. F. Zatsepin, Izv. Akad. Nauk SSSR, Ser. Fiz. **52**, 1614 (1988).
9. S. I. Vlasov, P. B. Parchinskii, A. A. Nasirov, *et al.*, Zh. Tekh. Fiz. **69** (8), 141 (1999) [Tech. Phys. **44**, 998 (1999)].

Translated by P. Pozdeev

Technical Physics Letters, Vol. 28, No. 11, 2002, pp. 935–938. Translated from Pis'ma v Zhurnal Tekhnicheskoĭ Fiziki, Vol. 28, No. 22, 2002, pp. 23–31.
Original Russian Text Copyright © 2002 by Sorokin, Savkina, Shuman, Lebedev, Mosina, Hutchison.

Features of the Structure of a Porous Silicon Carbide Layer Obtained by Electrochemical Etching of a 6H-SiC Substrate

L. M. Sorokin[a],*, N. S. Savkina[a], V. B. Shuman[a], A. A. Lebedev[a], G. N. Mosina[a], and G. Hutchison[b]

[a] *Ioffe Physicotechnical Institute, Russian Academy of Sciences, St. Petersburg, 194021 Russia*
[b] *Department of Materials, Oxford University, Perks Road, Oxford OXI 3PH, UK*
* *e-mail: lev.sorokin@mail.ioffe.ru*
Received July 2, 2002

Abstract—Transverse sections of the (11–20) cuts of a 6H-SiC substrate–porous SiC layer–epitaxial 6H-SiC layer structure were studied using electron microscopy. An intermediate layer is revealed between pores and unetched SiC which consists of a damaged region containing two-dimensional defects and a completely amorphous region. Energy-dispersive X-ray spectra measured within local (~3 nm) areas in various regions of the transverse sections of the structure studied showed that the intermediate layer is enriched with carbon in comparison to the stoichiometric substrate composition. The excess carbon content is retained in the layer of epitaxial SiC contacting the porous layer. © *2002 MAIK "Nauka/Interperiodica".*

The layers of porous silicon carbide (por-SiC), as well as the analogous layers of porous silicon, obtained by electrochemical etching of a massive single crystal is still a material of interest for the R&D of new semiconductor devices. This interest is related to the room-temperature photoluminescence (PL) from this material, the intensity of which is one to two orders of magnitude higher than the emission from the initial compact crystal in the same spectral range [1–3]. Attempts have been made to establish a relationship between the increased PL and structural features of the por-SiC layers. Konstantinov *et al.* [4] believed that this phenomenon is due to the defect centers formed as a result of the interaction of electrolyte with the SiC surface. Danishevskii *et al.* [5–7] suggested that it is a nanodimensional cubic carbide phase (3C-SiC) formed together with the porous layer which is responsible to a considerable extent for the enhanced emission from por-SiC. In particular, the results of transmission electron microscopy and cathodoluminescence measurements indicate [7] that the layer of 3C-SiC nanoparticles is buried at a certain depth rather than occurs at the surface of the porous layer (as was suggested for the PL-active layer in [4]). The additional interest in por-SiC layers is related to the possibility of growing perfect epitaxial layers on porous 6H-SiC substrates, since the etching treatment can be expected to decrease the concentration of defects capable of growing into the epitaxial layer and decreasing the structural perfection of the growing crystal [8].

In order to obtain new data on the structure of porous silicon carbide layers, we studied samples of this material by electron microscopy using EM 3000F and JEM 4000EXII instruments. The latter microscope is equipped with a special attachment containing an Si(Li) detector, which allows the energy-dispersive X-ray (EDX) spectra to be measured from local (~3 nm in diameter) areas of the sample surface.

The por-SiC layers were obtained on a part of a commercial 6H-SiC plate (Cree Corp., $N_d - N_a = 3 \times 10^{18}$ cm^{-3}) disoriented by 3.5° relative to the *c* axis. The working (0001)Si face of the plate was electrochemically polished, while the opposite side was mechanically ground. The anodic treatment was conducted for 20 min in an HF–H_2O–C_2H_5OH (1 : 1 : 2) electrolyte at a current density of 20 mA/cm^2 under UV illumination. The subsequent growth of thin (a few microns thick) epitaxial 6H-SiC films over the por-SiC layer was effected by sublimation in vacuum at 2000°C in a vertical water-cooled reactor [9]. It should be pointed out that the epitaxial growth under high-temperature conditions may be accompanied by modification of the por-SiC layer structure [10].

The results of electron-microscopic investigation showed that the structure of a por-SiC layer (with a thickness of ~35 μm obtained under the anodic treatment conditions employed) is inhomogeneous in depth. Projected onto the image plane, the pores observed at the substrate–porous layer (lower) interface appear as distorted triangles showing a tendency to align in zigzag chains along directions close to the normal in the basal (0001) plane. The bases of the triangles are parallel to the line of intersection of this (0001) plane with

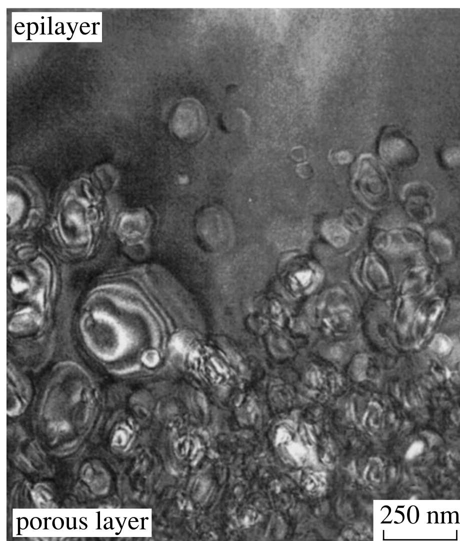

Fig. 1. Image of the transverse (11–20) cut showing the sample structure at the upper interface between the porous layer and the epitaxial layer.

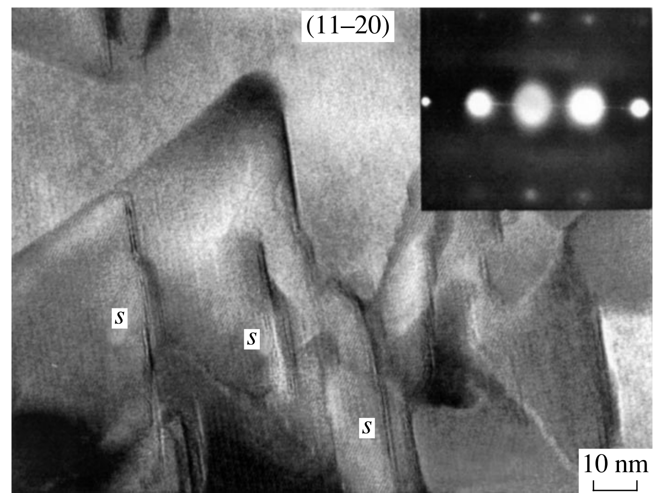

Fig. 2. Image of the transverse (11–20) cut showing the superposition of several triangular pores. The inset shows a microdiffraction pattern from the region *S* containing 2D defects.

the (11–20) projection plane. The vertices of the triangles point to the porous layer–epitaxial layer (upper) interface. The lower interface is rather sharp, with a deviation from plane parallel configuration not exceeding 30 nm over a boundary length of ~10 μm. On the average, the distance between the neighboring pores on the lower boundary of the porous layer equals the base of the triangles, which varies within 60–75 nm. The linear density of pores at the lower interface amounts to $\sim 1.5 \times 10^5$ cm^{-1}, from which the porosity can be estimated to not exceed 10%. Observed near the triangular etching patterns are so-called sleeves (120–150 nm long) extending in directions making an angle of 60° with the [0001] axis. The images obtained at a larger magnification reveal a stepped character of these sleeves, which is evidence that the etching patterns and their alignment are determined by the symmetry of the material.

The structure of a 1.5-μm-thick porous layer near the upper interface (Fig. 1) significantly differs from that observed at the lower boundary of the porous layer. The first point to be noted is that the upper interface is not as sharp as the lower one and is characterized by a greater scatter of pore dimensions (from 30 to 400 nm). Here, the pores have the shape of irregular hexagons, with one side parallel to the line of intersection of the (0001) plane with the (11–20) cut plane. The hexagons exhibit no clear tendency of alignment into chains. The images of large pores display interference (thickness) bands, which indicates that the pores possess a certain volume, rather than represent flat formations. The presence of large-size pores at the upper interface, which are larger than the average pores at the lower boundary of the porous layer, is probably explained by a polishing action of the sublimation etching process in the initial stage of the epitaxial growth: it was demonstrated in [10] that the epitaxial growth is preceded by a certain reduction (by a few microns) in the thickness of the porous layer.

Irrespective of the pore size, a region of increased dark contrast is observed at the interface between pores and the perfect layer at the site of intersection with the (0001) plane. At some points in this dark contrast region, the image reveals interference bands (Fig. 2). The corresponding microdiffraction patterns (see inset to Fig. 2) exhibit sharp intense bars connecting the primary beam trace to the (0002) reflections. These bars

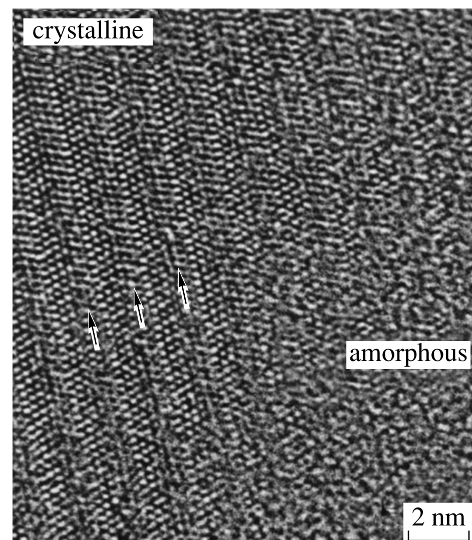

Fig. 3. High-resolution image of the transverse (11–20) cut showing the region of pores with an intermediate layer. The arrows indicate atomic rows with blurred contrast of separate atoms.

are oriented perpendicularly to the aforementioned boundary. An analysis of the images and the bar directions suggested that the latter are due to two-dimensional (2D) defects occurring in the basal (0001) planes perpendicular to the image plane.

High-resolution electron-microscopic images reveal an intermediate region between the perfect lattice of SiC and the pores (voids). This region features a gradual transition from the perfectly ordered to amorphous structure (Fig. 3). Figure 3 shows how the clear image of certain atomic plans loses sharpness, whereby separate "atoms" in these layers are not resolved. The diffuse character of the image of these planes is repeated with a period of several interplanar distances (with the planes sharply imaged separate atoms in between). Thus, we may suggest that violation of the image sharpness for certain atomic planes is related to the fact that these planes consist of atoms of a certain kind (Si or C).

In order to elucidate the nature of the amorphized region at the inner pore surface, we measured the local EDX spectra in various regions of the transverse sections of the samples studied: (i) in the substrate, at the lower interface, in the amorphous part of a pore, and between neighboring pores, and (ii) in the epitaxial layer, near the upper interface. Considering the EDX spectrum of the substrate (Fig. 4a) as a reference corresponding to stoichiometric SiC composition, an analysis of the aforementioned spectra indicated that the porous layer is enriched with carbon (Fig. 4b) as compared to the substrate. The maximum enrichment takes place in the amorphous region of the pore. The layer of epitaxial SiC adjacent to the porous material is also enriched with carbon (albeit to a lower extent than the porous layer proper), so that the epitaxial layer composition somewhat differs from stoichiometry.

The above results can be preliminarily interpreted as follows. Apparently, the electrochemical etching breaks the bonds between atoms of silicon carbide. The liberated atoms pass into the electrolyte. If the bonds between atoms of a certain kind are predominantly broken, the material will be enriched with atoms of another kind. Since the EDX spectra indicate that the porous SiC layer is enriched with carbon, we may conclude that etching predominantly breaks the bonds holding silicon atoms in the ordered state. When such bonds are broken, silicon atoms pass into the electrolyte. The regions exhibiting blurred images (Fig. 3) probably correspond to the positions of silicon atoms in the SiC structure of the (11-20) section studied.

As was established, the amorphized pore region exhibits a maximum deviation from SiC stoichiometry toward carbon enrichment. It is possible that, on reaching a critical deviation from stoichiometry and a certain fraction of broken bonds in the structure, the phase state of silicon carbide may be subject to instability, which leads to partial and, eventually, complete amorphization of such regions.

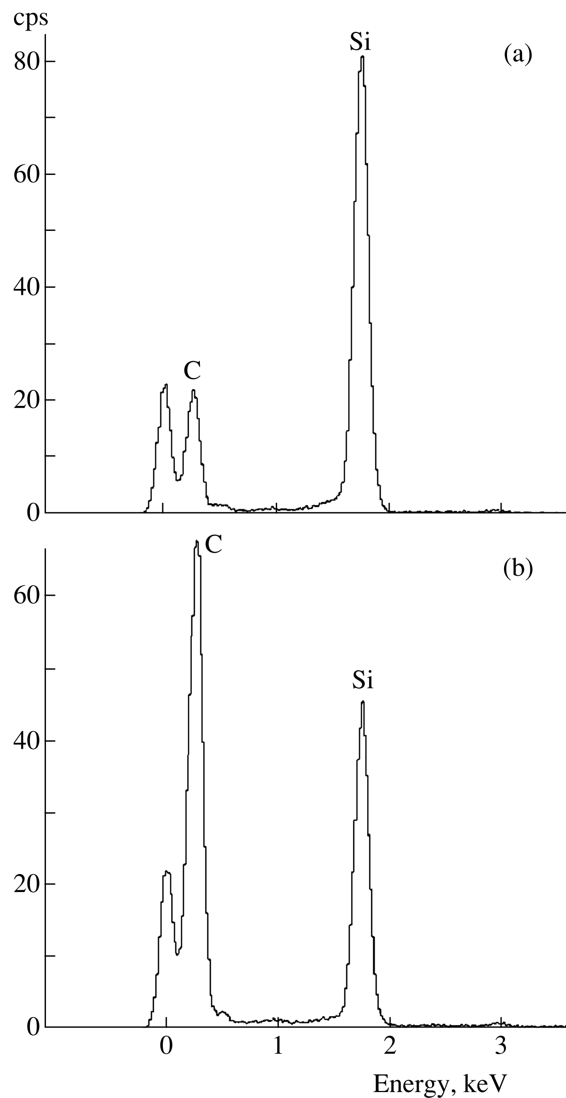

Fig. 4. EDX spectra of local (~3 nm) regions (a) in the substrate near the porous layer and (b) in the amorphous region of the porous layer.

The high-resolution images of the porous silicon carbide layer, as well as the corresponding microdiffraction patterns, did not exhibit any effects indicating the formation of disoriented nanodimensional particles. Nor did we observe 3C-SiC nanoparticles surrounded by the main (6H-SiC) material whose presence could be responsible for the increased PL activity. However, this can be related to the following. The breakage of interatomic bonds in the intermediate layer of porous silicon as a result of the interaction of electrolyte with 6H-SiC (indicated by certain features in the high-resolution images and EDX spectra) leads to distortion of the initial structure of the material. This process can be accompanied by the formation of new bonds with a coordination typical of the cubic SiC modification. Local regions with a cubic structure may be somewhat disoriented relative to each other. The {111} planes of

these nanoparticles can be ideally matched with the surrounding 6H-SiC at the {0001} planes. However, we failed to reveal such regions with sufficient reliability in this stage of the investigation. Evidently, a special processing of the high-resolution electron-microscopic images has to be developed for studying the nanodimensional particles.

Thus, our preliminary results neither revealed any growth defects in the epitaxial layer of silicon carbide nor showed the presence of dislocations or micropipes growing through the porous layer from the substrate. This result allows us to hope that porous silicon carbide layers on SiC substrates can be used as isomorphous buffer layers for the growth of epitaxial SiC layers more perfect as compared to the substrate while belonging to the same structural modification. Taking into account the absence of domestic 3C-SiC substrates of a large size, it is now even more interesting to obtain epitaxial layers of cubic SiC with a perfect crystal structure through sublimation epitaxy on a porous 6H-SiC substrate.

Acknowledgments. This study was supported by the Russian Foundation for Basic Research (project nos. 01-02-17907 and 01-02-17657) and by a grant from the Royal Society (London, UK).

REFERENCES

1. J. S. Shor, I. Grimberg, B. Z. Weiss, and B. D. Kutz, Appl. Phys. Lett. **62**, 2836 (1993).
2. T. Matsumoto, J. Takahashi, T. Tamaki, *et al.*, Appl. Phys. Lett. **64**, 226 (1994).
3. A. O. Konstantinov, C. L. Harris, and E. Jansen, Appl. Phys. Lett. **65**, 2699 (1994).
4. A. O. Konstantinov, A. Henry, C. I. Harris, and E. Jansen, Appl. Phys. Lett. **66** (17), 2250 (1995).
5. A. M. Danishevskii, V. B. Shuman, A. Yu. Rogachev, and P. A. Ivanov, Fiz. Tekh. Poluprovodn. (St. Petersburg) **29**, 2122 (1995) [Semiconductors **29**, 1106 (1995)].
6. A. M. Danishevskii, V. B. Shuman, A. Yu. Rogachev, *et al.*, Fiz. Tekh. Poluprovodn. (St. Petersburg) **30**, 1064 (1996) [Semiconductors **30**, 564 (1996)].
7. A. M. Danishevskii, M. V. Zamoryanskaya, A. A. Sitnikova, *et al.*, Semicond. Sci. Technol. **13**, 1111 (1998).
8. N. A. Mynbaeva, N. S. Savkina, A. Zubrilov, *et al.*, Mater. Res. Soc. Symp. Proc. **587**, 08.6.1. (2000).
9. N. S. Savkina, A. A. Lebedev, D. V. Davydov, *et al.*, Mater. Sci. Eng. **61**–**62**, 165 (1999).
10. N. S. Savkina, V. V. Ratnikov, and V. B. Shuman, Fiz. Tekh. Poluprovodn. (St. Petersburg) **35** (2), 159 (2001) [Semiconductors **35**, 153 (2001)].

Translated by P. Pozdeev

Technical Physics Letters, Vol. 28, No. 11, 2002, pp. 939–941. Translated from Pis'ma v Zhurnal Tekhnicheskoĭ Fiziki, Vol. 28, No. 22, 2002, pp. 32–38.
Original Russian Text Copyright © 2002 by Emel'yanov.

Features of the Relaxation Polarization of a Polar Dielectric under Conditions of Large Electrothermal Loads

O. A. Emel'yanov
St. Petersburg State Technical University, St. Petersburg, Russia
e-mail: eicc@phtf.stu.neva.ru
Received April 25, 2002

Abstract—In a polar dielectric occurring under the conditions of large electrothermal loads, it is necessary to take into account the temperature dependence of the conductivity $\gamma(T)$ and complex permittivity $\dot{\varepsilon}(T)$. An allowance for this circumstance in the simplest model of the Debye relaxation polarization leads to deviation of the $\varepsilon'' = f(\varepsilon')$ curve from the well-known Cole–Cole semicircle. Exact solutions of the model problems for a flat capacitor are presented for the cases when the temperature gradient is caused by an external source and by relaxation losses in the dielectric material. *© 2002 MAIK "Nauka/Interperiodica".*

When dielectrics and related electric capacitors are employed under the conditions of large electrothermal loads, the materials are subject to considerable temperature gradients. In such cases, the dielectric medium becomes essentially inhomogeneous because of the temperature dependence of important physical parameters, including the conductivity γ and complex permittivity $\dot{\varepsilon} = \varepsilon' - i\varepsilon''$, where ε' and ε'' are the real and imaginary parts of the complex quantity.

Allowance for the inhomogeneous distribution of $\gamma(T)$ in the regions of large temperature gradients may lead to a number of interesting kinetic phenomena:

(i) A frequency–field dependence of the dielectric characteristics caused by the migration polarization.

(ii) The appearance of a spectrum of the relaxation times outside the region of dispersion of the permittivity.

(iii) The appearance of nonlinear current–voltage (I–U) and capacitance–voltage (C–U) characteristics [1].

At the same time, allowing for the temperature dependence of $\varepsilon'(T)$ and $\varepsilon''(T)$ can also be significant for evaluation of the working regimes of capacitors based on polar dielectrics possessing a maximum in $\varepsilon''(T)$ [2]. This is especially important if the temperature gradients are caused by dielectric losses of the relaxation time while the conductivity losses can be ignored.

Consider a model flat capacitor with a dielectric layer thickness $2h$ and a voltage $\dot{u}(t) = U_0 e^{i\omega t}$ applied to the electrodes. In the general case, the parameters ε', ε'', and γ are functions of the coordinate x because of the temperature variation $T(x)$. The temperature gradient can result from external sources of heat and/or dielectric losses in the capacitor material. The total current j_t through the dielectric is a sum of the conduction (j_1) and displacement (j_2) components:

$$j_t = j_1 + j_2 = \gamma(T(x))E(T(x)) + \frac{\partial D(T(x))}{\partial t}, \quad (1)$$

where E and D are complex vectors of the electric field strength and induction; the complex current is $j_t = j_3 e^{i\omega t}$, where j_3 is the complex amplitude.

According to the total current law [3], the complex amplitude obeys the relation

$$\operatorname{div} j_3 = 0. \quad (2)$$

Taking into account the relations $D = \varepsilon E$ and $E = -\operatorname{grad} u(t)$ and the known temperature field $T(x)$, one can solve Eqs. (1)–(2) and determine the effective values of $\varepsilon'_{\text{eff}}$ and $\varepsilon''_{\text{eff}}$ for the given capacitor, which, generally speaking, must differ from the corresponding local characteristics of the dielectric, since the latter are inhomogeneously distributed as a result of the temperature gradient existing in the dielectric layer. In the simplest case, the character of the temperature field can be determined upon solving the corresponding first boundary problem of the quasi-stationary thermal conductivity:

$$\lambda \frac{d^2 T}{dx^2} + q_v(T(x)) = 0, \qquad T(-h) = T_1, \quad T(h) = T_2, \quad (3)$$

where λ is the thermal conductivity coefficient; T_1 and T_2 are the temperatures on the left- and right-hand dielectric boundaries, respectively; $q_v(T(x)) = \frac{1}{2}\operatorname{Re}\{j_3 \dot{E}\}$ is the volume density of heat evolution; and

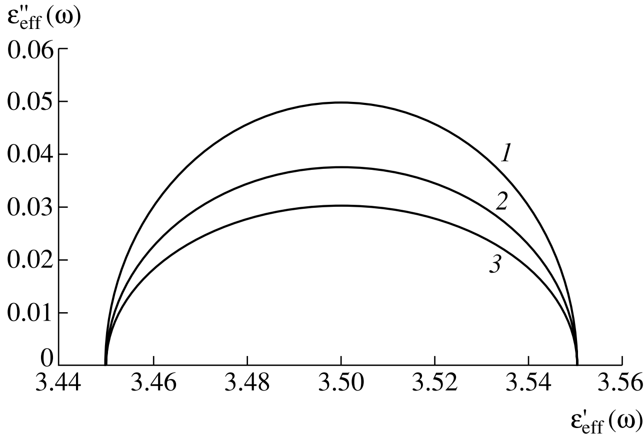

Fig. 1. The plots of $\varepsilon''_{\text{eff}} = f(\varepsilon'_{\text{eff}})$ constructed for various temperature differences T_m caused by an external heat source (K): (*1*) 0, (*2*) 100, and (*3*) 150.

$\dot{E}$ is the complex-conjugate amplitude of the electric field strength.

Thus, Eqs. (1)–(3) represent a mixed electrothermal problem for the state of a dielectric in a variable electric field, the inhomogeneity of which is related to the temperature variation $T(x)$. The effective quantities $\varepsilon''_{\text{eff}}$ and $\varepsilon'_{\text{eff}}$ and the loss tangent $\tan\delta_{\text{eff}} = \varepsilon''_{\text{eff}}/\varepsilon'_{\text{eff}}$ obey the following relations:

$$\gamma_a(x) = \omega\varepsilon''(x) + \gamma(x), \quad \gamma_r(x) = \omega\varepsilon'(x),$$

$$z_{as} = \int_{-h}^{h} \frac{\gamma_a(x)dx}{\gamma_a(x)^2 + \gamma_r(x)^2},$$

$$z_{rs} = \int_{-h}^{h} \frac{\gamma_r(x)dx}{\gamma_a(x)^2 + \gamma_r(x)^2}, \quad z_s^2 = z_{as}^2 + z_{rs}^2, \tag{4}$$

$$\varepsilon''_{\text{eff}} = \frac{2L}{\omega}\frac{z_{as}}{z_s^2}, \quad \varepsilon'_{eff} = \frac{2L}{\omega}\frac{z_{rs}}{z_s^2}, \quad \tan\delta_{\text{eff}} = \frac{z_{as}}{r_{rs}}.$$

In the case when the parameters ε', ε'', and γ are temperature independent, Eqs. (4) readily convert into the well-known relations for a homogeneous dielectric medium: $\varepsilon''_{\text{eff}} = \gamma/\omega + \varepsilon''$ and $\varepsilon'_{\text{eff}} = \varepsilon'$. In the most general case, $\varepsilon''_{\text{eff}} = \varepsilon''_{\text{eff}}(\omega, T)$ and $\varepsilon'_{\text{eff}} = \varepsilon'_{\text{eff}}(\omega, T)$. It would be of interest to make allowance for these dispersion relations in the case of a dielectric whose relaxation polarization is described by the simplest (Debye) model. In this case, the relation between ε'' and ε' is conveniently described by the well-known Cole–Cole diagram in the (ε''(ω), ε'(ω)) coordinates, representing a semicircle with the radius $(\varepsilon_s - \varepsilon_\infty)/2$, where ε_s and ε_∞ are the so-called static and optical permittivities. Let us consider these two cases separately.

1. Temperature gradient caused by external heat sources. In this case, the volume heat evolution term $q_v = \omega\varepsilon_0\varepsilon''E^2$ can be omitted to simplify Eq. (3), while the boundary conditions determine the temperature field gradient: $\text{grad}T(x) = T_m/2h$ for $T(h) = T_m$ and $T(-h) = 0$. This gradient can be due to an external thermal flux $q_s = -\lambda\,\text{grad}T(x)$. For the quantities z_{as} and z_{rs}, exact solution of the problem yields

$$z_{as}(\omega) = \frac{L}{\omega g}\frac{(\varepsilon_s - \varepsilon_\infty)}{p\varepsilon_0\varepsilon_c}\left[\arctan\frac{\tau_0}{a} - \arctan\frac{\tau_m}{a}\right],$$

$$z_{rs}(\omega) = \frac{2L}{\omega\varepsilon_s} + \frac{L(\varepsilon_s - \varepsilon_\infty)}{2\omega g p\varepsilon_0\varepsilon_s}\ln\left(\frac{a^2 + \tau_0^2}{a^2 + \tau_m^2}\right), \tag{5}$$

$$a = \frac{\varepsilon_s}{\varepsilon_\infty\omega}; \quad g = \frac{T_m}{2}; \quad \tau \approx \tau_0 e^{-pT}, \quad p = \frac{W}{kT_g^2},$$

where T_g is the temperature of the maximum in $\varepsilon''(T)$ and $\tau_m = \tau_0 e^{-pT_m}$.

Using formulas (5), general equations (4), and the Debye relations for a local point in the medium [4],

$$\varepsilon'(\omega) = \frac{\varepsilon_s + \varepsilon_\infty\omega^2\tau^2}{1 + \omega^2\tau^2}, \quad \varepsilon''(\omega) = \frac{(\varepsilon_s - \varepsilon_\infty)\omega\tau}{1 + \omega^2\tau^2}, \tag{6}$$

we determined the relations $\varepsilon''_{\text{eff}} = f(\varepsilon'_{\text{eff}})$, which are constructed in Fig. 1 for various T_m. As can be seen, the deviation of the curves from a semicircle at a small temperature gradient (small T_m) is insignificant. As the temperature gradient increases, the $\varepsilon''_{\text{eff}} = f(\varepsilon'_{\text{eff}})$ curve strongly deviates from the Cole–Cole semicircle corresponding the simple Debye model (6).

2. Temperature gradient caused by relaxation losses. In this case, the temperature T_m at the center of the dielectric layer becomes a parameter of the problem, which depends on the conditions of cooling at the capacitor boundaries, as well as on the frequency ω, the current density j_m, the thermal conductivity λ, and the half-layer thickness h.

The exact expressions for z_{as} and z_{rs} are as follows:

$$z_{as}(\omega) = 2L\sqrt{\frac{2}{\beta_m(\omega)\omega}}mI_0(\omega),$$

$$z_{rs}(\omega) = z_{as}(\omega)\frac{\varepsilon_s + \varepsilon_\infty\omega^2\tau_0^2}{(\varepsilon_s - \varepsilon_\infty)\omega\tau_0}$$

$$+ 2L\sqrt{\frac{2}{\beta_m(\omega)\omega}}m(\alpha I_1(\omega) - \beta I_2(\omega)),$$

$$\beta_m(\omega) = \frac{j^2(\omega)h^2}{2\lambda},$$

$$j(\omega) = \frac{\sqrt{\lambda}}{h}[I_3(\omega) + 2\sqrt{\omega}m(\varepsilon_\infty \alpha I_1(\omega) - \varepsilon_s \beta I_2(\omega))], \quad (7)$$

$$I_3(\omega) = 2m\sqrt{\omega}I_0(\omega)\frac{\varepsilon_s^2 + \varepsilon_\infty^2\omega^2\tau_0^2}{(\varepsilon_s - \varepsilon_\infty)\omega\tau_0},$$

$$I_0(\omega) = \sqrt{\arctan\frac{\tau_0}{a} - \arctan\frac{\tau_m}{a}},$$

$$I_1(\omega) = \int_{\tau_0}^{\tau_m} \sqrt{\arctan\frac{x}{a} - \arctan\frac{\tau_m}{a}}\,dx,$$

$$I_2(\omega) = \int_{\tau_0}^{\tau_m} \sqrt{\arctan\frac{x}{a} - \arctan\frac{\tau_m}{a}}\,\frac{1}{x^2}\,dx,$$

where $\beta_m(\omega)$ is the load parameter; α, β, and m are coefficients given by the formulas

$$\alpha = \frac{\varepsilon_\infty \omega}{\varepsilon_s - \varepsilon_\infty}, \quad \beta = \frac{\varepsilon_s}{(\varepsilon_s - \varepsilon_\infty)\omega}, \quad m = \sqrt{\frac{\varepsilon_s - \varepsilon_\infty}{\rho \varepsilon_\infty \varepsilon_s}};$$

and the quantities τ_0, τ_m, and a are the same as in Eqs. (5).

Figure 2 presents the plots of $\varepsilon''_{\text{eff}} = f(\varepsilon'_{\text{eff}})$ constructed for various loads β_m corresponding to different temperature differences T_m between the center and boundaries of the dielectric. Similarly to the first case, the $\varepsilon''_{\text{eff}} = f(\varepsilon'_{\text{eff}})$ curve more significantly deviates from a semicircle with increasing load $\beta_m(\omega)$. In both cases, the deviation is caused by the presence of a temperature gradient in the dielectric, which is characterized by the same relaxation process according to the Debye model. This circumstance can be formally interpreted as the appearance of a spectrum of the relaxation times, although the difference is entirely due to the internal temperature-induced inhomogeneity in distribution of the field and the main dielectric parameters ε' and ε''.

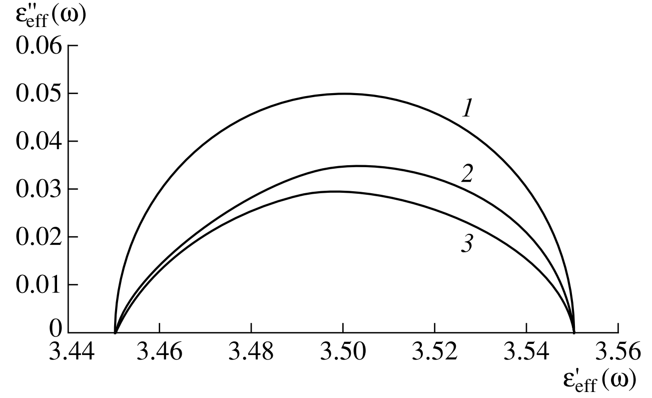

Fig. 2. The plots of $\varepsilon''_{\text{eff}} = f(\varepsilon'_{\text{eff}})$ constructed for various temperature differences T_m caused by internal relaxation losses (K): (*1*) 0, (*2*) 100, and (*3*) 150.

The maximum value of ε''_{eff}, which determines the tolerable level of electrothermal load, is lower than the intrinsic $\varepsilon''_{\max}$ of the medium and shifts leftward on the frequency scale with increasing load parameter $\beta_m(\omega)$, which has to be taken into account in evaluating the working properties of capacitors operating in such regimes.

REFERENCES

1. V. V. Kharitonov and É. I. Ermolina, Fiz. Tverd. Tela (Leningrad) **29** (4), 977 (1987) [Sov. Phys. Solid State **29**, 560 (1987)].
2. O. A. Emel'yanov, Pis'ma Zh. Tekh. Fiz. **27** (16), 32 (2001) [Tech. Phys. Lett. **27**, 679 (2001)].
3. L. D. Landau and E. M. Lifshitz, *Electrodynamics of Continuous Media* (Gostekhizdat, Moscow, 1957; Pergamon, Oxford, 1960).
4. B. I. Sazhin, *Electrical Properties of Polymers* (Khimiya, Leningrad, 1985).

Translated by P. Pozdeev

Technical Physics Letters, Vol. 28, No. 11, 2002, pp. 942–944. Translated from Pis'ma v Zhurnal Tekhnicheskoĭ Fiziki, Vol. 28, No. 22, 2002, pp. 39–44.
Original Russian Text Copyright © 2002 by Abdullaev, Navotny.

Dispersion-Managed Soliton Propagation in Optic Fibers with Random Dispersion

F. Kh. Abdullaev and D. V. Navotny

Physicotechnical Institute, Academy of Sciences of the Republic of Uzbekistan, Tashkent, Uzbekistan

e-mail: fatkh@uzsci.net; denis@uzsci.net

Received March 5, 2002

Abstract—Propagation of dispersion-managed solitons in optic fibers with randomly distributed dispersion is studied. It is shown that the effect of the dispersion fluctuations can be described within the framework of a modified nonlinear Schrödinger equation with a frequency-dependent damping term ($\sim\omega^4$). The presence of randomly modulated dispersion leads to the damping of optical pulses. The condition for stable pulse propagation is determined based on the corresponding variational equations. *© 2002 MAIK "Nauka/Interperiodica".*

The use of dispersion-managed solitons (DMSs) as data carriers is a key concept underlying the creation of high-speed optical communication lines [1, 2]. The difference between a DMS and a usual soliton consists in that the former periodically changes shape while propagating in an optic fiber with alternating normal and anomalous dispersion regions. However, recent experiments involving precise measurements of the dispersion in optical fibers have shown that this parameter varies in a random manner along the fiber length [3], which can lead to DMS breakage.

Previously, a model in which the lengths of normal and anomalous dispersion regions varied in a random manner was studied within the framework of a variational approach [4, 5]. However, the disadvantage of that model was that the damping due to radiation losses was not taken into consideration. Kath and Smyth [6] derived variational equations for the homogeneous nonlinear Schrödinger equation (NSE) with allowance for the radiation damping. Below, we consider the problem of DMS propagation in an optic fiber with randomly distributed dispersion under linear and nonlinear amplification conditions.

As is known, the propagation of optical pulses in dispersion-managed systems is adequately described by an NSE with a periodically varying dispersion term,

$$iu_z + \frac{d(z)}{2}u_{tt} + |u|^2u = i\delta u + i\mu|u|^2u, \qquad (1)$$

where u is a dimensionless envelope of the electric field in the light wave; δ and μ are the linear and nonlinear amplification coefficients, respectively; and $d(z)$ is the dispersion profile of the optic fiber. In the presence of dispersion fluctuations, the $d(z)$ function can be presented as a sum of periodic and random components,

$$d(z) = d_0(z) + \epsilon(z), \quad \langle\epsilon\rangle = 0,$$
$$\langle\epsilon(z)\epsilon(z')\rangle = B(z-z', l_c)_{l_c\to 0} \longrightarrow \sigma^2\delta(z-z'),$$

where $\epsilon(z)$ is assumed to be a random Gauss process with $\sigma^2 = \Delta D l_c$, $\Delta D = D_1 - D_2$, and l_c is the correlation length. We will also assume that the magnitude of noise is small as compared to that of the periodic dispersion term. According to experimental data, l_c is usually on the order of several meters and, hence, is much smaller as compared to all characteristic lengths (which are typically on the order of several tens of kilometers). Therefore, the $\varepsilon(z)$ random process can be considered as white noise.

In order to describe the influence of the dispersion fluctuations, let us treat Eq. (1) using to the method of a mean field. According to this method, the total field is represented as the sum of a slowly varying mean field $\langle u\rangle$ and a weak fluctuating component δu:

$$u = \langle u\rangle + \delta u, \quad \langle\delta u\rangle = 0, \quad \delta u \ll \langle u\rangle.$$

Within the framework of this approach, we assume that $\langle|u|^2u\rangle \approx |\langle u\rangle|^2\langle u\rangle$, which implies the neglect of nonlinear fluctuations. In order to separate the average $\langle\epsilon(z)u_{tt}\rangle$, we use the Furutsu–Novikov formula [7]

$$\langle\epsilon(z)F(u)\rangle = \int_0^z B(z-z')\left\langle\frac{\delta F(u)}{\delta\epsilon(z')}\right\rangle dz'. \qquad (2)$$

After this averaging, Eq. (1) acquires the following form (for simplicity, we omit the angular brackets):

$$iu_z + \frac{d_0(z)}{2}u_{tt} + |u|^2u = i\delta u - i\gamma u_{tttt} + i\mu|u|^2u, \qquad (3)$$

where $\gamma = \sigma^2/4$ and σ is the noise strength. As can be seen, the resulting equation is of the NSE type with an additional term proportional to the fourth-order derivative in the right-hand part. This implies that the effect of random dispersion on the evolution of an optical pulse is described as pulse propagation in a periodically-inhomogeneous medium with frequency-dependent damping.

Gabitov and Turitsyn [2] demonstrated that the DMS dynamics in conservative systems is well described within the framework of a variational approximation. In the presence of nonconservative terms in Eq. (3), we can use a modified variational approach. In this case, the Euler–Lagrange equation can be written in the following form [8]:

$$\frac{\partial \bar{L}}{\partial \eta_i} - \frac{d}{dz}\frac{\partial \bar{L}}{\partial \eta_{iz}} = \int_{-\infty}^{\infty}\left(R\frac{\partial u^*}{\partial \eta_i} + c.c.\right), \quad (4)$$

where $\bar{L} = \int L(z, t)dt$ is the average Lagrangian and R is the perturbation operator. Taking the trial function in the form of a Gauss pulse,

$$u(z, t) = A(z)\exp\left[-\frac{t^2}{2a(z)^2} + i\frac{b(z)t^2}{2} + i\phi(z)\right],$$

where $A(z)$, $a(z)$, $b(z)$, and $\phi(z)$ are the amplitude, width, chirp, and linear phase of the pulse, respectively, we obtain from Eqs. (3) and (4) the following system of equations for the DMS parameters:

$$\begin{aligned}(a^2)_z &= 2d_0(z)a^2b - \frac{5}{2\sqrt{2}}\mu A^2a^2 + 6\gamma a^2\left[\frac{1}{a^4} - b^4a^4\right],\\ (A^2)_z &= -d_0(z)A^2b + \frac{7}{2}\delta A^2 + \frac{13}{4\sqrt{2}}\mu A^4\\ &\quad - \frac{3}{2}\gamma A^2\left[\frac{3}{a^4} + 2b^2 - b^4a^4\right],\\ b_z &= \frac{d_0(z)}{a^4} - d_0(z)b^2 - \frac{A^2}{\sqrt{2}a^2} - 12\gamma b\left(\frac{1}{a^4} + b^2\right).\end{aligned} \quad (5)$$

Here, the equation for ϕ is omitted because it separates from the system of Eqs. (5). In the case of $\gamma = \delta = \mu = 0$, system (5) reproduces the known variational equations for the DMS parameters [2].

Let us find fixed points of the system under consideration which correspond to stable DMS propagation in the presence of random fluctuations of the dispersion map coefficients. Equating the left parts of Eqs. (5) to zero and assuming that $b \sim \delta, \mu, \gamma \ll 1$ and $a \sim 0$, we obtain

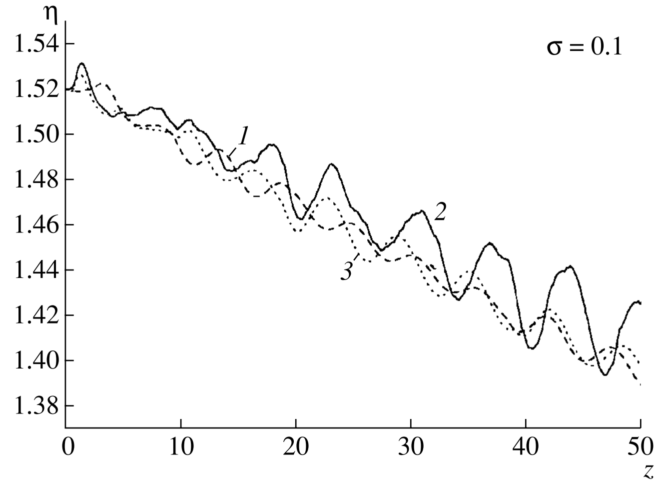

Fig. 1. A comparison of numerical solutions to the averaged NSE (3) (curve *1*), system (5) (curve *2*), and complete NSE (1) (curve *3*).

$$a_0^2 = \frac{\sqrt{2}d_0}{A_0^2}, \quad (6)$$

$$A_0^2 = \frac{2\sqrt{2}\mu d_0^2}{3\gamma}\left(1 \pm \sqrt{1 + \frac{21\delta\gamma}{4\mu^2 d_0^2}}\right), \quad (7)$$

$$b_0 = \frac{1}{2d_0}\left(\frac{5\mu A_0^2}{2\sqrt{2}} - \frac{6\gamma}{a_0^4}\right). \quad (8)$$

According to relation (6), stable DMS propagation in an optical fiber with random dispersion is possible only in the region of normal residual dispersion ($d_0 > 0$). This prediction is confirmed by the results of numerical modeling (see [5]).

We performed numerical modeling of the variational equations (5) and the complete NSE (1) for a system with the following parameters: nonlinear refractive index of the fiber, $n_2 = 3.2 \times 10^{-20}$ m^2/W; effective cross section area of the fiber, $A_{\text{eff}} = 50$ μm^2; wavelength, $\lambda_0 =$ 1.55 μm; anomalous dispersion $D_1 = 3$ ps/(nm km); normal dispersion, $D_2 = -2.8$ ps/(nm km); normal and anomalous dispersion segment length, $Z_1 = Z_2 = 79$ km; and the correlation length, $l_c = 3$ m. In dimensionless variables, the dispersion map coefficients are $d_1 = 30$, $d_2 = -28$, and $z_1 = z_2 = 0.078$.

Let us compare the numerical results obtained using the variational equations for DMS parameters (5), the complete NSE (1), and the averaged Eq. (3) presented in Fig. 1. As can be seen from these data, the three

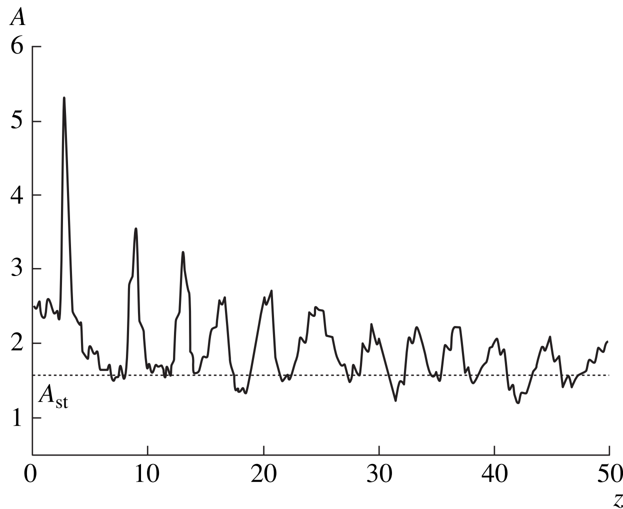

Fig. 2. Transition to a stable pulse propagation regime as described by a solution to system (5); A_{st} is the stationary solution.

curves are in good agreement, which confirms the validity of the proposed approach.

Figure 2 shows the behavior of the amplitude according to Eq. (3) for $\delta = 0.001$, $\mu = -0.001$, $\sigma = 0.1$, and $d_0 = 30$. As can be seen, the amplitude tends to a stationary point which can be calculated using Eqs. (6)–(8). We failed to achieve a fully stable DMS propagation because of the presence of random perturbations (6)–(8). In order to provide for stable DMS propagation, it might be useful to employ a filter with saturated absorption, which would suppress the non-soliton part of the optical signal [9, 10].

REFERENCES

1. F. M. Knox, N. J. Doran, K. J. Blow, *et al.*, Electron. Lett. **32**, 54 (1996).
2. I. Gabitov and S. Turitsyn, Opt. Lett. **21**, 327 (1996).
3. L. F. Mollenauer, P. V. Mamyshev, and M. J. Neubelt, Opt. Lett. **21**, 1724 (1996).
4. F. Kh. Abdullaev and B. B. Baizakov, Opt. Lett. **25**, 93 (2000).
5. B. A. Malomed and A. Berntson, J. Opt. Soc. Am. B **18** (9), 1243 (2001).
6. W. I. Kath and N. Smyth, Phys. Rev. E **51**, 1484 (1995).
7. I. V. Klyatskin, *Stochastic Equations and Waves in Randomly-Inhomogeneous Media* (Nauka, Moscow, 1980).
8. A. Maĭmistov, Zh. Éksp. Teor. Fiz. **104**, 3620 (1993) [JETP **77**, 727 (1993)].
9. S. Turitsyn, Phys. Rev. B **54**, R3125 (1996).
10. L. Richardson, K. Blow, and V. K. Mezentsev, in *Nonlinear Guided Waves and Their Applications* (Optical Society of America, Washington, 2001), p. 352.

Translated by P. Pozdeev

Technical Physics Letters, Vol. 28, No. 11, 2002, pp. 945–948. Translated from Pis'ma v Zhurnal Tekhnicheskoĭ Fiziki, Vol. 28, No. 22, 2002, pp. 45–51.
Original Russian Text Copyright © 2002 by Shiryaeva, Belonozhko, Grigor'ev.

On the Conditions for Realization of Nonlinear Resonance in an Oscillating Charged Drop

S. O. Shiryaeva, D. F. Belonozhko, and A. I. Grigor'ev
Yaroslavl State University, Yaroslavl, Russia
e-mail: shir@uniyar.ac.ru
Received May 24, 2002

Abstract—Nonlinear oscillations of a charged drop upon the initial deformation of the equilibrium spherical shape representing a superposition of several modes are studied. A condition for the excitation mode frequencies is established under which a resonance interaction of the oscillation modes in the drop takes place. For a drop charged below the critical level for realization of the instability with respect to the intrinsic charge, there is a large number of resonance conditions rather than a single situation, as known previously. © *2002 MAIK "Nauka/Interperiodica".*

Introduction. Investigation of the nonlinear interaction of modes in oscillating charged drops is of interest from the standpoint of many basic and applied problems involving such objects. An original study of the nonlinear capillary oscillations of a drop charged below the critical level from the standpoint of the surface stability [1] showed that, in the second order of smallness with respect to the small initial single-mode perturbation, there is an internal nonlinear resonance between the fourth and sixth modes provided that the mode frequencies obey the condition $\omega_6^2 = 4\omega_4^2$. No other resonances were found in a drop charged below the critical level [1].

Previously [2], we studied a more general situation in which the initial perturbation of the drop surface represented a superposition of two modes and established that the resonance found in [1] possesses an asymmetric character: a resonance of the fourth mode can take place only upon simultaneous initial excitation of the fourth and sixth modes, while a resonance of the sixth mode can be induced by the initial excitation of the fourth mode alone. Thus, in the case when the initial deformation of the equilibrium spherical shape represents a superposition of several modes rather than a single mode, the resonance frequency relation obtained in [1] should be replaced by a more general condition which would take into account the triple mode interactions as well. This generalization may reveal additional resonance situations in a drop possessing a subcritical charge. It should be noted that the resonance energy exchange between modes may also lead to a change in the critical conditions determining the development of the drop instability with respect to the intrinsic charge (the instability onset level may decrease as compared to that predicted from linear theory). For these reasons, determination and investigation of the possible resonance mode interactions in this system is of considerable importance.

Formulation of the problem. Let us consider the time evolution of the surface of a drop of the ideal incompressible conducting liquid with a density ρ and surface tension σ. The drop, bearing a total charge of Q and having a volume equal to that of a sphere with radius R, occurs in vacuum. At the initial time instant $t = 0$, the equilibrium spherical shape of the drop is subject to a virtual axisymmetric perturbation of a certain finite amplitude. The task is to determine the spectrum of capillary oscillations of the drop (i.e., the drop shape) in the subsequent moments of time ($t > 0$).

Let an equation describing the drop surface in a spherical coordinate system with the origin placed at the center of mass be written in the following form: $r(\theta, t) = 1 + \xi(\theta, t)$, where $|\xi| \ll 1$. In the dimensionless variables such that $R = \rho = \sigma = 1$, the problem of evolution of the drop surface is mathematically formulated as follows:

$$\Delta\psi(\mathbf{r}, t) = 0; \quad \Delta\Phi(\mathbf{r}, t) = 0;$$

$$r \longrightarrow 0: \psi(\mathbf{r}, t) \longrightarrow 0; \quad r \longrightarrow \infty: \Phi(\mathbf{r}, t) \longrightarrow 0;$$

$$r = 1 + \xi(\theta, t): \frac{\partial\xi}{\partial t} = \frac{\partial\psi}{\partial r} - \frac{1}{r^2}\frac{\partial\xi}{\partial\theta}\frac{\partial\psi}{\partial\theta};$$

$$\Delta p - \frac{\partial\psi}{\partial t} - \frac{1}{2}(\nabla\psi)^2 + \frac{1}{8\pi}(\nabla\Phi)^2 = \operatorname{div}\mathbf{n};$$

$$\Phi(\mathbf{r}, \theta, t) = \Phi_s(t).$$

To close the above system, we use the conditions of conservation of the total charge Q and the drop volume,

as well as the condition of immobility of the center of mass:

$$-\frac{1}{4\pi}\oint_S(\mathbf{n}\cdot\nabla\Phi)ds = Q,$$

$$S = [r = 1+\xi(\theta,t),\ 0\le\theta\le\pi,\ 0\le\phi\le 2\pi],$$

$$\int_V r^2 dr\sin\theta d\theta d\phi = \frac{4}{3}\pi,$$

$$V = [0\le r\le 1+\xi(\theta,t),\ 0\le\theta\le\pi,\ 0\le\phi\le 2\pi],$$

$$\int_V \mathbf{e}_r\cdot r^3 dr\sin\theta d\theta d\phi = 0.$$

The initial conditions specify a virtual deformation of the equilibrium spherical drop, with zero initial velocities of all points of the drop surface:

$$t = 0: \xi(\theta) = \xi_0 P_0(\mu)+\xi_1 P_1(\mu)+\varepsilon\sum_{1\in\Xi}h_i P_i(\mu);$$

$$\sum_{i\in\Xi}h_i = 1;\quad \frac{\partial\xi(\theta,t)}{\partial t} = 0.$$

In the above relationships, Ξ is the set of numbers of the initially excited modes; $\mu\equiv\cos\theta$; Δp is the constant pressure jump between the inside and outside of the drop in the equilibrium state; $\mathbf{n}$ is the unit vector of the normal to the drop surface; $\mathbf{e}_r$ is the radial unit vector of the spherical coordinate system; $\Phi(\mathbf{r},t)$ and $\psi(\mathbf{r},t)$ are the potentials of the electric and velocity fields, respectively; $\Phi_s(t)$ is the constant electric potential on the drop surface; ε is the amplitude of the initial perturbation of the drop surface; $P_i(\mu)$ is the Legendre polynomial of the ith order; h_i are coefficients determining the partial contributions of the ith oscillation mode to the total initial perturbation; and ξ_0 and ξ_1 are constants determined from the conditions of the constant drop volume and the center-of-mass immobility at the initial instant of time.

Problem solution and discussion. The above problem can be solved using the asymptotic multiscale method, which yields the following expression describing the time variation of the droplet shape:

$$r(\theta,t)1+\varepsilon\left\{\sum_{i\in\Xi}M_i^{(1)}(t)P_i(\mu)\right\}+\varepsilon^2\left\{\sum_{n=0}^{\infty}M_n^{(2)}(t)P_n(\mu)\right\}+O(\varepsilon^3);\qquad(1)$$

$$M_i^{(1)}(t) = h_i\cos(\omega_i t);$$

$$M_0^{(2)})(t) = -\frac{1}{2}\sum_{i\in\Xi}\frac{h_i}{(2i+1)}(1+\cos(2\omega_i t));$$

$$M_1^{(2)}(t) = -\sum_{i\in\Xi}\frac{9ih_{i-1}h_i}{(2i-1)(2i+1)}\cos(\omega_i t)\cos(\omega_{i-1}t);$$

$$M_n^{(2)}(t) = [N_n(t)-N_n(0)\cos(\omega_n t)];\quad n\ge 2;$$

$$N_n(t) = \frac{1}{2}\sum_{i\in\Xi}\sum_{j\in\Xi}h_i h_j\{\lambda_{ijn}^{(+)}\cos((\omega_i+\omega_j)t)+\lambda_{ijn}^{(-)}\cos((\omega_i-\omega_j)t)\};$$

$$\omega_n^2\equiv n(n-1)[(n+2)-W];\quad W = \frac{Q^2}{4\pi};$$

$$\lambda_{ijn}^{(\pm)}\equiv[\gamma_{ijn}\pm\omega_i\omega_j\eta_{ijn}][\omega_n^2-(\omega_i\pm\omega_j)^2]^{-1};$$

$$\gamma_{ijn}\equiv K_{ijn}[\omega_i^2(n-i+1)+2n[j(j+1)-1]+[j(i+1)-i(2i-2n+7)+3]n\frac{W}{2}\Big]+\alpha_{ijn}\left[\frac{1}{i}\omega_i^2+n\frac{W}{2}\right];$$

$$\eta_{ijn}\equiv K_{ijn}\left(\frac{n}{2}-i+1\right)+\alpha_{ijn}\frac{1}{i}\left(1+\frac{n}{2j}\right);$$

$$K_{ijn}\equiv[C_{i0j0}^{n0}]^2;\quad \alpha_{ijn}\equiv-\sqrt{i(i+1)j(j+1)}C_{i0j0}^{n0}C_{i(-1)j1}^{n0};$$

$$C_{i0j0}^{n0} \equiv \begin{cases} 0, \quad \text{if} \quad i+j+n = 2g+1 \ (\text{where } g \text{ is integer}); \\ \dfrac{(-1)^{g-n}\sqrt{2n+1}g!}{(g-i)!(g-j)!(g-n)!}\left[\dfrac{(2g-2i)!(2g-2j)!(2g-2n)!}{(2g+1)!}\right]^{1/2}, \text{ if } i+j+n = 2g; \end{cases}$$

$$C_{i(-1)j1}^{n0} \equiv \sqrt{2n+1}n!\left[\frac{(i+j-n)!i(i+1)}{(n+i-j)!(n-i+j)!(i+j+n+1)!j(j+1)}\right]^{1/2}$$

$$\times \sum_z \frac{(-1)^{i+1+z}(i+z-1)!(n+j-z+1)!}{z!(i-z+1)!(n-z)!(j-n+z-1)!}.$$

In the last term, the sum is taken over all integer z for which expressions under the factorial sign are non-negative. Note that the Clebsch–Gordan coefficients C_{i0j0}^{n0} and $C_{i(-1)j1}^{n0}$ [3] are nonzero only for the subscripts that obey the following conditions:

$$|i-j| \le n \le (i+j); \quad i+j+n = 2g. \tag{2}$$

This implies that oscillations excited in the second order of smallness with respect to the perturbation amplitude include the modes whose numbers obey conditions (2).

An analysis of the expressions for the $\lambda_{ijn}^{(\pm)}$ coefficients shows that, when the frequencies of modes with the numbers i, j, n obey one of the relations,

$$\omega_n^2 - (\omega_i \pm \omega_j)^2 = 0, \tag{3}$$

where

$$\omega_m^2 = m(m-1)\left[(m+2) - \frac{Q^2}{4\pi}\right],$$

the expression for the nth mode amplitude $M_n^{(2)}(t)$ contains a small denominator. It should be recalled that i and j are the numbers of modes determined from the spectrum of initial perturbation of the equilibrium spherical drop surface, while n is the number determined from relations (2), which corresponds to a mode excited in the second order of smallness due to the mode interaction. Thus, if any one of the relations (3) is satisfied for a drop charged below the critical level, the drop exhibits a resonance excitation of the nth surface oscillation mode.

Using relations (3), one can readily derive a resonance condition for the frequencies of the fourth and sixths modes ($\omega_6^2 = 4\omega_4^2$) obtained in [1]. To this end, it is sufficient to substitute $i = j = 4$ and $n = 6$ into Eq. (3). In other words, this situation represents a degenerate mode interaction corresponding to a twofold interaction between the fourth and sixth modes.

As can be readily seen, relations (3) can be satisfied in drops charged to a subcritical level (as characterized by parameter W) for a large number of combinations. For example, in a situation with $\omega_n = \omega_i + \omega_j$, initial excitation of the third and fourth modes leads to a resonance of the fifth mode at $W \approx 3.62$ (at a critical value of W equal to 4), initial excitation of the third and fifth modes leads to a resonance of the sixth mode at $W \approx 3.21$, and initial excitation of the ninth mode alone leads to a degenerate interaction with the fourteenth mode and gives rise to resonance of the latter at $W \approx 2.42$. This list of resonance interactions can be continued by proceeding to even higher modes.

From the standpoint of analysis of the critical conditions of the drop instability with respect to the intrinsic charge, it is of special interest to study the possibility of a resonance interaction whereby the energy is pumped from higher to lower modes rather than from lower to higher modes as in the examples presented above. For this purpose, it is necessary to consider the mode interaction under the condition $\omega_n = \omega_i - \omega_j$. The number of resonances possible in this situation is also large. Indeed, a resonance excitation of the third mode of capillary oscillations of a drop charged below the critical level takes place in nine cases, whereby the parameter W sequentially decreases from ~3.62 (for the initial excitation of the fourth and fifth modes) to ~0.19 (for the initial excitation of the twelfth and thirteenth modes). A resonance growth of the fourth mode takes place in four cases, whereby the parameter W sequentially decreases from ~3.62 (for the initial excitation of the third and fifth modes) to ~0.61 (for the initial excitation of the sixth and eighth modes).

According to the existing notions about the energy exchange between resonantly interacting modes [4], energy pumping from higher to lower modes is more effective and leads to a significant increase in the amplitude of the latter modes. Taking into account that the results of our calculations show a rapid decrease in the resonant values of W with increasing number of initially excited modes, we may expect that a large drop

charged to a level reasonable for stormy cloud conditions [5] would be subject to the development of surface instability as a result of the excitation of high oscillation modes upon collisions with significantly smaller drops [6]. In taking into account this circumstance, it would be expedient to renew the discussion as to the physical mechanism involved in the initiation of lightning discharge [7, 8].

Conclusion. A possible mechanism responsible for the breakage of charged drops at a low value of the intrinsic charge can be related to a nonlinear resonance energy pumping from higher to lower modes of capillary oscillations.

Acknowledgments. This study was supported by Presidential Grant no. 00-15-9925.

REFERENCES

1. J. A. Tsamopoulos and R. A. Brown, J. Fluid Mech. **147**, 373 (1984).
2. S. O. Shiryaeva, Pis'ma Zh. Tekh. Fiz. **26** (22), 76 (2000) [Tech. Phys. Lett. **26**, 1016 (2000)].
3. D. A. Varshalovich, A. N. Moskalev, and V. K. Khersonskii, *Quantum Theory of Angular Momentum* (Nauka, Leningrad, 1975; World Scientific, Singapore, 1988).
4. M. I. Rabinovich and D. I. Trubetskov, *Introduction to the Theory of Oscillations and Waves* (Nauka, Moscow, 1984).
5. I. P. Mazin, A. Kh. Khrgian, and I. M. Imyanitov, *Clouds and Cloud Atmosphere: a Handbook* (Gidrometeoizdat, Leningrad, 1989).
6. A. I. Grigor'ev, Zh. Tekh. Fiz. **70** (5), 22 (2000) [Tech. Phys. **45**, 543 (2000)].
7. V. A. Dyachuk and V. M. Muchnik, Dokl. Akad. Nauk SSSR **248** (1), 60 (1979).
8. A. I. Grigor'ev and S. O. Shiryaeva, Phys. Scr. **54**, 660 (1996).

Translated by P. Pozdeev

Technical Physics Letters, Vol. 28, No. 11, 2002, pp. 949–951. Translated from Pis'ma v Zhurnal Tekhnicheskoĭ Fiziki, Vol. 28, No. 22, 2002, pp. 52–58.
Original Russian Text Copyright © 2002 by Alekseev, Bazarov, Gubin, Kovalenko, Sazonov, Starostin.

Recirculation Fiber Loop Interferometer with a Faraday Reflector

É. I. Alekseev, E. N. Bazarov, V. P. Gubin, V. G. Kovalenko, A. I. Sazonov, and N. I. Starostin

Fryazino Branch, Institute of Radio Engineering and Electronics, Russian Academy of Sciences, Fryazino, Moscow oblast, Russia

e-mail: http://fire.relarn.ru

Received April 22, 2002

Abstract—A new optical scheme of the recirculation fiber loop interferometer with a Faraday reflector and a broadband radiation source is suggested. It is experimentally established that this scheme provides for a more than tenfold decrease in the instrument zero response caused by a spurious polarization modulation in the phase modulator. Factors leading to additional shifts in the instrument zero response are revealed. © *2002 MAIK "Nauka/Interperiodica".*

Recirculation fiber loop interferometers (RFLIs) [1] represent low-coherent optical devices of a new type combining the advantages of the traditional Sanjack interferometer employing a broadband light source and those of a resonant loop interferometer with a narrowband source. RFLIs can be implemented in various measuring systems and transducers (e.g., angular velocity meters). Among the several proposed RFLI schemes [1–4], the least studied is that with an external reflector [3, 4]. An advantage of this scheme is the simplicity of its matching with a reflection phase modulator, in which the light passes through the modulating element in both forward and backward directions.

By using a Faraday polarization mode converter [5] in the reflection modulator, it is possible to provide for at least a 100-fold compensation [6] of the spurious polarization modulation (SPM), which almost always takes place in phase modulators, in particular, in those with modulating elements employing an optical fiber wound on a piezoelectric cylinder. Such modulators are widely used in modern interferometers due to their low cost, small optical losses, and the simplicity of matching them with other elements.

The optical fiber in a piezoelectric modulating element is subject to both longitudinal and transverse stresses, which lead, in addition to the useful phase modulation, to a spurious polarization modulation. This SPM is among the factors determining the interferometer errors. In order to reduce the SPM level, a number of methods have been suggested [3, 6–8]. The most effective of these is the aforementioned principle of compensation in the reflection modulator [3, 6]. The aim of this study was to estimate the SPM level in the proposed RFLI scheme with an external Faraday reflector.

The practical implementation of RFLIs encounters difficulties related to the required 90° rotation of the light polarization plane in a modulator with a Faraday reflector. In the proposed scheme, this difficulty was partly surmounted by using a new optical scheme (Fig. 1) representing one of the possible variants of a fiber loop interferometer with a Faraday reflector. The phase-sensitive element of the proposed RFLI is fiber loop *5* in which the light waves from broadband source *1* (with an average wavelength of 1.55 μm and a spectral width of 20 nm) travel in opposite directions. Photodetector *10* measures signals due to the interference of waves, the phase difference of which depends on a factor (e.g., rotation) acting upon loop *5*. The output signal is monitored by a scheme using the harmonic phase modulation of light waves and a lock-in detection of the modulated output radiation component.

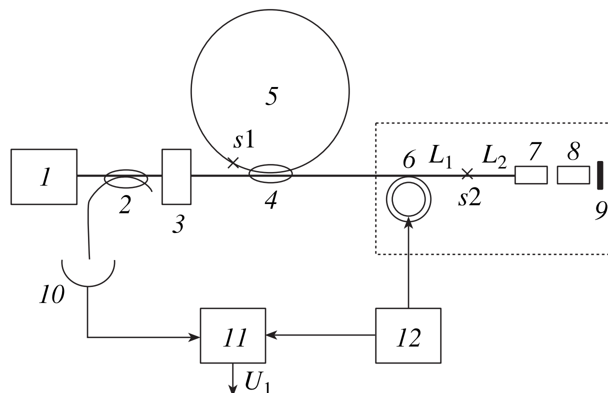

Fig. 1. Optical scheme of an RFLI with a Faraday reflector: (*1*) light source; (*2*, *4*) directional couplers; (*3*) polarizer; (*5*) fiber loop; (*6*) piezoelectric fiber loop; (*7*) collimator; (*8*) 45° Faraday rotator; (*9*) blunt mirror; (*10*) photodetector; (*11*) phase lock-in detector; (*12*) master generator; and *s*1 and *s*2, optical junctions.

1063-7850/02/2811-0949$22.00 © 2002 MAIK "Nauka/Interperiodica"

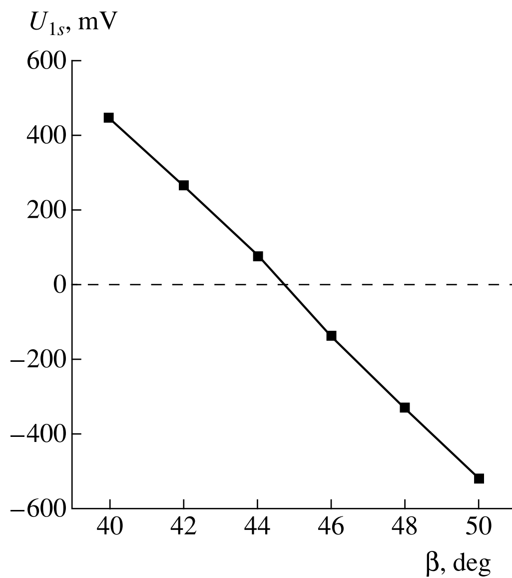

Fig. 2. The plot of RFLI zero response versus β angle at junction *s*2.

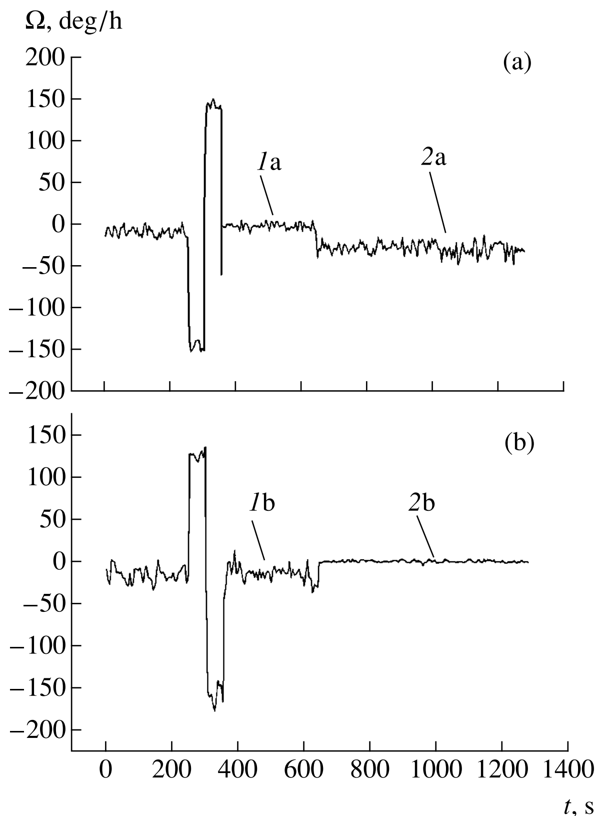

Fig. 3. Time variation of the (*1*) equiphase and (*2*) quadrature components of the RFLI output signal recorded in the schemes with (a) a usual mirror and (b) a Faraday reflector.

In the given scheme, 45° Faraday rotator *8* performs the function of a polarization mode converter. The useful phase modulation of the optical radiation at a frequency of f_m = 42 kHz is performed in piezoelectric fiber element *6*. This element represents a piezoceramic disk with a diameter of 50 mm and an aluminum ring pressed onto this disk on which an optical fiber of the PANDA type (12 turns) is wound at a 50-g load. The RFLI scheme is made of the same optical fiber.

In the proposed scheme, the output radiation polarization at the exit of the modulator is rotated by 90° relative to the input polarization direction. In order to ensure that the opposite waves carrying information about the sensor rotation return to polarizer *3* with a correct linear polarization, one of the contacts (*s*1) between phase-sensitive loop *5* and directional coupler *4* is made so as to provide for a 90° rotation of the fiber birefringence axes. Note that this scheme ensured attenuation of a spurious light component entering the polarizer without passing through the loop. Another feature of the proposed scheme is the presence of junction *s*2, in which the optical contact is made with a 45° rotation of the fiber birefringence axes.

In this interferometer, SPM is manifested in the amplitude modulation (additional to that due to the sensor rotation) of the output voltage of photodiode *10* with a frequency of f_m and an amplitude of U_1. The value of U_1 has to be determined in the absence of sensor rotation and for the other spurious signals in the RFLI made as small as possible. We measured U_1 using a phase lock-in technique with registration of the equiphase (U_{1s}) and quadrature (U_{1q}) signal components, which yields $U_1^2 = U_{1s}^2 + U_{1q}^2$. The equiphase detector tuning corresponds to a maximum sensitivity of the interferometer with respect to rotation, while the quadrature signal component is related predominantly to SPM [7]. The efficiency of SPM suppression in the proposed scheme was characterized by the ratio of the quadrature signal components in the RFLI schemes with the usual mirror and the Faraday reflector. For this purpose, the experimental setup was provided with a facility that ensured switching between the two schemes.

Experiments with the scheme employing the Faraday reflector revealed a dependence of the zero response shift U_{1s} on the angle β of mutual rotation of fibers in the *s*2 contact (see Fig. 2) with a slope of 0.7 mV/(deg/h). A zero shift corresponds to approximately 45° rotation of the fiber birefringence axes. The slope of $U_1(\beta)$ depends on the experimentally selected lengths L_1 and L_2. The results of our experiments showed that there are problems related to the reciprocity of the opposite waves that are not quite clear; these problems were probably caused by the nonideality of the Faraday rotator employed, in which the angle of the mode field rotation deviated from 45°.

In order to evaluate the degree of SPM suppression in the proposed scheme, the RFLI output signal was recorded in the absence of sensor rotation using the equiphase and quadrature (the output signal measured 600 s after the record start) tunings of the phase detector in the schemes with the usual and Faraday reflectors

(Fig. 3). The measurements were performed with a calibration signal (±140 deg/h) superimposed on the equiphase component of the output signal; the magnitude of the quadrature component was close to a maximum value in both variants. In the scheme with the Faraday reflector, the quadrature component virtually coincides with the zero response of electronics and exhibits a small drift. This is evidence of the absence of significant quadrature signals in the proposed scheme and, hence, of a significant suppression of SPM. The magnitude of the quadrature component was –27.5 ± 7.4 deg/h for the usual scheme against –1.85 ± 1.3 deg/h for the Faraday mirror, which shows that the quadrature component was suppressed by a factor of about 15. Another important fact is the relatively small noise of the quadrature component (related primarily to the ambient temperature variations) in the scheme with the Faraday reflector (one-sixth of that in the scheme with the usual mirror).

It should be noted that we did not aim at obtaining a small drift of the RFLI zero (equiphase component). Solving this task would require studying the additional zero shifts revealed in the proposed RFLI scheme. The level of suppression of the SPM level achieved in these experiments was limited by a number of factors, the most significant of which is related, in our opinion, to uncertainty in the mode conversion caused by the error in the polarization plane rotation in the polarizer employed.

To summarize, we suggested a new optical scheme for a recirculation fiber loop interferometer with a Faraday reflector, experimentally demonstrated that this scheme provides for a more than tenfold decrease in the instrument zero response caused by a spurious polarization modulation in the phase modulator, and revealed factors leading to additional shifts in the instrument zero response.

Acknowledgments. The authors are grateful to B.L. Davydov and E.A. Konstantinov for their help in preparation of the experiment.

This study was supported by the Russian Foundation for Basic Research, project no. 00-02-17344.

REFERENCES

1. A. Yu and A. S. Siddiqui, Electron. Lett. **28**, 1778 (1992).
2. É. I. Alekseev, E. N. Bazarov, V. P. Gubin, *et al.*, Kvantovaya Élektron. (Moscow) **31**, 1113 (2001).
3. É. I. Alekseev and E. N. Bazarov, Pis'ma Zh. Tekh. Fiz. **23** (15), 90 (1997) [Tech. Phys. Lett. **23**, 613 (1997)].
4. Z. Hu, X. Ma, F. Li, *et al.*, Proc. SPIE **3860**, 348 (1999).
5. K. H. Wanser, Proc. SPIE **891**, 204 (1988).
6. É. I. Alekseev, E. N. Bazarov, V. P. Gubin, *et al.*, Radiotekh. Élektron. (Moscow) **44** (1), 122 (1999).
7. B. Szafraniec and J. Blake, J. Lightwave Technol. **12** (9), 1679 (1994).
8. D. G. Luke, R. McBridge, J. G. Burnett, *et al.*, Opt. Commun. **121**, 115 (1995).

Translated by P. Pozdeev

Technical Physics Letters, Vol. 28, No. 11, 2002, pp. 952–954. Translated from Pis'ma v Zhurnal Tekhnicheskoĭ Fiziki, Vol. 28, No. 22, 2002, pp. 59–63.
Original Russian Text Copyright © 2002 by Abduev, Asvarov, Akhmedov, Baryshnikov, Terukov.

Vapor Phase Synthesis of ZnO Structures

A. Kh. Abduev, A. Sh. Asvarov, A. K. Akhmedov, V. G. Baryshnikov, and E. I. Terukov

Institute of Physics, Dagestan Scientific Center, Russian Academy of Sciences, Makhachkala, Dagestan, Russia

Ioffe Physicotechnical Institute, Russian Academy of Sciences, St. Petersburg, 194021 Russia

Received May 27, 2002

Abstract—We observed zinc oxide structures formed in an oxygen-containing atmosphere as a result of oxidation of the surface of zinc droplets. The gas-phase oxidation leads to the formation of hollow ZnO whiskers on the metal surface, which grow due to the transport of zinc vapor through their channels. It was found that high partial pressures of zinc and atomic oxygen give rise to fractal structures, which appear in a cascade process involving the sequential formation of zinc oxide vapor, ZnO clusters, and cluster aggregates as a result of the cluster–cluster interaction. A deposit of ZnO synthesized on the cathode surface exhibits a columnar structure. © *2002 MAIK "Nauka/Interperiodica".*

The process of zinc oxide whisker growth has been extensively studied (see, e.g., [1–5]). Recently, we reported on the observation of hollow annular ZnO structures [6], while Huang *et al.* [7, 8] observed the phenomenon of UV emission from ZnO whiskers at room temperature. Considerable attention in these investigations is paid to the mechanism of whisker growth. In earlier works [1–3], the key role in the formation of ZnO whiskers was attributed to a diffusion-dislocation mechanism. In recent years, the experimental results are usually interpreted within the framework of Wagner's vapor–liquid–crystal (VLC) model [7–9], whereby it is suggested that a material ensuring the formation of a liquid phase on a growth surface has to be applied onto a substrate in order to provide for the whisker growth.

We studied the synthesis of ZnO aggregates formed in the gas phase and on a substrate in the Zn–O system. In order to study the whisker growth at various partial pressures of Zn vapor and O_2, the experiments were performed under the conditions of electric-arc spraying of zinc oxide and evaporation of metallic zinc. All materials were of special purity (OSCh) grade.

1. The experiments with electric-arc spraying were performed in a chamber filled with argon to a pressure of 10 Torr at a discharge current of 400 A between a water-cooled graphite cathode and a ZnO ceramic anode. The sprayed ceramic anode with a 6×10 mm cross section was made of ZnO with 2% aluminum oxide additive to provide for the necessary conductivity. Plasma, formed as a result of the thermal decomposition of zinc oxide, contained equal molar fractions of zinc and oxygen atoms.

Figure 1 shows micrographs of a material deposited on the cathode. The interaction between oxygen and zinc vapor leads to the formation of ZnO molecules with a high concentration in the gas phase. We believe that a dominating process in the next stage (condensation) is the formation of ZnO clusters. Interaction between these clusters leads to the growth of aggregates. The resulting fractal structures are deposited onto the flat cathode surface to form a layer of the cathode deposit (Fig. 1a). Micrographs of the cross sections

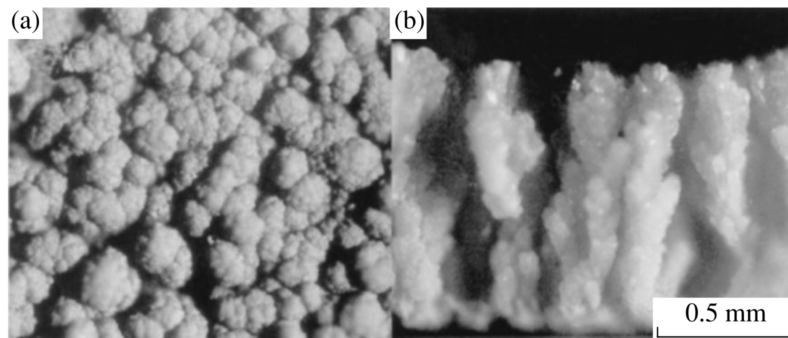

Fig. 1. Micrographs of the (a) surface and (b) cross section of a columnar ZnO deposit on the cathode.

1063-7850/02/2811-0952$22.00 © 2002 MAIK "Nauka/Interperiodica"

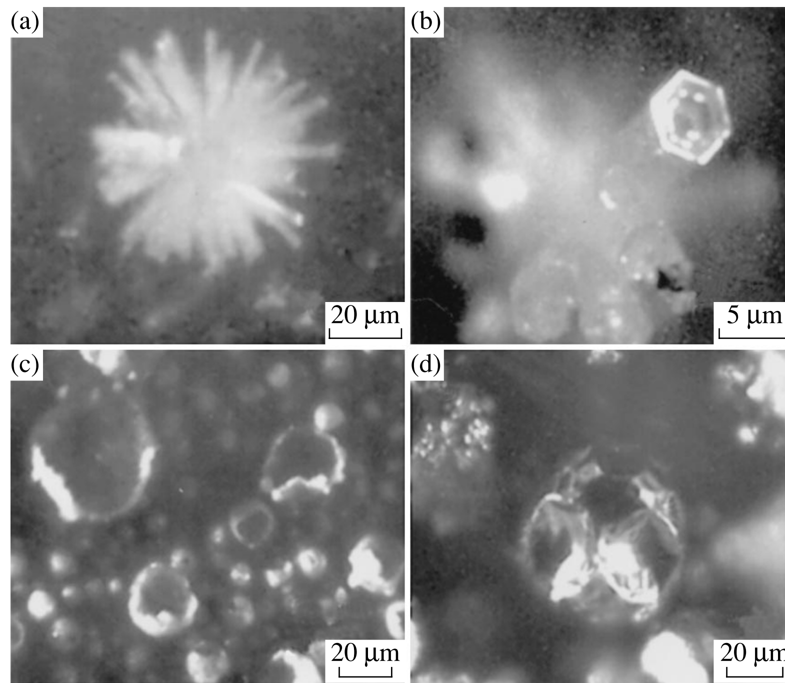

Fig. 2. Micrographs of (a) ZnO aggregates formed in the gas phase, (b) a whisker edge, (c) oxide shells formed upon the explosion of zinc drops, and (d) the surface of a zinc drop with elements of ordering.

of such a layer showed that the deposit possesses a columnar structure (Fig. 1b).

The nature of the columnar structures is probably related to the formation of three-dimensional fractals from ZnO aggregates by the Witten–Sunders mechanism [10]. It should be noted that we observed neither homogeneous nor heterogeneous growth of whiskers in the course of the electric-arc spraying of zinc oxide. We believe that the observed behavior is explained by a high spatial localization of the reactants, which precludes their separate transport to a growth surface and leads to the formation of fractal structures immediately in the gas phase.

2. Structures formed during the evaporation of zinc in a counterflow of oxygen atoms are depicted in Fig. 2. In order to exclude the appearance of zinc molecules in the primary flux of evaporated zinc, the metal sample was placed into a graphite cell. The process was conducted in an open tubular furnace. When the temperature exceeded 1000°C, an oxide film coating the zinc surface was broken and a zinc vapor-drop phase was ejected into the cell channel. It was possible to observe, with the naked eye, how the hedgehoglike zinc oxide aggregates fell from the cell onto a substrate surface (Fig. 2a). At the same time, whiskers reaching up to several millimeters in length and several microns in diameter were found to grow in the neighboring zone, as well as around the cell nozzle edge. As the distance from the nozzle edge increases and the partial pressure of oxygen grows, zinc oxide grows in the form of a porous material composed of small whiskers.

Previously [6], we established that the growth of hollow dendrite structures is due to the transport of zinc vapor via the dendrite channel and the reaction of zinc oxidation at the growing dendrite edge. We believe that the growth of ZnO hedgehogs is due to the oxidation of small zinc droplets, local breakage of the oxide film, and the formation of hollow whiskers from the core material (Fig. 2b). Investigation of the behavior of a piece of zinc heated in an oxygen-containing atmosphere showed that, at temperature above the boiling point of zinc melt, the sample exhibits a cascade process involving oxidation, oxide shell breakage, and metal ejection in the form of a metal vapor and small droplets (Fig. 2c). It is suggested that, when droplets are ejected from beneath the oxide shell, the local surface temperature drops. This results in the formation of Benard cells, which leads to the appearance of local surface oxidation regions and hollow whisker channels. Examination of the surface of zinc drops upon cooling shows evidence of such ordering (Fig. 2d).

The formation of monolithic whiskers takes place at the graphite cell nozzle edge, in the region where the fluxes of oxygen and zinc vapor collide at a sufficiently high temperature (about 1000°C) excluding the incorporation of atoms into a lattice on the whisker side walls. The results of our investigations show that a necessary condition for the whisker growth is the separate delivery of reactants to the growth surface, which excludes the formation of zinc oxide molecules and clusters in the gas phase.

In our experiments, no impurities ensuring that the process would proceed by the VLC mechanism were introduced into the system. We believe that this mechanism would be operative if a liquid phase of zinc could form on the (0001)ZnO plane as a result of the melting temperature depression in the ZnO–Zn system at a sufficiently high zinc pressure or due to the formation of a hypothetical zinc hemioxide (Zn_2O).

An analysis of the results of our investigation allows the following conclusions to be made:

(i) High local partial pressures of zinc and oxygen lead to their intense interaction with the formation of ZnO clusters, which aggregate into a cathode deposit possessing a columnar structure.

(ii) Separate delivery of oxygen and zinc vapor to the growth surface at a temperature of about 1000°C leads to the growth of ZnO whiskers in the absence of additional impurities.

(iii) The presence of a droplet phase may lead to the formation of hollow whiskers on the surface of oxidized drops by a mechanism involving the transport of zinc from inside the drop to the growth site via channels in the growing whiskers.

The above results are of practical significance for the creation of gas sensors employing ZnO aggregates with anomalously developed surfaces and for the development of thin-film varistors.

REFERENCES

1. Y. S. Park and D. C. Reynolds, J. Appl. Phys. **38** (2), 756 (1967).
2. Ram Bilas Sharma, J. Appl. Phys. **41** (4), 1866 (1970).
3. S. D. Sharma and Subhash Kashyap, J. Appl. Phys. **42** (13), 5302 (1971).
4. Ikumaro Kubo, Jpn. J. Appl. Phys. **4**, 225 (1965).
5. Hiroshi Iwanaga and Noboru Shibata, J. Cryst. Growth **24**/**25**, 357 (1974).
6. A. Kh. Abduev, A. K. Akhmedov, V. G. Baryshnikov, and Sh. O. Shakhshaev, Pis'ma Zh. Tekh. Fiz. **26** (8), 37 (2000) [Tech. Phys. Lett. **26**, 332 (2000)].
7. Michael H. Huang, Samuel Mao, Henning Feick, *et al.*, Science **292**, 1897 (2001).
8. Michael H. Huang, Yiying Wu, and Henning Feick, Adv. Mater. **13** (2), 113 (2001).
9. E. I. Givargizov, *Growth of Whiskers and Platelike Crystals from Vapor Phase* (Nauka, Moscow, 1977).
10. B. M. Smirnov, Usp. Fiz. Nauk **149** (2), 177 (1986) [Sov. Phys. Usp. **29**, 481 (1986)].

Translated by P. Pozdeev

Technical Physics Letters, Vol. 28, No. 11, 2002, pp. 955–957. Translated from Pis'ma v Zhurnal Tekhnicheskoĭ Fiziki, Vol. 28, No. 22, 2002, pp. 64–69.
Original Russian Text Copyright © 2002 by Mynbaev, Bazhenov, Smirnov, Ivanov-Omskiĭ.

Electrical Properties of $Cd_xHg_{1-x}Te$ and $Zn_xCd_yHg_{1-x-y}Te$ Modified by Low-Energy Ion Bombardment

K. D. Mynbaev, N. L. Bazhenov, V. A. Smirnov, and V. I. Ivanov-Omskiĭ

Ioffe Physicotechnical Institute, Russian Academy of Sciences, St. Petersburg, 194021 Russia

e-mail: mynkad@mail.ioffe.ru

Received June 3, 2002

Abstract—The phenomenon of conversion of the conductivity type in *p*-type samples of the $Cd_xHg_{1-x}Te$ ($0.28 \le x \le 0.55$) and $Zn_xCd_yHg_{1-x-y}Te$ solid solutions bombarded by low-energy argon ions was studied. It is shown that a necessary condition for the conversion effect in $Cd_xHg_{1-x}Te$ with $0.28 \le x \le 0.39$ is ion neutralization in the bombarding beam. The dependence of the conversion layer thickness in $Cd_xHg_{1-x}Te$ on the solid solution composition agrees with that predicted by the diffusion model of ion-bombardment-induced conversion of the conductivity type. © *2002 MAIK "Nauka/Interperiodica".*

Possessing unique physical properties, solid solutions of the cadmium mercury telluride $Cd_xHg_{1-x}Te$ (CHT) system are still used as base materials for infrared optoelectronics. In recent years, one of the main methods used for the *p–n* junction formation in CHT based photodetectors was bombardment by low-energy ions of inert gases, which produces conversion of the conductivity type from *p* to *n* in a surface layer of preset thickness [1–4].

Previously [2, 5], we reported on the results of experiments aimed at the creation of *p–n* junctions in $Cd_xHg_{1-x}Te$ and on the properties of the resulting *n*-type layers. The *p–n* conversion was observed only in the samples with $x \le 0.24$, which corresponds to the bandgaps $E_g \le 0.15$ eV and the photosensitivity threshold $\lambda \sim 9$ μm at $T = 77$ K.

Now, we report on successful experiments in which the conductivity type of epitaxial CHT layers with *x* up to 0.39 ($E_g \le 0.41$ eV; $\lambda \ge 3$ μm) was inverted by low-energy ion bombardment. We also studied the conductivity type conversion in layers of the $Zn_xCd_yHg_{1-x-y}Te$ (ZCHT) solid solutions with $0.15 \le E_g \le 0.35$ eV. These semiconductors are considered as an alternative to CHT, since the introduction of Zn must stabilize the weak Hg–Te bonds and, hence, improve the material quality. However, data on ion-bombardment-induced conversion of the conductivity type in ZCHT are very restricted [6, 7].

The experiments were performed with samples of layers grown on CdTe substrates by liquid-phase epitaxy (LPE) from Te-rich solutions. After post-growth annealing in mercury vapor, we obtained *p*-type samples with an uncompensated donor concentration of $N_a - N_d = (4.6–380) \times 10^{15}$ cm^{-3}. Then, the samples were bombarded in a vacuum chamber by a beam of neutralized argon ions with the energy varied from 60 to 800 eV and the beam current density, from 0.05 to 0.2 mA/cm^2. The treatment duration was 20 min; no special measures were taken to cool the samples during ion bombardment.

The conversion depth *h* and the electrical characteristics of *n*-type layers in the ion-bombarded samples were studied by measuring the Hall coefficient and the dc conductivity profiles in the course of layer-by-layer etching with a step of 0.7 μm. The measurements were performed at 77 K for ZCHT and CHT with $x < 0.4$ and at 300 K for CHT with $x > 0.5$.

Table 1 presents the results of measurements of the electrical properties of epitaxial CHT layers with $0.28 \le x \le 0.55$ before and after bombardment with 400-eV argon ions at an ion beam current density of 0.1 mA/cm^2. As can be seen, the conversion took place in all samples with $x < 0.5$. A low density (n) and high mobility (μ_n) of electrons is evidence of good quality in the *n*-type layers. The data in Table 1 confirm the previously observed relation between the values of *n* upon conversion in the ion-bombarded samples and $N_a - N_d$ in the initial layers [5]. Note that the electrical characteristics of inverted layers were virtually independent of the ion energy and beam current density.

We studied the conversion layer thickness (h) as a function of the solid solution composition (x) for CHT samples treated in the same regime (see figure). Since the samples possessed different initial $N_a - N_d$ values, we took into account that (as established previously [5]) *h* is inversely proportional to $(N_a - N_d)^{1/2}$ by plotting $L = h(N_a - N_d)^{1/2}$ versus *x*. As can be seen from the figure, *L* decreases with increasing *x*.

This result agrees well with the commonly accepted diffusion model of conductivity type conversion in CHT bombarded by low-energy ions. According to this model, the conversion is related to diffusion of the

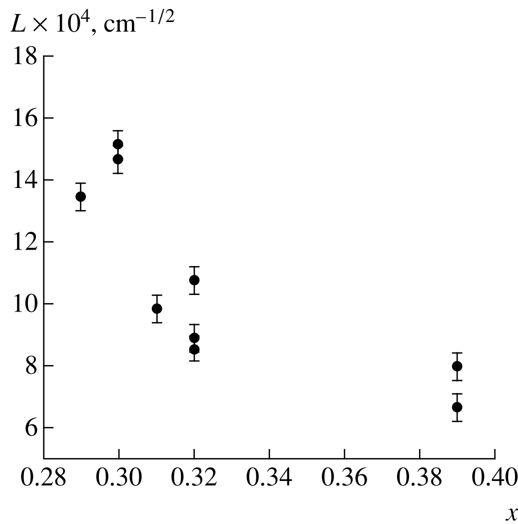

The plot of $L = h(N_a - N_d)^{1/2}$ versus composition x for $Cd_xHg_{1-x}Te$ samples upon low-energy ion bombardment.

interstitial mercury atoms, liberated in the course of the ion sputtering of the CHT surface, and their annihilation, with the mercury vacancies–acceptors determining the *p*-type of conductivity in the initial material [3, 5, 8]. Within the framework of this model, $h^2/t \sim C_sD/(N_a - N_d)$, where D is the diffusion coefficient, C_s is the surface concentration of interstitial mercury atoms, and t is the diffusion (treatment) duration. Obviously, the strong variation of $h(x)$ depicted in the figure implies that C_s sharply decreases with increasing x. Indeed, it is known that the ion sputtering rate of CHT and, hence, the rate of free mercury production on the bombarded surface decrease with increasing x [9]. This is accompanied by a drop in the fraction of mercury in the total number of liberated atoms. In addition, the growth of x (and, hence, of E_g) increases the role of the internal electric field at the conversion layer boundary, which additionally decreases the effective C_s value [10].

Table 2 presents data on the electrical properties of epitaxial ZCHT layers measured before and after ion bombardment in the same regime as that specified above. For this material, the E_g value was determined from the half-decay of the room-temperature optical transmission of ZCHT layers. As can be seen, these samples are also characterized by a low concentration and high mobility of electrons upon ion-bombardment-induced *p–n* conversion. However, no correlation was found between n in the inverted layers and $N_a - N_d$ in the initial *p*-type material. Nor did we observe any clear dependence of h on either x, y or E_g in the ZCHT samples studied.

In the experiments described above, we observed *p–n* conversion in CHT samples with $x \le 0.39$ ($E_g \le 0.41$ eV) bombarded with a beam of neutralized argon ions. It should be noted that no conversion in the CHT layers with $x > 0.24$ was observed previously [2, 5]. However, the previous experiments were performed with a beam on Ar^+ ions without neutralization with the samples mounted on dielectric substrata. Thus, the effect of conductivity type conversion in the CHT samples with $x > 0.24$ apparently depends on whether the sample is irradiated by a beam of charged or neutralized ions. Bombardment with the beam of ions creates a charged layer on the target surface. In the case of narrow-bandgap semiconductors such as CHT solid solutions with $x \sim 0.2$, this charge is compensated by intrinsic carriers (the concentration of which at the temperature of treatment is rather high).

In a material with large x (and E_g), the density of intrinsic carriers is much lower and insufficient to compensate for the charge accumulated at the surface. The accumulated uncompensated charge hinders sputtering of the surface by low-energy ions. Moreover, the effect of the surface charge adds is added to the effect of the aforementioned internal electric field of charged defects. As a result, the effective surface interstitial mercury concentration C_s significantly decreases and

Table 1. The electrical properties of epitaxial $Cd_xHg_{1-x}Te$ layers before and after bombardment with neutralized low-energy ions

Sample	E_g, eV (300 K)	x	Before treatment		After treatment	
			$N_a - N_d$, cm^{-3}	μ_p, cm^2/(V s)	n, cm^{-3}	μ_n, cm^2/(V s)
C1	0.264	0.28	8.0×10^{15}	360	1.0×10^{15}	3.7×10^4
C2	0.291	0.30	1.1×10^{16}	420	1.4×10^{15}	6.2×10^4
C3	0.304	0.31	7.3×10^{15}	460	6.3×10^{14}	2.1×10^4
C4	0.318	0.32	3.2×10^{16}	420	2.7×10^{15}	4.9×10^3
C5	0.412	0.39	1.8×10^{16}	250	1.1×10^{15}	1.9×10^4
C6	0.412	0.39	2.2×10^{16}	260	8.8×10^{14}	2.0×10^4
C7	0.565	0.50	2.1×10^{16}	75	No conversion	
C8	0.594	0.52	2.4×10^{16}	120	"	
C9	0.637	0.55	2.3×10^{16}	260	"	

Table 2. The electrical properties of epitaxial $Zn_xCd_yHg_{1-x-y}Te$ layers before and after bombardment with neutralized low-energy ions

Sample	E_g, eV	Composition		Before treatment		After treatment	
		x	y	$N_a - N_d$, cm^{-3}	μ_p, cm^2/(V s)	n, cm^{-3}	μ_n, cm^2/(V s)
Z1	0.344	0.17	0.07	8.0×10^{16}	230	1.0×10^{14}	3.0×10^4
Z2	0.275	0.11	0.15	2.5×10^{16}	305	1.7×10^{15}	1.5×10^4
Z3	0.199	0.11	0.09	1.2×10^{17}	155	3.1×10^{15}	4.1×10^4
Z4	0.185	0.11	0.09	4.6×10^{15}	350	1.1×10^{15}	9.0×10^3
Z5	0.185	0.13	0.10	3.8×10^{17}	130	6.9×10^{14}	1.3×10^5
Z6	0.146	0.08	0.09	3.1×10^{17}	200	3.5×10^{15}	2.3×10^4

no conversion takes place. In the material with $x > 0.5$, a decrease in the total content of mercury and the action of the internal field reduce C_s so strongly that even irradiation by a neutralized beam (not charging the surface) does not lead to conversion of the conductivity type.

REFERENCES

1. M. V. Blackman, D. E. Charlton, M. D. Jenner, *et al.*, Electron. Lett. **23** (19), 978 (1987).
2. V. I. Ivanov-Omskiĭ, K. E. Mironov, and K. D. Mynbaev, Fiz. Tekh. Poluprovodn. (Leningrad) **24** (12), 2222 (1990) [Sov. Phys. Semicond. **24**, 1379 (1990)].
3. E. Belas, R. Grill, J. Franc, *et al.*, J. Cryst. Growth **159** (1–4), 1117 (1996).
4. G. Bahir, V. Garber, and D. Rosenfeld, Appl. Phys. Lett. **78** (10), 1331 (2001).
5. V. I. Ivanov-Omskiĭ, K. E. Mironov, and K. D. Mynbaev, Semicond. Sci. Technol. **8** (5), 634 (1993).
6. P. Brogowski, H. Mucha, and J. Piotrowski, Phys. Status Solidi A **114**, K37 (1989).
7. S. Rolland, R. Granger, and R. Triboulet, J. Cryst. Growth **117**, 208 (1992).
8. D. Shaw and P. Capper, J. Mater. Sci.: Mater. Electron. **11** (2), 169 (2000).
9. L. Wang and L. H. Zhang, J. Electron. Mater. **29** (6), 873 (2000).
10. V. V. Bogoboyashchiĭ and I. I. Izhnin, Izv. Vyssh. Uchebn. Zaved., Fiz. **43** (8), 16 (2000) [Russ. Phys. J. **43** (8), 627 (2000)].

Translated by P. Pozdeev

Technical Physics Letters, Vol. 28, No. 11, 2002, pp. 958–961. Translated from Pis'ma v Zhurnal Tekhnicheskoĭ Fiziki, Vol. 28, No. 22, 2002, pp. 70–77.
Original Russian Text Copyright © 2002 by Volyar, Fadeeva, Egorov.

Vector Singularities of Gaussian Beams in Uniaxial Crystals: Optical Vortex Generation

A. V. Volyar, T. A. Fadeeva, and Yu. A. Egorov

Tauride National University, Simferopol, Ukraine

Received April 15, 2002

Abstract—The propagation of a circularly polarized singular beam through a uniaxial crystal is accompanied by the appearance of additional singularities in the polarization structure of the beam field. These vector singularities combine to form concentric ombilic lines—degenerate ombilic points of the star type, thus significantly changing the entire fine structure of the field. When the beam passes through a birefringent quarter-wave plate and a polarizer, the vector singularities transform into the usual optical vortices. Rotation of the polarizer and/or of the quarter-wave plate drives the vortices to move by preset trajectories, merge with one another, or break into elementary singularities. These processes are studied using theoretical and experimental methods. © *2002 MAIK "Nauka/Interperiodica".*

The formation of optical vortices is usually related to the creation of phase transparencies in which rotation of the field around a singular point changes the phase by a multiple of 2π. In particular, the intracavity generation of singular beams assumes the use of a phase transparency or mirror with a helicoidal surface repeating the structure of the vortex wave front [1]. A similar approach is used for the extracavity generation, in which case the method is modified by forming a computer-synthesized hologram placed in the propagating laser beam [2]. The first method is based on the use of high-precision technologies and requires laser mirrors of strictly controlled shape. Ignoring these requirements leads to significant structural distortions of the singular beam [1]. The second method, while offering a simple and original solution, possesses a relatively low energy efficiency (not exceeding 10%). In addition, neither of these methods allows the properties of optical vortices to be smoothly controlled.

However, as long ago as in 1981, Nye [3] pointed out unusual properties of an inhomogeneously polarized electromagnetic wave featuring singularities of one of the electric and magnetic field components. According to Nye, the so-called *C*-lines (trajectories on which the amplitude of either right- or left-handed circular polarization becomes zero) are identified with dislocations of the wave front of the corresponding field component. Using this approach, we can alternatively treat the problem of optical vortex generation and control.

This study addresses the process of conversion of the vector singularities of the field of a Gaussian beam, propagating in a uniaxial crystal, into bound and free optical vertices.

Let us consider the case of a Gaussian beam propagating along the optical axis Oz in a uniaxial crystal. In this case, the permittivity tensor components are determined as $\varepsilon_x = \varepsilon_y = \varepsilon^{(o)} = \varepsilon$ and $\varepsilon_z = \varepsilon^{(e)}$. Hillion [4] treated this problem on an abstract mathematical level in the case of paraxial beams. Unfortunately, the implicit relations obtained in [4] do not provide for a detailed analysis of the process of creation, annihilation, and evolution of vector singularities. For this reason, we will employ an approximate solution to the Maxwell equations for a paraxial beam in combination with the ray approach [5].

First, we should like to note that the eikonal equation and the parabolic wave equation [6] for beams are obtained in the same approximation of $kz_0 \gg 1$ or $(\lambda/\rho)^2 \ll 1$, where $z_p = k\rho_0^2/2$, $k = 2\pi/\lambda$, and ρ_0 is the beam waist radius at $z = 0$. Taking into account this circumstance, it is possible to represent the Gaussian beam as a sum of ray trajectories lying on the surfaces of embedded one-sheet hyperboloids of revolution [5]. A local plane wave propagates along each ray, so that the phase difference gained between orthogonal components of the local electric field is $\delta = k\Delta nh\sin^2\theta_R$, where $\Delta n = n^{(e)} - n^{(o)} \approx (\varepsilon^{(e)} - \varepsilon^{(o)})/2\varepsilon$, h is the geometric length of the ray between the waist plane and the plane of observation, and θ_R is the angle between the ray and the optical axis Oz [7, 8]. Assuming that all rays originate from the same point and travel in the crystal at an angle θ to the optical axis, we can take $\theta \approx \theta_R$ in the paraxial approximation. In addition, we can take into account that the geometric lengths of a given ray h and a ray in the beam H are approximately equal ($H \approx h$). For this reason, the phase difference between orthogonal components of the electric vector of a local wave is

$$\delta = k\Delta n r^2/\sqrt{r^2+z^2}, \quad r^2 = x^2+y^2, \tag{1}$$

where z is the distance along the optical axis between the waist plane and the plane of observation.

Now, let us consider transformations exhibited by the Jones vector of a local wave propagating through the crystal. Consider a local system of coordinates (u, ν, η) related to the ray. The Ou axis is oriented parallel to the plane containing the ray and the optical axis, and the Oν axis is perpendicular to this plane. Let us assume that a circularly polarized beam with the Jones vector $\mathbf{g} = \frac{1}{\sqrt{2}}\binom{1}{\sigma i}$ ($\sigma = \pm 1$ is the helicity of the beam, that is, the direction of circulation of the electric vector) is incident onto the crystal. Then, the Jones vector components g_x and g_y in the Cartesian basis set can be expressed as

$$\begin{aligned} g_x &= \cos\delta/2 + i\sin\delta/2\exp(i2\varphi), \\ g_y &= i\sigma[\cos\delta/2 - i\sin\delta/2\exp(i2\varphi)], \end{aligned} \tag{2}$$

where φ is the angle of inclination of the beam propagation plane to the zOx plane. The field components of the Gaussian beam can be written in the paraxial approximation using the relations [5]

$$e_x = \Psi g_x, \quad e_y = \Psi g_y, \quad e_z \approx i/k\nabla\mathbf{e}_t,$$

$$\mathbf{h}_t = \sqrt{\varepsilon}\mathbf{k}\times\mathbf{e}_t, \quad \mathbf{h}_t \approx -i/k\sqrt{\varepsilon}\nabla_t\times\mathbf{e}_t,$$

where

$$\nabla_t = \hat{i}\partial_x + \hat{j}\partial_y, \tag{3a}$$

$$\Psi = \frac{1}{\xi}\left(\frac{r}{\xi}\right)^{|l|}\exp\left(-\frac{r^2}{\rho^2\xi}\right)\exp[il\varphi] \tag{3b}$$

(i.e., the scalar wavefunction of the Gaussian beam), $\xi = 1 + iz/z_0$, and l is the azimuthal index. In our case, considerations can be restricted to the transverse electric field components e_x and e_y.

Let us consider the structure of the polarization states in the transverse beam cross section at a distance z from the waist plane. Figure 1, Ia presents a schematic diagram of the distribution of polarization states in a mode beam behind the crystal. The lines of circular and linear polarization are clearly distinguished. Unlike the classification of special points for a random field [3], the beam field behind the uniaxial crystal contains special regions of a degenerate ombilic point of the star type near the rings of circular polarization. If the beam after the crystal passes through a polarization analyzer, there appears a typical pattern of Airy's spirals. Rotation of the polarizer results in rotation of the whole pattern. Indeed, for any orientation of the polarizer axis, there are four points on the neighboring rings of linear polarization in which the amplitude becomes zero and the wave phase becomes indefinite. This corresponds to the generation of four optical vortices with opposite topological charges combined into topological quadrupoles. Rotation of the polarizer results in synchronous rotation of the bound vortices. However, it is impossible to separate a single optical vortex in this way.

At the same time, the distribution of singularities in the field of polarization states is such that the field structure can be transformed to a required form under the action of a quarter-wave plate. Indeed, past the quarter-wave plate (the extraordinary axis of which is oriented at an angle Q relative to the x axis), the Jones vector components (2) acquire the form

$$\begin{aligned} q_x &= \cos\delta/2[1 + i\exp(i\sigma Q)] \\ &+ i\sin\delta/2[1 + i\exp(-i\sigma Q)]\exp(i\sigma 2\varphi), \\ q_y &= i\sigma\{\cos\delta/2[1 - i\exp(i\sigma Q)] \\ &- i\sin\delta/2[1 - i\exp(-i\sigma Q)]\exp(i\sigma 2\varphi)\} \end{aligned} \tag{4}$$

and the structure of the field of polarization states transforms as depicted in Fig. 1, Ib. Here, it is possible to distinguish only two nondegenerate ombilic points, of the star type (Fig. 1, Id) and lemon type (Fig. 1, Ic), in contrast to the Nye classification [3], where the necessary intermediate ombilic point of the monstar (from "(le)monstar") type is introduced. According to expressions (4), if the initial fundamental Gaussian beam ($l = 0$) has a right-handed circular polarization ($\sigma = +1$) and the extraordinary axis of the quarter-wave plate makes an angle of $Q = \pi/4$, the first term in (3a) and the second term in (3b) become zero. Then, $q_x = 2i\sin\delta/2\exp(i\sigma 2\varphi)$ and $q_y = 2i\sigma\exp\delta/2$ and, hence, the x component of the beam field contains an optical vortex with topological charge $l = +2$ which is situated on the optical axis. Apparently, we can readily suppress the y component of the electric field using a polarizer, thus separating a beam carrying a single optical vortex (Fig. 1, IIc). However, there are regions far from the axis—the family of edge circular dislocations—where the field amplitude also becomes zero. These dislocations can also be readily suppressed by properly selecting the beam waist radius ρ. A change in the topological charge of the vortex is achieved by changing the direction of circulation in the initial beam and simultaneously rotating the polarizer transmission axis by $\pi/2$.

Let us consider the problem of control over the optical vortices. Figure 1, II shows the equilevel lines of ellipticity (thick solid curves) and azimuth (thin solid curves) characterizing the possible states of bound optical vortices. Indeed, let the angle Q of the anisotropic axes remain constant (e.g., $Q = \pi/4$) and let us rotate the polarizer transmission axis as described by the angle α. For $\alpha = \pi/2$, the x component of polarization is suppressed and the intensity distribution is characterized by a system of edge circular dislocations with the maximum at the center (Fig 1, IIa). A deviation from this position leads to splitting of two vortices from the edge dislocation closest to the center (Fig. 1, IIb); these vortices possess equal charges, $l = 1$, $\sigma = 1$, and move toward each other along the x axis. At $\alpha = 0$, these vortices merge to form a common optical vortex with $l = 2$ at the center (Fig. 1, IIc). A further increase in the angle leads to separation of the central vortex. The resulting unit vortices move in opposite directions along the y

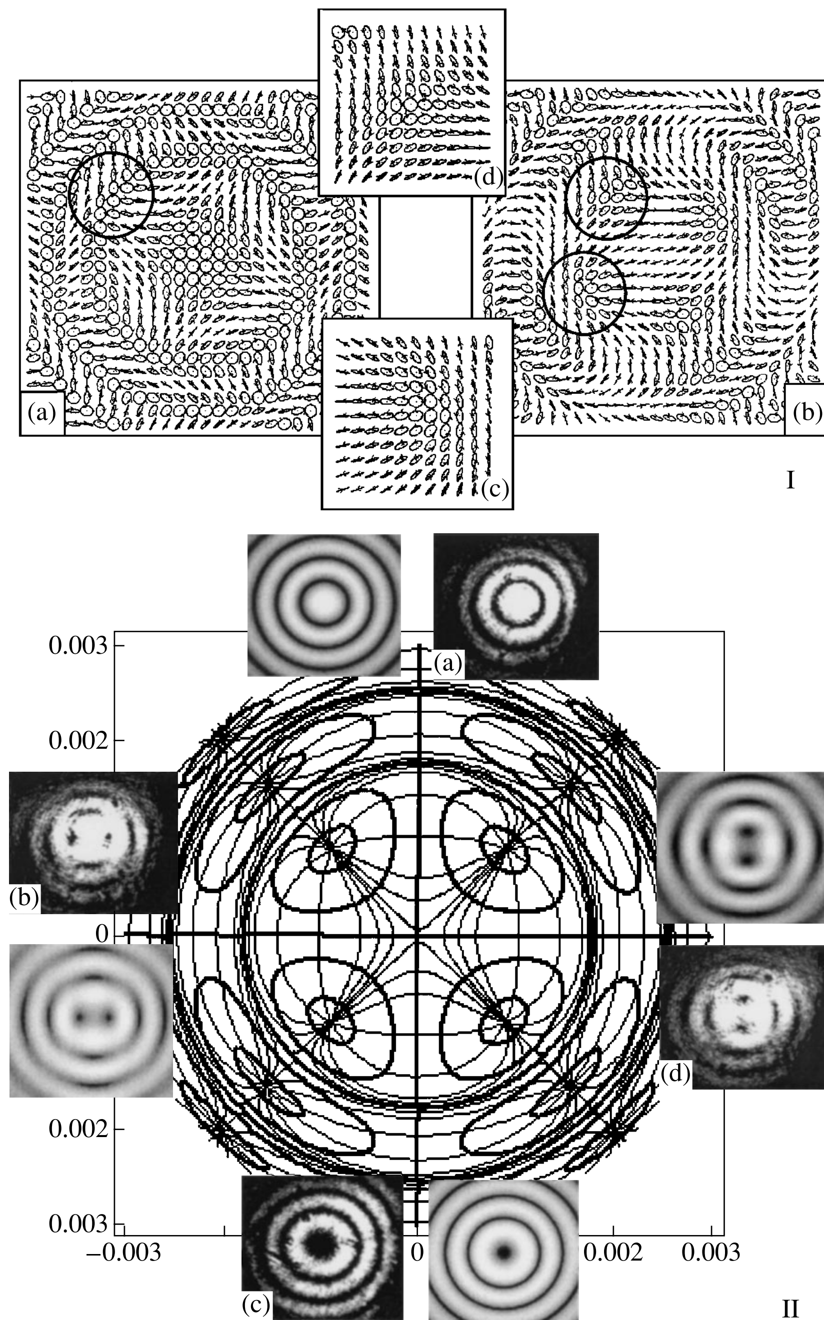

Fig. 1. Evolution of singular beams in the uniaxial crystal–quarter-wave plate–polarizer system. (I) Transverse distribution of polarization states in the field of the Gaussian beam (a) behind the crystal (b) past the quarter-wave plate and in the vicinity of the ombilic points of the (c) lemon and (d) star type. (II) Central panel shows the equilevel lines of the ellipticity (thick solid curves) and azimuth (thin solid curves); (a)–(d) theoretical and experimental ($LiNbO_3$ crystal, $\lambda = 0.6328$ μm) patterns of the intensity distribution at the system output.

axis (Fig. 1, IId) and merge into a common circular dislocation forming the initial pattern at $\alpha = -\pi/2$. Far from the center, the separation of two equally charged vortices from a circular dislocation violates the topological neutrality of the circular dislocation and leads to rearrangement of the entire dislocation pattern into a system of topological quadrupoles embracing one another but not interconnected.

When a topologically charged Gaussian beam (optical vortex) propagating through a crystal passes through the quarter-wave plate and the polarizer, the vortex charge changes by two units, either to increase or decrease, depending on the sign of the initial topological charge l and helicity σ. Using expressions (3) and (4), it is possible to derive the following expression for the topological charge of the beam at the system

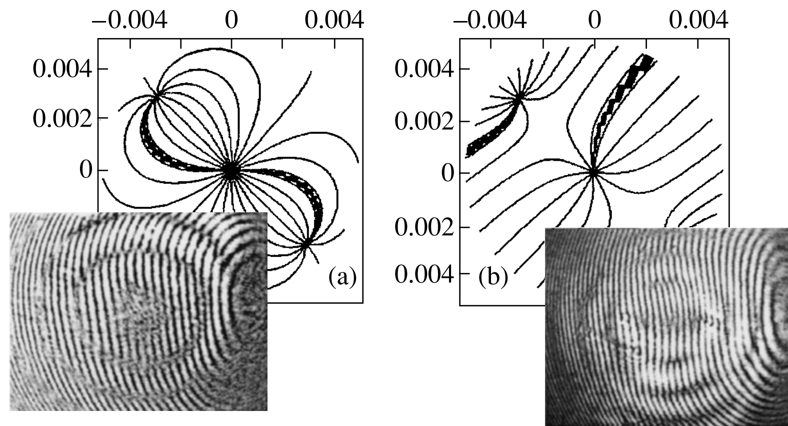

Fig. 2. Equiphase lines (with a $\pi/6$ step) and the experimental intensity distributions at the output of the crystal–quarter-wave plate–polarizer system, obtained upon the conversion of (a) a singular beam with $l = +2$, $\sigma = +1$ into a topologically neutral beam (unfolding of the singularity) and (b) a beam with $l = +1$, $\sigma = +1$ into a singular beam with triple topological charge ($l = +3$).

output: $t' = l + 2\sigma$. Obviously, a beam in the initial state with $l = -2$ and $\sigma = +1$ becomes topologically neutral at the system output and has a zero amplitude on the axis (which corresponds to unfolding of the singularity [3]). On the contrary, the initial state with $l = +2$ and $\sigma = +1$ converts into a state with doubled topological charge $l' = +4$ (multiplication of the topological charge). Such transformations were experimentally studied for a laser radiation with $\lambda = 0.6328$ μm passing through a $LiNbO_3$ crystal. The results presented in Fig. 2 demonstrate good coincidence with theory.

Thus, using the uniaxial crystal–quarter-wave plate–polarizer system, it is possible to generate optical vortices and control their geometric position, as well as the magnitude and sign of the topological charge.

REFERENCES

1. R. Oron, N. Davidson, A. Friesem, and E. Hasman, Opt. Lett. **25** (13), 939 (2000).
2. *Optical Vortices*, Ed. by M. V. Vasnetsov and K. Staliunas (Nova Science, New York, 1999).
3. J. F. Nye, *Natural Focusing and Fine Structure of Light Caustics and Wave Dislocations* (Institute of Physics Publishing, Bristol, 1999).
4. P. Hillion, J. Phys. A **32**, 2697 (1999).
5. A. V. Volyar, V. G. Shvedov, and T. A. Fadeeva, Pis'ma Zh. Tekh. Fiz. **25** (5), 87 (1999) [Tech. Phys. Lett. **25**, 203 (1999)].
6. A. Yariv and P. Yeh, *Optical Waves in Crystals: Propagation and Control of Laser Radiation* (Wiley, New York, 1984; Mir, Moscow, 1987).
7. M. Born and E. Wolf, *Principles of Optics* (Pergamon, Oxford, 1969; Nauka, Moscow, 1973).
8. E. Edser, *Light for Students* (Macmillan, London, 1907; Estestvoispytatel', St. Petersburg, 1914).

Translated by P. Pozdeev

Technical Physics Letters, Vol. 28, No. 11, 2002, pp. 962–963. Translated from Pis'ma v Zhurnal Tekhnicheskoĭ Fiziki, Vol. 28, No. 22, 2002, pp. 78–81.
Original Russian Text Copyright © 2002 by Svetukhin, Grishin, Il'ina, Prokof'eva, Rygalin.

A Study of the Oxygen Precipitation Kinetics in Zirconium-Doped Silicon

V. V. Svetukhin, A. G. Grishin, T. S. Il'ina, V. K. Prokof'eva, and B. N. Rygalin

Ul'yanovsk State University, Ul'yanovsk, Russia

Moscow Institute of Electronic Technology (Technical University), Moscow, Russia

e-mail: slava@sv.uven.ru

Received June 11, 2002

Abstract—The kinetics of oxygen precipitation at 900 and 1050°C was studied in Czochralski-grown silicon single crystals doped to various levels with zirconium. It is established that zirconium, while not participating in the nucleation of oxygen precipitates, decreases the concentration of interstitial oxygen in the crystals. *© 2002 MAIK "Nauka/Interperiodica".*

The introduction of gettering impurities such as zirconium into a solution melt during the growth of large single crystals improves the quality of silicon ingots by ensuring a more homogeneous interstitial oxygen distribution in both axial and radial directions and by increasing the lifetime of nonequilibrium charge carriers [1]. The distribution of oxygen in both the length and cross section of a single crystal ingot is well suited for autogetter operation. In order to select the optimum conditions for the internal gettering process in zirconium-doped silicon, it is necessary to study the effect of zirconium on the kinetics of oxygen precipitation in such systems.

We studied the precipitation kinetics of oxygen in samples of zirconium-doped silicon. Silicon single crystal ingots of KDB-12 grade with a diameter of 100 mm were grown by the Czochralski method (at the Moscow Institute of Electronic Technology) from a silicon melt with zirconium added to an atomic concentration from 5×10^{18} to 5×10^{19} cm^{-3}. The average content of zirconium atoms in our silicon crystals was 10^{16} cm^{-3}, while the local concentration gradually increased from the beginning to the end of the ingot. For this reason, we separated the ingots into four parts and studied plates cut from each part.

An increase in the zirconium content was accompanied by a decrease in concentration of the interstitial oxygen atoms: from 9.6×10^{17} cm^{-3} in zirconium-free samples to $(6.40–8.69) \times 10^{17}$ cm^{-3} in samples doped with zirconium [2]. Dependence of the interstitial oxygen concentration on zirconium content can be related both to elastic stresses created by the incorporated dopant atoms and to the formation of complexes involving oxygen and zirconium atoms.

All samples were annealed at 900 and 1050°C for 70 h. The concentration of interstitial oxygen was determined by determining the optical absorption at a wavelength of 1106 cm^{-1} with allowance for the multiple internal reflection in a silicon plate and asymmetric pretreatment of the sample surfaces [2]. Typical curves of the oxygen precipitation kinetics in silicon annealed at 900 and 1050°C are presented in the figure.

It was established that the presence of zirconium slows down the process of oxygen precipitation. In order to elucidate the reason behind the retarded precip-

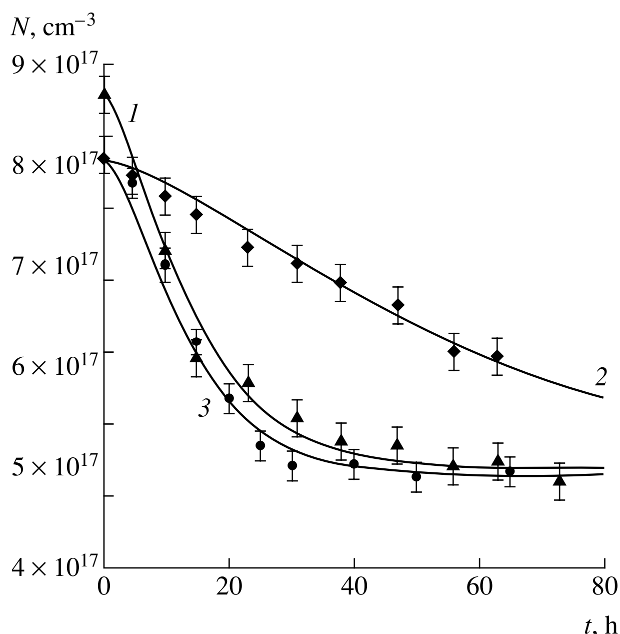

Time variation of the interstitial oxygen concentration N showing the oxygen precipitation kinetics in single crystal silicon: (*1*) undoped Si annealed at 900°C; (*2*) Zr-doped Si annealed at 900°C; (*3*) Zr-doped Si annealed at 1050°C. Symbols represent experimental data, solid curves show the results of calculations by formula (1).

itation kinetics, we described experimental data in terms of a theoretical model proposed previously [3]:

$$\frac{dN(t)}{dt} = -4\pi D b N_C^{2/3}[N(t) - N_E]\{N(0) + mN_C - N(t)\}^{1/3}, \quad (1)$$

where D is the coefficient of diffusion of the interstitial oxygen, $b = 0.25$ nm, N_E is the equilibrium concentration of oxygen in silicon, $N(0)$ is the initial oxygen concentration, $m = 4$ is the number of particles in the nucleation center, and N_C is the concentration of the precipitation nucleation centers. Using Eq. (1), it is possible to explain, in particular, the asymptotic behavior established by Ham [4] for the growth of precipitates with a constant eccentricity.

The only fitting parameter in Eq. (1) is the concentration N_C of the precipitation nucleation centers. By processing all the experimental data in terms of Eq. (1) and conducting a comparative analysis of the experimental results and theoretical calculations, we determined the concentrations of nucleation canters in the samples taken from various parts of the zirconium-doped ingot and from an undoped single crystal: $(3–4) \times 10^{10}$ cm^{-3} for the samples annealed at 900°C and $(3–5) \times 10^9$ cm^{-3} for those annealed at 1050°C.

As is known, the concentration of nucleation centers for the precipitation of oxygen in Czochralski-grown undoped (zirconium-free) silicon single crystals is described by the following relation [5]:

$$N_C(T) = 0.15\exp(2.65/kT)\ \text{cm}^{-3}. \quad (2)$$

Calculations by this formula yields $N_C = 4 \times 10^{10}$ and 2×10^9 cm^{-3} for $T = 900$ and 1050°C, respectively. Thus, the calculated values are consistent with those obtained by processing the experimental data for zirconium-doped samples. From this we conclude that zirconium does not participate (or participates insignificantly) in the formation of nucleation centers for oxygen precipitation. Therefore, retardation of the kinetics of oxygen precipitation in zirconium-doped silicon is related predominantly to a decrease in the concentration of interstitial oxygen.

REFERENCES

1. B. N. Rygalin, E. B. Sokolov, and V. K. Prokof'eva, Izv. Vyssh. Uchebn. Zaved., Élektron. Tekh., Nos. 4–5, 71 (2000).
2. T. S. Pchelintseva, V. K. Prokof'eva, V. V. Svetukhin, *et al.*, Pis'ma Zh. Tekh. Fiz. **27** (20), 20 (2001) [Tech. Phys. Lett. **27**, 852 (2001)].
3. S. V. Bulyarskiĭ, V. V. Svetukhin, and O. V. Prikhod'ko, Fiz. Tekh. Poluprovodn. (St. Petersburg) **33** (11), 1280 (1999) [Semiconductors **33**, 1157 (1999)].
4. F. S. Ham, Phys. Chem. Solids **6**, 335 (1958).
5. A. Borghesi, B. Pivac, A. Sassella, *et al.*, J. Appl. Phys. **77**, 4196 (1995).

Translated by P. Pozdeev

Technical Physics Letters, Vol. 28, No. 11, 2002, pp. 964–966. Translated from Pis'ma v Zhurnal Tekhnicheskoĭ Fiziki, Vol. 28, No. 22, 2002, pp. 82–88.
Original Russian Text Copyright © 2002 by Odnoblyudov, Egorov, Kryzhanovskaya, Gladyshev, Mamutin, Tsatsul'nikov, Ustinov.

Room-Temperature Photoluminescence at 1.55 μm from Heterostructures with InAs/InGaAsN Quantum Dots on GaAs Substrates

V. A. Odnoblyudov, A. Yu. Egorov, N. V. Kryzhanovskaya, A. G. Gladyshev, V. V. Mamutin, A. F. Tsatsul'nikov, and V. M. Ustinov

Ioffe Physicotechnical Institute, Russian Academy of Sciences, St. Petersburg, 194021 Russia

Received May 22, 2002

Abstract—Room-temperature photoluminescence (PL) at 1.55 μm from heterostructures with InAs/InGaAsN quantum dots (QDs) grown by MBE on GaAs substrates is demonstrated for the first time. The effect of nitrogen incorporated into InAs/InGaAsN QDs on the PL wavelength and intensity was studied. The integral intensity of PL from the new structure with InAs/(In)GaAsN QDs is comparable to that from a structure with InGaAsN quantum wells emitting at 1.3 μm. *© 2002 MAIK "Nauka/Interperiodica".*

Introduction. Wide use of fiber optic communication lines in local networks is hindered by the lack of reliable inexpensive radiation sources. Good prospects can be related to vertical-cavity surface-emitting lasers, but the development of such devices based on traditional heterostructures is problematic. Presently, the effort of many research laboratories around the world is being concentrated on the creation of new heterostructures which would serve as a basis for more effective radiation sources operating in the wavelength interval of 1.3–1.55 μm, which would offer an alternative to the existing heterostructures of the InGaAsP/InP type. This wavelength interval corresponds to the transparency window of a usual optical fiber, 1.3 μm being the wavelength of minimum dispersion and 1.55 μm ensuring minimum absorption.

At present, possible alternatives include heterostructures with InGaAsN/GaAs quantum wells (QWs) and InAs/InGaAs QDs on GaAs substrates. These heterostructures have been successfully employed in edge-emitting injection lasers [1, 2] and vertical-cavity surface-emitting lasers [3, 4] operating at 1.3 μm. However, the passage to longer wavelengths (up to 1.55 μm) with the structures of both types is complicated by basic restrictions on the composition and thickness of QDs, which are related to the period of pseudomorphous growth.

Attempts at moving toward longer wavelengths reported by various laboratories have not led to the creation of structures capable of effectively emitting at 1.55 μm. Recently, the possibility of photoluminescence (PL) in the vicinity of 1.55 μm was demonstrated for the heterostructures with InAs/InGaAs QDs in a GaAs matrix grown at rather low temperatures [5, 6]. The emission at 1.55 μm was reported for InAs QDs with nitrogen additives [7] and for InAs QDs in a GaAsN matrix [8], but the PL intensity achieved with both approaches was low. An increase in the molar fraction of nitrogen and indium in InGaAsN QDs shifted the emission wavelength from 1.3 μm to 1.55 μm, but at the expense of a significant decrease in the PL intensity [9].

In this study, we used the InAs/InGaAs QDs in a GaAs matrix (emitting at 1.3 μm) as an object to be modified so as to shift the emission to 1.55 μm. We demonstrated that adding nitrogen to the material of a layer (InGaAs) overgrown on the InAs QDs leads to a significant decrease in the bandgap width and decreases the level of quantum confinement in InAs QDs by a value sufficient to shift the PL peak up to 1.55 μm. The radiative recombination efficiency in the modified objects and InGaAsN QDs differs by a factor of two.

Experimental. The experiments were performed in a molecular beam epitaxy (MBE) system of the EP-1203 type equipped with an RF plasma nitrogen source (Epi Unibulb) and a solid-state source of arsenic. The samples were grown at a substrate temperature of 470°C. The heterostructures with QDs were synthesized immediately during the growth in the initial stages of InAs deposition onto (001)GaAs by the Stranski–Krastanov growth mechanism [10]. The QDs were overgrown with InGaAsN layers with a nitrogen content that varied within 0–2%. This resulted in the formation of a new object representing InAs/InGaAsN QDs surrounded by layers of either GaAs or GaAsN with a thickness of 0–1000 Å and a molar fraction of nitrogen within 0–2.5% (below, the surrounding layer will be referred to as the matrix).

The PL spectra were excited by an argon laser at an intensity of 100 W/cm^2 and measured using a cooled germanium detector. The content of nitrogen in the matrix was determined in special GaAsN test samples

using an X-ray diffraction technique based on the rocking curve measurements in the vicinity of the (004)GaAs reflection. The accuracy of nitrogen determination was 0.01%.

Results and discussion. In the first series of samples, InAs/InGaAs QDs emitting at 1.3 μm were placed into a GaAsN layer. Figure 1 shows a plot of the emission wavelength versus nitrogen content in the GaAsN matrix. As can be seen from these data, adding nitrogen to the GaAs matrix leads to a significant longwave shift of the PL peak of the QDs studied. The experimental curve is well approximated by the exponential function $f(x) = 1.3 + 0.005\exp(x/0.74)$. This approximation, while having no physical meaning, allows the longwave shift of the PL peak to be reliably predicted for a given nitrogen content in the matrix. The nitrogen content required to obtain QDs emitting at 1.55 μm can be estimated by extrapolating this function in the region of higher nitrogen concentrations. Thus, upon adding about 3% nitrogen, one can expect to observe the PL at 1.55 μm. It should noted that an increase in the nitrogen content in the matrix was accompanied by a systematic decrease in the PL signal intensity.

In the second stage of the experiment, we studied a heterostructure with InAs/InGaAsN QDs placed inside a $GaAsN_{2.5\%}$ layer with a thickness of 1000 Å. Adding only 0.85% nitrogen to the InAs layer used to overgrow the $In_{15\%}GaAs$ led to a shift of the PL wavelength up to 1.55 μm. A decrease in thickness of the GaAsN matrix, with the same nitrogen content in the matrix and the InGaAsN layer used to overgrow the QDs, led to an increase in the PL intensity not affecting the PL peak position. The results of this series of experiments are presented in Fig. 2. The emission at 1.55 μm corresponds to radiative transitions inside the QDs. The second PL peak with a maximum at 1.17 μm corresponds to emission from the $GaAsN_{2.5\%}$ matrix. As the matrix thickness decreases, the intensity of emission at 1.55 μm grows (for the peak position at 1.55 μm remaining unchanged) and the PL signal at 1.17 μm drops. This implies that nonequilibrium charge carriers tend to recombine predominantly via the QD states. The inset in Fig. 2 shows a plot of the relative integral PL intensity versus the GaAsN matrix layer thickness.

Complete replacement of the GaAsN matrix by GaAs, with the QD composition (producing the spectra presented in Fig. 2) remaining unchanged, led to a shortwave shift of the PL peak, but provided for a significant increase in the PL signal intensity. The shortwave shift could be partly reduced without a loss in intensity by increasing the overall nitrogen content in the InGaAsN layer (used to overgrow the QDs) from 0.84 to 15%. The integral intensity of emission from this structure was about 18 times that from the structure with In(Ga)As(N) QDs in a 100-Å-thick GaAsN matrix. As a result, the PL intensity of a structure with InAs/InGaAsN QDs in the GaAs matrix (emitting at 1.54 μm) became comparable (Fig. 3) with the PL intensity of a test structure with $GaAs/In_{0.36}Ga_{0.64}As_{0.98}N_{0.02}/GaAs$ QWs (emitting at 1.26 μm). Use of InGaAsN QWs of a like composition [2] as the active region of injection lasers demonstrated the possibility of low-threshold lasing at 1.3 μm. We believe that a further increase in the inten-

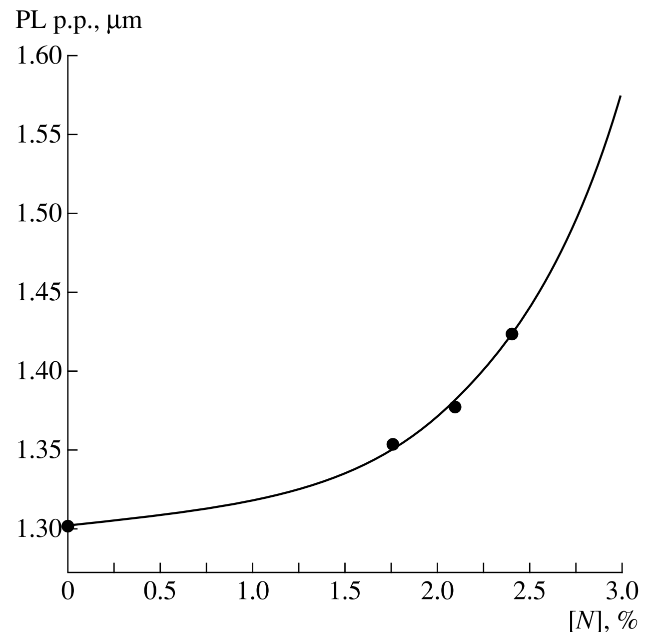

Fig. 1. A plot of the emission wavelength versus nitrogen content in the GaAsN matrix containing InAs QDs overgrown with $In_{15\%}GaAs$. Symbols represent the experimental points; solid curve shows the approximating exponential function.

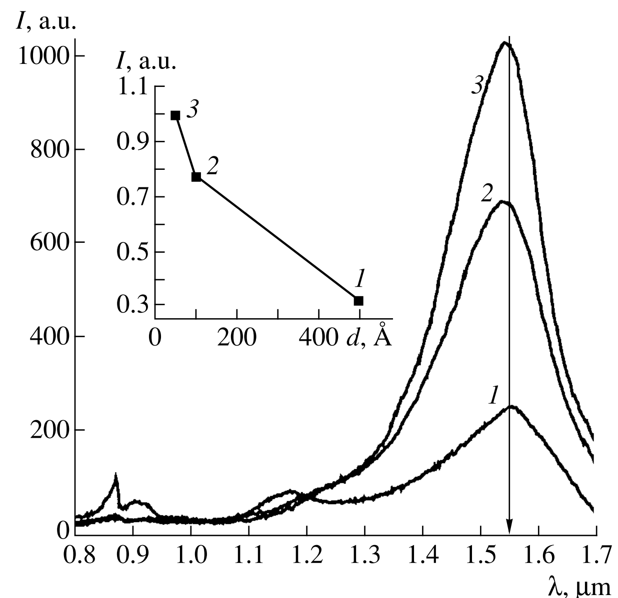

Fig. 2. PL spectra of the structures with InAs QDs overgrown with $In_{15\%}GaAsN_{0.85\%}$ in a $GaAsN_{2.5\%}$ matrix with a thickness of (*1*) 1000, (*2*) 200, and (*3*) 100 Å. The inset shows a plot of the relative integral PL intensity versus matrix thickness for the same samples.

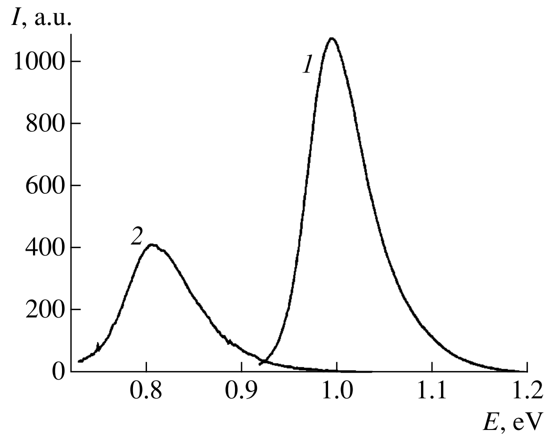

Fig. 3. PL spectra of (*1*) InGaAsN QWs in a GaAs matrix and (*2*) $InAs/In_{15\%}GaAsN_{1.5\%}$ QDs in a GaAs matrix.

sity of emission from the structures with InAs/InGaAsN QDs can be provided by optimization of the annealing stage. It is also possible that an additional slight increase in the nitrogen content in the InGaAsN layer (used to overgrow the QDs) will be required in order to retain the PL peak position at 1.55 μm.

Conclusion. We obtained for the first time room-temperature emission at 1.55 μm from heterostructures with InAs/InGaAsN QDs in a GaAs matrix on (001)GaAs substrates with a total PL intensity comparable to that from $GaAs/In_{0.36}Ga_{0.64}As_{0.98}N_{0.02}/GaAs$ QWs (emitting at 1.26 μm). The emission wavelength and intensity in the proposed structure was studied as a function of the nitrogen content in the matrix and in the layer used to overgrow the QDs, as well as a function of the matrix thickness. An increase in the molar fraction of nitrogen in the matrix leads to a longwave shift of the PL peak, while a decrease in the matrix thickness increases the signal intensity. Adding nitrogen to the layer used to overgrow the QDs and placing this system into a GaAs matrix sharply (by a factor of ~18) increases the PL intensity, but at the expense of a short-wave shift of the PL peak. The latter shift can be partly reduced by increasing the nitrogen content in the layer used to overgrow the QDs.

Acknowledgments. This study was supported by the federal program "Physics of Solid State Nanostructures", the NATO Science for Peace Program (grant no. SfP-972484), the US Civilian Research and Development Foundation (CRDF grant no. RE1-2221), and the Russian Foundation for Basic Research (project no. 02-02-17677). One of the authors (V.M.U.) is grateful to the Foundation for the Promotion of Russian Science for support.

REFERENCES

1. V. M. Ustinov and A. E. Zhukov, Semicond. Sci. Technol. **15**, R41 (2000).
2. A. Yu. Egorov, B. Brenklau, B. Borchert, *et al.*, J. Cryst. Growth **227–228**, 545 (2001).
3. N. A. Maleev, A. Yu. Egorov, A. E. Zhukov, *et al.*, Fiz. Tekh. Poluprovodn. (St. Petersburg) **35** (7), 881 (2001) [Semiconductors **35**, 847 (2001)].
4. J. A. Lott, N. N. Ledentsov, V. M. Ustinov, *et al.*, Electron. Lett. **36** (5), 1384 (2000).
5. A. E. Zhukov, B. V. Volovik, S. S. Mikhrin, *et al.*, Pis'ma Zh. Tekh. Fiz. **27** (17), 51 (2001) [Tech. Phys. Lett. **27**, 734 (2001)].
6. A. A. Tonkikh, V. A. Egorov, N. K. Polyakov, *et al.*, Pis'ma Zh. Tekh. Fiz. **28** (10), 72 (2002) [Tech. Phys. Lett. **28**, 434 (2002)].
7. M. Sopanen, H. P. Xin, and C. W. Tu, Appl. Phys. Lett. **76**, 994 (2000).
8. A. Yu. Egorov *et al.*, in *International Symposium QD 2000, Munich, 2000.*
9. M. Fisher, M. Reinhardt, and A. Forhel, Electron. Lett. **36** (14), 1208 (2000).
10. D. Bimberg, M. Grundmann, and N. N. Ledentsov, *Quantum Dot Heterostructures* (Wiley, Chichester, 1999).

Translated by P. Pozdeev

Technical Physics Letters, Vol. 28, No. 11, 2002, pp. 967–969. Translated from Pis'ma v Zhurnal Tekhnicheskoĭ Fiziki, Vol. 28, No. 22, 2002, pp. 89–94.
Original Russian Text Copyright © 2002 by Tchen.

A Kinematic Approximation for the Coefficient of X-ray Wave Backscattering from a Strongly Bent Crystal

T. Tchen
Moscow State Academy of Fine Chemical Technology, Moscow, Russia
e-mail: docent65@mtu-net.ru; ttchen@e-mail.ru
Received April 15, 2002; in final form, June 6, 2002

Abstract—An analytical expression for the coefficient of Bragg backscattering ($\theta_B \cong \pi/2$) of an X-ray wave from a strongly bent thin crystal is obtained. It is shown that the amplitude reflection coefficient for backscattering from a strongly bent crystal differs from the value for a flat crystal of the same thickness by a small phase-dependent factor. *© 2002 MAIK "Nauka/Interperiodica".*

The diffraction reflection of X-ray beams in the backscattering mode (i.e., for the Bragg angle $\theta_B \cong \pi/2$) from flat and strongly bent crystals was experimentally studied in [1–8]. Measurements in the backscattering geometry offer some advantages over the case of diffraction for the Bragg angles $\theta_B < \pi/2$. First, the reflected beam intensity in the former case is significantly (by 2–3 orders of magnitude) greater than that in the latter one. Indeed, using the explicit expression for the angular variable y (see, e.g., [9]),

$$y = [2\Delta\theta(\gamma_0/|\gamma_h|)\sin 2\theta_B + (1+\gamma_0/|\gamma_h|)\chi_0]/2C(\chi_h\chi_{-h}\gamma_0/|\gamma_h|)^{1/2}, \tag{1}$$

and taking into account that, in the backscattering mode, $\sin 2\theta_B \cong 2\Delta\theta \ll 1$, we readily obtain an expression for the angular width of the backscattering curve:

$$\Delta\theta_{\theta\cong\pi/2} \cong (\chi_h\chi_{-h})^{1/4}(2C)^{1/2}/(\gamma_0/|\gamma_h|)^{1/4}, \quad |C| = 1, \quad \gamma_0 = |\gamma_h|. \tag{2}$$

In Eq. (1), $\Delta\theta = \theta - \theta_B$ is the deviation from the exact Bragg angle θ_B, $\gamma_{0,h}$ are the directional cosines for the incident and diffracted waves, $\chi_{0,h,-h}$ are the Fourier components of the X-ray polarizability, and C is the polarization factor. As can be seen from formula (2), the angular width of the backscattering curve is greater than that for $\theta_B < \pi/2$ by a factor of $(\chi_h\chi_{-h})^{-1/4}$.

Another advantage of backscattering is its high sensitivity with respect to the degree of monochromaticity $\Delta\lambda/\lambda$ of the radiation employed. Indeed, according to the Bragg law, $\Delta\lambda/\lambda = \cot\theta_B\Delta\theta \le (\Delta\theta)^2$. For a highly collimated beam with $\Delta\theta \sim 10^{-5}$–$10^{-6}$, this yields $\Delta\lambda/\lambda \sim 10^{-10}$–$10^{-12}$. The third important feature of backscattering is its high sensitivity with respect to a change Δd in the interplanar spacing d: $\Delta d/d \le (\Delta\theta)^2$. Finally, the backscattering regime is characterized by minimum geometric aberrations.

However, until now, X-ray backscattering under the Bragg diffraction conditions was studied predominantly for thick crystals: $l > \Lambda$, where l is the crystal thickness, $\Lambda = \lambda/|\chi_{hr}|$ is the extinction length for backscattering, and λ is the incident radiation wavelength. The aim of this study is to obtain an analytical expression for the amplitude reflection coefficient of a plane X-ray wave backscattered from a thin crystal ($l \ll \Lambda$) under kinematic diffraction conditions. An expression for the backscattering coefficient of such a crystal will be derived proceeding from the well-known analytical expression for the coefficient of reflection from a strongly bent crystal of finite thickness and refers to the region of the angular variable y where the oscillation character of the reflection coefficient can be ignored.

Let us consider a flat crystal of thickness l. Using the results obtained in [10], the amplitude reflection coefficient in this case can be expressed as

$$r_{\text{flat}} = [1-\exp\{i(\varepsilon_1-\varepsilon_2)l\}]/[R_2 - R_1\exp\{i(\varepsilon_1-\varepsilon_2)l\}], \tag{3}$$

where

$$\varepsilon_{1,2} = \pi[\chi_0 + C(\chi_h\chi_{-h}\gamma_0/|\gamma_h|)^{1/2} \times(-y \pm \{y^2-1\}^{1/2})]/\lambda\gamma_0,$$
$$R_{1,2} = (-y \pm \{y^2-1\}^{1/2})(\chi_h/\chi_{-h})^{1/2}. \tag{4}$$

Formulas (3) and (4) are applicable to the case of backscattering as well. According to expression (3), the diffraction reflection coefficient (see the $|r_{\text{flat}}|^2$ versus y curve in the figure) exhibits oscillations at $|y| > 1$. The oscillation period Δy can be estimated by assuming that, approximately,

$$2\pi|\chi_{hr}|(y^2-1)l/\lambda \approx 2\pi n \tag{5}$$

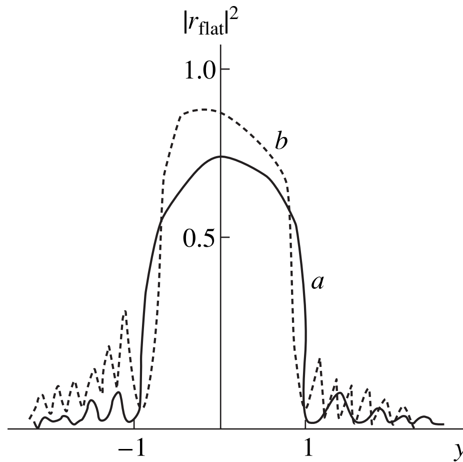

Profiles of the amplitude reflection coefficient of a flat crystal $|r_{\text{flat}}|^2$ as a function of the angular variable y for CuK_α radiation backscattered (220 reflection) from a Si crystal ($\Lambda = 6.28$ μm) with a thickness of $l = 12.56$ (*a*) and 31.4 μm (*b*).

(where n is an integer), from which it follows that $\Delta y = \{\Lambda^2(n+1)^2/l^2 + 1\} - \{\Lambda^2 n^2/l^2 + 1\}$. For a very thin crystal ($l \ll \Lambda$), this yields $\Delta y \approx \Lambda/l$. In the opposite case of $l \gg \Lambda$, we obtain $\Delta y \approx \Lambda^2(2n+1)/(2l^2)$.

Let us ignore the oscillation structure of $|r_{\text{flat}}|^2$ and consider only the part of the curve within the interval $|y| \ll \{\Lambda^2/(4\pi^2 l^2) + 1\}^{1/2}$. As the crystal thickness l increases, the interval of $|y|$ obeying this condition exhibits narrowing. With neglect of the oscillation term, expression (3) yields

$$r_{\text{flat}} \cong i\pi|\chi_{hr}|l/\lambda. \tag{6}$$

This formula was derived assuming, for definiteness, that the crystal is centrosymmetric ($\chi_h = \chi_{-h}$) and taking into account that $(\varepsilon_1 - \varepsilon_2)l \ll 1$.

Now, let us pass to the case of a bent crystal of finite thickness l. According to [11], the amplitude reflection coefficient of such a crystal is

$$r_{\text{bent}} = -(i)^{3/2}(q/4d)(\pi/2B)^{1/2}\tan\theta_B \times[\Phi(-t_1/2^{1/2}) - \Phi(-t_0/2^{1/2})]\exp(-t_0^2/2),$$

where $q = \pi C d\chi_h/(\lambda\sin\theta_B)$ is the coefficient of reflection from an atomic plane, $t_1 = t_0 + 4l\cot\theta_B(-iB)^{1/2}$, $t_0 = (-i/4B)^{1/2}k$, $k \le 2\pi\Delta\theta/\lambda$, B is the crystal deformation gradient, and $\Phi(t)$ is the probability integral. Assuming that $l \ll \pi/(4\lambda B)$, let us expand the difference of the probability integrals in the above expression in a Taylor series and restrict the expansion to the first-order derivative of $\Phi(t)$:

$$\Phi(-t_1/2^{1/2}) - \Phi(-t_0/2^{1/2}) \approx -2(\pi)^{-1/2}\exp(-t_0^2/2)(t_1 - t_0)/2^{1/2}. \tag{7}$$

In this approximation, the amplitude reflection coefficients in the backscattering mode is as follows:

$$r_{\text{bent}} \cong i\pi|\chi_{hr}|l\exp(-t_0^2)/\lambda. \tag{8}$$

Comparing expressions (6) and (8), we obtain

$$r_{\text{bent}} = r_{\text{flat}}\exp(ik^2/4B). \tag{9}$$

According to [12], the crystal bending parameter for a symmetric diffraction geometry and σ-polarized radiation is

$$|v| = \pi^2|\chi_{hr}|^2/(16\lambda^2 B\sin^2\theta_B\cos^2\theta_B). \tag{10}$$

Under the conditions of backscattering, $\cos\theta_B \le |\chi_{hr}|^{1/2}$. Taking $\cos\theta_B = |\chi_{hr}|^{1/2}/2$, we obtain for the crystal bending parameter

$$|v|_{\theta\approx\pi/2} = \pi^2|\chi_{hr}|/(4B\lambda^2). \tag{11}$$

Using the condition of strong bending $|v| \ll 1$, the necessary crystal deformation gradient can be estimated as $B \gg \pi^2|\chi_{hr}|/(4\lambda^2)$. For $|\chi_{hr}| \sim 10^{-5}$ and $\lambda \sim 1$ Å, this implies $B \gg 10^{15}$ m^{-2}.

It should be noted that formulas (10) and (11) are partial cases of a more general expression for the crystal bending parameter:

$$|v| = \pi^2(\Delta\theta)^2/(4\lambda^2 B). \tag{12}$$

Taking $\Delta\theta$ equal to the angular halfwidth of the reflection curve, we obtain formulas (10) and (11). Strictly speaking, an exact expression for the crystal bending parameter $|v|$ in the case of backscattering can be obtained by solving the problem of dynamic diffraction in the back halfspace for a bent crystal. However, it is also possible to use expression (12) with

$$(\Delta\theta)_{\theta\approx\pi/2} = K^{1/2}|\chi_{hr}|/\sin 2\theta_B, \tag{13}$$

where $\theta_B \ne \pi/2$ and $K \ll 1$. The value of K should be chosen depending on the deformation gradient B, so that a weak bending at $\theta_B \ne \pi/2$ would correspond to a strong bending at $\theta_B \cong \pi/2$.

Taking into account formulas (9) and (11), we obtain $r_{\text{bent}} \cong r_{\text{flat}}\exp(i|v|^2)$. Thus, the amplitude reflection coefficient for backscattering from a strongly bent crystal differs from the value for a flat crystal of the same thickness by a small phase-dependent factor. The presence of this factor may influence, for example, the focusing properties of bent crystals under consideration (including the cases of both a free-standing crystal and a single crystal film deposited onto a thick crystalline substrate).

In concluding, it should be noted that, despite the obvious advantages of diffraction measurements in the backscattering mode, practical realization of this scheme encounters considerable difficulties. This is related to the fact that, in the case of exact back reflection, the diffracted beam propagates in the direction

opposite (antiparallel) to that of the incident beam. In order to surmount this problem, it is necessary to use a sliding angle above $\pi/2 - |\chi_{hr}|^{1/2}$. Under these conditions, the sum of distances (i) from a source S of the spherical wave to a normal to the crystal surface and (ii) from the normal to the image S' is $\sim|\chi_{hr}|^{1/2}(L_0 + L_h)$, where L_0 and L_h are the distances from S to the crystal and from the crystal to S', respectively. In the case of a synchrotron radiation source with $L_0 \geq 10$ m, the source S and image S' can be spaced by $\geq 10^{-2}$ m in the direction perpendicular to the normal. This removes the aforementioned problem hindering experimental realization of the X-ray diffraction measurements in the backscattering mode.

Diffraction in biaxially bent crystals in the backscattering geometry provides for a sharp increase in the level of signal intensity in X-ray optics and can find application in X-ray spectroscopy, microscopy, etc.

REFERENCES

1. A. Yu. Nikulin, J. R. Davis, N. T. Jones, *et al.*, Phys. Status Solidi A **179**, 103 (2000).
2. Yu. V. Shvyd'ko and E. Gerdau, Hyperfine Interact. **123**/**124**, 741 (1999).
3. Yu. V. Shvyd'ko, E. Gerdau, J. Jäschke, *et al.*, Phys. Rev. B **57**, 4968 (1998).
4. W. Graeff and G. Materlik, Nucl. Instrum. Methods **195**, 97 (1982).
5. V. I. Kushnir and É. V. Suvorov, Pis'ma Zh. Éksp. Teor. Fiz. **44**, 205 (1986) [JETP Lett. **44**, 262 (1986)].
6. V. I. Kushnir and E. V. Suvorov, Phys. Status Solidi A **122**, 391 (1990).
7. D. P. Woodruff, D. L. Seymour, C. F. McConville, *et al.*, Phys. Rev. Lett. **58**, 1460 (1987).
8. C. Cusatis, D. Udron, I. Mazzaro, *et al.*, Acta Crystallogr. A **52**, 614 (1996).
9. Z. G. Pinsker, *X-ray Optics* (Nauka, Moscow, 1982).
10. V. A. Bushuev and T. Tchen, Vestn. Mosk. Univ., Ser. 3: Fiz., Astron. **29** (6), 58 (1988).
11. F. N. Chukhovskiĭ, Metallofizika **3** (5), 3 (1981).
12. K. T. Gabrielyan, F. N. Chukhovskiĭ, and D. I. Piskunov, Zh. Éksp. Teor. Fiz. **96** (3), 834 (1989) [Sov. Phys. JETP **69**, 474 (1989)].

Translated by P. Pozdeev